

# Development of a Low Energy Ion Source for ROSINA Ion Mode Calibration

Inauguraldissertation  
der Philosophisch-naturwissenschaftlichen Fakultät  
der Universität Bern

vorgelegt von

**Martin Rubin**

von Reichenbach i.K.

Leiter der Arbeit:  
Prof. Dr. Kathrin Altwegg  
Physikalisches Institut der Universität Bern



# Development of a Low Energy Ion Source for ROSINA Ion Mode Calibration

Inauguraldissertation  
der Philosophisch-naturwissenschaftlichen Fakultät  
der Universität Bern

vorgelegt von

**Martin Rubin**

von Reichenbach i.K.

Leiter der Arbeit:  
Prof. Dr. Kathrin Altwegg  
Physikalisches Institut der Universität Bern

Von der Philosophisch-naturwissenschaftlichen Fakultät angenommen.

Der Dekan:

Bern, den 30. März 2006

Prof. Dr. Paul Messerli





## ABSTRACT

The aim of this work has been to design, construct, and implement a Low Energy Ion Source for the ion mode calibration of the two ROSINA mass spectrometers on board ESA's Rosetta spacecraft to comet 67P/Churyumov-Gerasimenko.

The requirements for the source stem from the specific Rosetta mission design: the ion energy distribution of a weak comet and the effects of spacecraft charging have both been reviewed. We show the physics that are relevant for the development of a new design for this type of ion sources. As part of this thesis, a corresponding source has been built and existing calibration facilities have been upgraded. The measurements of the sensitivity, beam shape, and energy distribution and corresponding computer simulations demonstrate that the Low Energy Ion Source meets the scientific requirements for the Rosetta mission.

Last compiled: February 24, 2006 9:49



# CONTENTS

<i>List of Tables</i> . . . . .	viii
<i>List of Figures</i> . . . . .	xviii
<i>1. Introduction</i> . . . . .	1
<i>2. The Rosetta Mission</i> . . . . .	3
2.1 The ROSINA instrument . . . . .	3
2.1.1 The Double Focusing Mass Spectrometer (DFMS) . . . . .	4
2.1.2 The Reflectron-type Time-Of-Flight mass spectrometer (RTOF) . . . . .	6
2.2 The target: comet 67P/Churyumov-Gerasimenko . . . . .	8
2.2.1 Ion dynamics in a cometary coma . . . . .	9
2.2.2 From a weak to a strong comet . . . . .	11
2.2.3 Particle distribution functions . . . . .	15
2.3 Spacecraft environment . . . . .	17
2.3.1 Thermal Electron Current . . . . .	18
2.3.2 Ion Current . . . . .	19
2.3.3 Photoelectric Current . . . . .	20
2.3.4 Results and Discussion . . . . .	21
<i>3. Setup of the Low Energy Ion Source</i> . . . . .	25
3.1 Requirements . . . . .	25
3.2 Source layout . . . . .	28
3.2.1 Electron flight path . . . . .	29
3.2.2 Neutral gas and ion flight path . . . . .	30

---

3.2.3	Microtip . . . . .	31
3.2.4	Glass capillary plate . . . . .	32
3.2.5	Nominal potentials of the Low Energy Ion Source . . .	33
3.3	Standards for the used electronics . . . . .	34
4.	<i>Theory</i> . . . . .	35
4.1	The glass capillary array . . . . .	36
4.1.1	The gas flow . . . . .	36
4.2	Ionizing the neutral gas beam in the source . . . . .	43
4.2.1	The ion current . . . . .	43
4.2.2	Space-charge effects . . . . .	45
4.3	The vacuum system . . . . .	47
4.4	Summary from theoretical considerations . . . . .	49
5.	<i>Characterization of the Low Energy Ion Source</i> . . . . .	51
5.1	Microtip conditioning . . . . .	51
5.1.1	Required conditions . . . . .	51
5.1.2	Formation procedure . . . . .	52
5.1.3	Conditioning results for the Low Energy Ion Source microtip . . . . .	55
5.2	Grid transmissions . . . . .	58
5.3	Sensitivity and intensity . . . . .	60
5.3.1	Static mode sensitivity . . . . .	61
5.3.2	Maximum current . . . . .	62
5.3.3	Dynamic mode sensitivity . . . . .	63
5.4	Beam shape measurements . . . . .	66
5.4.1	Static mode beam shape . . . . .	67
5.4.2	Dynamic mode beam shape . . . . .	71
5.4.3	Beam dispersion . . . . .	76
5.4.4	Space charge effects . . . . .	83
5.5	Energy distribution . . . . .	85
5.6	ROSINA RTOF ion measurements setup . . . . .	92

---

6. <i>Ion Source simulation with SIMION</i> . . . . .	95
7. <i>Conclusions &amp; Outlook</i> . . . . .	109
<i>Appendix</i>	111
A. <i>Pictures</i> . . . . .	113
B. <i>Drawings and Schematics</i> . . . . .	119
<i>Literature</i> . . . . .	129
<i>Acknowledgement</i> . . . . .	133
<i>Curriculum Vitae</i> . . . . .	135



## LIST OF TABLES

2.1	Parameters of comet 67P/Churyumov-Gerasimenko . . . . .	9
2.2	Floating potentials obtained through the analytical model and the numerical model presented in [BR04]. . . . .	22
3.1	Parameters of the used glass capillary plate . . . . .	33
3.2	Nominal potentials for the Low Energy Ion Source. The floating potentials are always related to the cage exit voltage which can be varied from $-20\dots 20$ volts (see Fig. 3.1). . . . .	33
5.1	Microtip current $i_{em}$ of single and combined groups. The 'sum' column indicates the summation of the corresponding groups in single operation and can be compared to the effective measured value in the 'eff' column. . . . .	56
5.2	Microtip emission current $i_-$ of single and combined groups. The 'sum' column indicates the summation of the corresponding groups in single operation and can be compared to the effective measured value in the 'eff' column. . . . .	57
5.3	Transmissions and collected electron currents (75 eV electron energy) of the individual ion source parts and an external collector anode in front of the source. Since the ionization box consists of two grids the first value in the "Transmission" column represents the overall transmission and the second value its square root as an estimation of the transmission per grid. . . . .	58
5.4	Characteristics for the measured beam shapes for different electron emission currents $i_-$ in static mode at $4.4 \times 10^{-8}$ mbar residual gas pressure. The accumulation time is 100 s and the ion energy is 200 eV. . . . .	67

5.5	Characteristics for the measured beam shapes for different electron emission currents $i_-$ in dynamic mode at $4.4 \times 10^{-8}$ mbar residual gas pressure and $3.6 \times 10^{-7}$ mbar argon in the source introduced through the glass capillary array. The ion energy is still 200 eV and the accumulation time is 100 s. . . . .	71
5.6	Characteristics for the measured beam shapes for different ion energies respectively different potentials between ion source and detector in static mode at $4.4 \times 10^{-8}$ mbar residual gas pressure. The electron emission current $i_-$ was adjusted to obtain similar intensities on the detector (see first column). . .	76
5.7	Peak widths at 50% height. Calculated values are bold, measured values in normal font. . . . .	81
5.8	Fitted parameters for the obtained retarding potential distribution. . . . .	91
6.1	Used potentials for the electrodes in SIMION. . . . .	96



## LIST OF FIGURES

2.1	Double Focusing Mass Spectrometer (DFMS) without the Multi Layer Insulation foil (MLI) and closed cover. . . . .	5
2.2	Reflectron-type Time-Of-Flight mass spectrometer (RTOF) mounted in the CASYMS chamber. . . . .	6
2.3	Image of comet 67P/Churyumov-Gerasimenko. . . . .	8
2.4	Boundaries in the comet - solar wind interaction. [Joc90] . . .	10
2.5	Test particle trajectories for Churyumov-Gerasimenko at 3.25 AU. (a) Electric field strength. Color coded is the absolute value, the arrows give the direction of the field. (b) Magnetic field strength (color coded) and trajectories of solar wind test particles (drawn as black lines). (c) Relative heavy ion (HI) density (color coded) and trajectories of HI test particles. The light blue lines belong to the heavy ions picked up by the solar wind far away from the nucleus, whereas the light red lines are ions generated close to the nucleus. $Q = 10^{24} \text{ s}^{-1}$ , $B_0 = 1.13 \text{ nT}$ , and scale length $x_0 = 280 \text{ km}$ . The Sun is on the left-hand side. [BM06] . . . . .	13
2.6	Same as Fig. 2.5 for 2.8 AU. $Q = 7.5 \times 10^{25} \text{ s}^{-1}$ , $B_0 = 1.23 \text{ nT}$ , and scale length $x_0 = 240 \text{ km}$ . The Sun is on the left-hand side. [BM06] . . . . .	14

2.7	Particle distribution functions in resulting from the complicated flow patterns in Fig. 2.6 for Churyumov-Gerasimenko at 2.8 AU heliocentric distance. (b)-(f) Particle distribution in energy [eV] at different locations indicated in (a) where the position of the nucleus is in the center (0). The points reflect the total kinetic energy of the ions with their angular distribution. The red points show the heavy cometary ions and the blue the solar wind protons, respectively. The total dimension in (a) is $12 \cdot x_0 \times 12 \cdot x_0$ with $x_0 = 240$ km similar to Fig. 2.6. The Sun is on the left-hand side. [BM06] . . . . .	15
2.8	Sketch of the Rosetta orbiter showing the plasma flow and solar direction in the nominal position. The symmetry planes, XY and YZ, are also indicated. [BR04] . . . . .	21
2.9	Potential [V], ion, and photoelectron densities (normalized to ambient plasma density) for the nominal position of the spacecraft with the nucleus on the right-hand side and the Sun on the left-hand side. Three different situations have been simulated: (a) nucleus at 1 AU from the Sun (perihelion) and the S/C (spacecraft) at $1 R_n$ from the nucleus, (b) nucleus at 1 AU from the Sun and the S/C at $100 R_n$ from the nucleus, (c) nucleus at 3 AU from the Sun and the S/C at $100 R_n$ from the nucleus. [BR04] . . . . .	23
3.1	Cut through the Low Energy Ion Source. Scale 1:1. . . . .	28
3.2	Low Energy Ion Source isometric view. . . . .	29
3.3	Low Energy Ion Source without Cage. . . . .	30
3.4	Wire-bonding of the 8 groups. At the bottom the active area of the microtip can be seen. . . . .	31
3.5	Scanning electron microscope (SEM) image of a microtip line section. . . . .	32
4.1	Hexagonal configuration of the glass capillary array . . . . .	38
4.2	Flow rate $Q_{\text{Total}} = N_{\text{Holes}} \cdot Q_{\text{Single Tube}}$ through all orifices plotted against the pressure behind the plate $p_A$ ( $N_2$ molecules, residual gas pressure set to $p_B = 5 \times 10^{-8}$ mbar). . . . .	41

---

4.3	Pressure of introduced gas inside the ionization volume of the Low Energy Ion Source versus the pressure $p_A$ behind the capillary plate ( $N_2$ molecules). For the total pressure the residual gas pressure $p_B = 5 \times 10^{-8}$ mbar needs to be added. . . . .	42
4.4	Ion current dependent of pressure behind capillary plate and electron emission current ( $N_2$ molecules, residual gas pressure $p_B = 5 \times 10^{-8}$ mbar). $\beta$ has been set to 1. . . . .	44
4.5	Total chamber pressure versus pressure behind capillary plate ( $N_2$ molecules, residual gas pressure $p_B = 5 \times 10^{-8}$ mbar). Pumping capacity $P = 250$ l/s and $P = 1000$ l/s. . . . .	48
5.1	Collector anode after microtip seasoning phase. The silhouette of the active area is visible (electron polished area) in the center, the blue area left to it comes from degassing of the soldering, and the brown part is caused by the microtip degassing. Degassing of the bonding wires (Fig. 3.4) would take place on the right side of the active area, but has not been observed on the collector anode. . . . .	52
5.2	Microtip conditioning setup. . . . .	53
5.3	Two sets of sensitivity measurements in static mode. Plotted is the ion current per electron current dependent of the partial argon pressure measured at the chamber wall. The residual gas pressure is $2.87 \times 10^{-8}$ mbar and the ion energy was set to $U_{\text{ion}} = 200$ eV. The blue curve (lower curve) was measured approximately one hour after the red curve. The indicated error for the slope and the offset of the fit give the 95% confidence interval. . . . .	61
5.4	Sensitivity measurement in dynamic mode. Plotted is the ion current per electron current dependent of the partial argon pressure measured at the chamber wall. The residual gas pressure is $2.87 \times 10^{-8}$ mbar and the ion energy was set to $U_{\text{ion}} = 200$ eV. The indicated errors for the slope and the offset of the fit give the 95% confidence interval. . . . .	63

- 
- 5.5 Relation between partial argon pressure in the source and pressure reading at the chamber wall. When gas is introduced into the ion source the pressure inside the ionization zone is higher by approximately a factor of forty than the one outside at the wall of the chamber. The residual gas pressure is  $2.87 \times 10^{-8}$  mbar and the ion energy was set to 200 eV. The indicated errors for the slope and the offset of the fit give the 95% confidence interval. . . . . 64
- 5.6 Beam shape at 1.0 nA electron emission current  $i_-$  in static mode at  $4.4 \times 10^{-8}$  mbar residual gas pressure. The plots are normalized to the intensity of the beam at 7.0 nA electron emission current in Fig. 5.8 on page 70. Top left the plot shows the  $1 \times 10^{-5}$  contour lines and top right a vertical cut through peak maximum is shown. Bottom left a horizontal cut through the peak maximum can be seen and bottom right the beam intensity is plotted as a 3D-surface. . . . . 68
- 5.7 Beam shape at 3.0 nA electron emission current  $i_-$  in static mode at  $4.4 \times 10^{-8}$  mbar residual gas pressure. The plots are normalized to the intensity of the beam at 7.0 nA electron emission current in Fig. 5.8 on page 70. Top left the plot shows the  $1 \times 10^{-5}$  contour lines and top right a vertical cut through peak maximum is shown. Bottom left a horizontal cut through the peak maximum can be seen and bottom right the beam intensity is plotted as a 3D-surface. . . . . 69
- 5.8 Beam shape at 7.0 nA electron emission current  $i_-$  in static mode at  $4.4 \times 10^{-8}$  mbar residual gas pressure. Top left the plot shows the  $1 \times 10^{-5}$  contour lines and top right a vertical cut through peak maximum is shown. Bottom left a horizontal cut through the peak maximum can be seen and bottom right the beam intensity is plotted as a 3D-surface. . . . . 70

- 
- 5.9 Beam shape at 1.0 nA electron emission current  $i_-$  in dynamic mode at  $3.6 \times 10^{-7}$  mbar argon pressure and  $4.4 \times 10^{-8}$  mbar residual gas pressure. The plots are normalized to the intensity of the beam at 3.0 nA electron emission current in Fig. 5.11 on page 74. Top left the plot shows the  $1 \times 10^{-5}$  contour lines and top right a vertical cut through peak maximum is shown. Bottom left a horizontal cut through the peak maximum can be seen and bottom right the beam intensity is plotted as a 3D-surface. . . . . 72
- 5.10 Beam shape at 2.0 nA electron emission current  $i_-$  in dynamic mode at  $3.6 \times 10^{-7}$  mbar argon pressure and  $4.4 \times 10^{-8}$  mbar residual gas pressure. The plots are normalized to the intensity of the beam at 3.0 nA electron emission current in Fig. 5.11 on page 74. Top left the plot shows the  $1 \times 10^{-5}$  contour lines and top right a vertical cut through peak maximum is shown. Bottom left a horizontal cut through the peak maximum can be seen and bottom right the beam intensity is plotted as a 3D-surface. . . . . 73
- 5.11 Beam shape at 3.0 nA electron emission current  $i_-$  in dynamic mode at  $3.6 \times 10^{-7}$  mbar argon pressure and  $4.4 \times 10^{-8}$  mbar residual gas pressure. Top left the plot shows the  $1 \times 10^{-5}$  contour lines and top right a vertical cut through peak maximum is shown. Bottom left a horizontal cut through the peak maximum can be seen and bottom right the beam intensity is plotted as a 3D-surface. . . . . 74
- 5.12 Beam shape at 100 eV ion energy in static mode at  $4.4 \times 10^{-8}$  mbar residual gas pressure, normalized to the total signal. Top left the plot shows the  $1 \times 10^{-5}$  contour lines and top right a vertical cut through peak maximum is shown. Bottom left a horizontal cut through the peak maximum can be seen and bottom right the beam intensity is plotted as a 3D-surface. . . 77
- 5.13 Beam shape at 200 eV ion energy in static mode at  $4.4 \times 10^{-8}$  mbar residual gas pressure, normalized to the total signal. Top left the plot shows the  $1 \times 10^{-5}$  contour lines and top right a vertical cut through peak maximum is shown. Bottom left a horizontal cut through the peak maximum can be seen and bottom right the beam intensity is plotted as a 3D-surface. . . 78

- 
- 5.14 Beam shape at 300 eV ion energy in static mode at  $4.4 \times 10^{-8}$  mbar residual gas pressure, normalized to the total signal. Top left the plot shows the  $1 \times 10^{-5}$  contour lines and top right a vertical cut through peak maximum is shown. Bottom left a horizontal cut through the peak maximum can be seen and bottom right the beam intensity is plotted as a 3D-surface. . . . . 79
- 5.15 Beam shape at 400 eV ion energy in static mode at  $4.4 \times 10^{-8}$  mbar residual gas pressure, normalized to the total signal. Top left the plot shows the  $1 \times 10^{-5}$  contour lines and top right a vertical cut through peak maximum is shown. Bottom left a horizontal cut through the peak maximum can be seen and bottom right the beam intensity is plotted as a 3D-surface. . . . . 80
- 5.16 Measured peak widths HWHM and exponential fit (see Eq. 5.3 and Tab. 5.7). . . . . 82
- 5.17 Beam shape at 8.6  $\mu\text{A}$  electron emission in static mode at  $7.5 \times 10^{-9}$  mbar residual pressure ( $\approx 11$  pA ion current before intensity reduction grids). Normalized to peak height. Top left the plot shows the 0.1 contour lines and top right a vertical cut through peak maximum is shown. Bottom left a horizontal cut through the peak maximum can be seen and bottom right the beam intensity is plotted as a 3D-surface. . . . . 83
- 5.18 Beam shape at 8.6  $\mu\text{A}$  electron emission in static mode at  $7.5 \times 10^{-9}$  mbar residual pressure and  $7.7 \times 10^{-7}$  mbar argon pressure ( $\approx 33$  pA ion current before intensity reduction grids). Normalized to peak height. Top left the plot shows the 0.1 contour lines and top right a vertical cut through peak maximum is shown. Bottom left a horizontal cut through the peak maximum can be seen and bottom right the beam intensity is plotted as a 3D-surface. . . . . 84
- 5.19 Relative ion current against the retarding potential. Measurements in the static mode are fitted with a sigmoid curve. The electron suppressor grid potential is set to -100 V. . . . . 86
- 5.20 Ion current distribution in static mode calculated from the measurement (see Fig. 5.19) and obtained through derivation of the sigmoid. The area beneath the curve is normalized to 1 and the electron suppressor grid potential is  $-100$  V. . . . . 87

5.21	Ion current distributions at different electron suppressor grid potentials in the static mode. Curves for $-100$ V, $-150$ V, and $-200$ V are measured whereas the curve for $0$ V has been extrapolated. All areas beneath the curves are normalized to 1.	88
5.22	Ion current distributions at different electron suppressor grid potentials in the dynamic mode. Curves for $-100$ V, $-150$ V, and $-200$ V are measured whereas the curve for $0$ V has been extrapolated. All areas beneath the curves are normalized to 1.	89
5.23	Comparison between energy distributions in static and dynamic mode. The integrals of both curves are normalized to 1.	90
5.24	ROSINA RTOF mounted in the CASYMS chamber on a moveable table. The Low Energy Ion Source is attached in front and the Faraday cup above the two sources and the ion attraction grid, respectively.	92
6.1	Cut through the Low Energy Ion Source potential array (see also Fig. 3.1 on page 28). On the lower part the microtip can be seen as well as the electron collector on the upper side. The electron flight direction is therefore upwards and ions move from the right to the left in this picture. The large electrode with grid on the left edge is the ion collector.	97
6.2	Cut through the Low Energy Ion Source potential array including trajectories of electrons emitted by the microtip in a $30$ degrees angle (see [PB94]).	98
6.3	Potential energy view of the potential array. The setup is given in Tab. 6.1. The highest part is the electron collector electrode at $50$ V and the lowest part is the external ion collector (with grid) at $-100$ V. Also the microtip grid and the electron collector grid at $10$ volts can be seen. All other parts are on ground potential.	99
6.4	Potential Energy view of the potential array including calculated ion trajectories. The ions are generated homogeneously (in position and with forward direction) in the ionization zone which is typical for the static mode, where no additional gas is introduced through the glass capillary array.	100

- 
- 6.5 Beam shape at 0 V acceleration potential ( $U_{\text{Collector Grid}} = 0 \text{ V}$ ,  $U_{\text{Cage}} = 0 \text{ V}$ ) normalized to its height. Top left the plot shows the 0.1 contour lines and top right a vertical cut through peak maximum is shown. Bottom left a horizontal cut through the peak maximum can be seen and bottom right the beam intensity is plotted as a 3D-surface. Note that the 8 cm vertical and horizontal ranges are both twice the standard 4 cm from the other figures. For comparison, the dotted circle with a 2 cm radius in the first plot shows the active area of the MCP detector used during the measurements in chapter 5.4. . . . . 102
- 6.6 Beam shape at 100 V acceleration potential ( $U_{\text{Collector Grid}} = -100 \text{ V}$ ,  $U_{\text{Cage}} = 0 \text{ V}$ ) normalized to its height. Top left the plot shows the 0.1 contour lines and top right a vertical cut through peak maximum is shown. Bottom left a horizontal cut through the peak maximum can be seen and bottom right the beam intensity is plotted as a 3D-surface. For comparison, the dotted circle with a 2 cm radius in the first plot shows the active area of the MCP detector used during the measurements in chapter 5.4. . . . . 103
- 6.7 Beam shape at 200 V acceleration potential ( $U_{\text{Collector Grid}} = -200 \text{ V}$ ,  $U_{\text{Cage}} = 0 \text{ V}$ ) normalized to its height. Top left the plot shows the 0.1 contour lines and top right a vertical cut through peak maximum is shown. Bottom left a horizontal cut through the peak maximum can be seen and bottom right the beam intensity is plotted as a 3D-surface. For comparison, the dotted circle with a 2 cm radius in the first plot shows the active area of the MCP detector used during the measurements in chapter 5.4. . . . . 104
- 6.8 Beam shape at 300 V acceleration potential ( $U_{\text{Collector Grid}} = -300 \text{ V}$ ,  $U_{\text{Cage}} = 0 \text{ V}$ ) normalized to its height. Top left the plot shows the 0.1 contour lines and top right a vertical cut through peak maximum is shown. Bottom left a horizontal cut through the peak maximum can be seen and bottom right the beam intensity is plotted as a 3D-surface. For comparison, the dotted circle with a 2 cm radius in the first plot shows the active area of the MCP detector used during the measurements in chapter 5.4. . . . . 105



- 
- 6.9 Beam shape at 400 V acceleration potential ( $U_{\text{Collector Grid}} = -400$  V,  $U_{\text{Cage}} = 0$  V) normalized to its height. Top left the plot shows the 0.1 contour lines and top right a vertical cut through peak maximum is shown. Bottom left a horizontal cut through the peak maximum can be seen and bottom right the beam intensity is plotted as a 3D-surface. For comparison, the dotted circle with a 2 cm radius in the first plot shows the active area of the MCP detector used during the measurements in chapter 5.4. . . . . . 106
- 6.10 Measured peak widths HWHM and exponential fits for both, measured (upper red curve) and simulated (blue) beam shapes (see also Fig. 5.16 on page 82). . . . . . 107
- A.1 Beam shape at 2.0 nA electron emission current  $i_-$  in static mode at  $4.4 \times 10^{-8}$  mbar residual gas pressure. The plots are normalized to the intensity of the beam at 7.0 nA electron emission current in Fig. 5.8 on page 70. Top left the plot shows the  $1 \times 10^{-5}$  contour lines and top right a vertical cut through peak maximum is shown. Bottom left a horizontal cut through the peak maximum can be seen and bottom right the beam intensity is plotted as a 3D-surface. . . . . . 114
- A.2 Beam shape at 4.0 nA electron emission current  $i_-$  in static mode at  $4.4 \times 10^{-8}$  mbar residual gas pressure. The plots are normalized to the intensity of the beam at 7.0 nA electron emission current in Fig. 5.8 on page 70. Top left the plot shows the  $1 \times 10^{-5}$  contour lines and top right a vertical cut through peak maximum is shown. Bottom left a horizontal cut through the peak maximum can be seen and bottom right the beam intensity is plotted as a 3D-surface. . . . . . 115
- A.3 Beam shape at 5.0 nA electron emission current  $i_-$  in static mode at  $4.4 \times 10^{-8}$  mbar residual gas pressure. The plots are normalized to the intensity of the beam at 7.0 nA electron emission current in Fig. 5.8 on page 70. Top left the plot shows the  $1 \times 10^{-5}$  contour lines and top right a vertical cut through peak maximum is shown. Bottom left a horizontal cut through the peak maximum can be seen and bottom right the beam intensity is plotted as a 3D-surface. . . . . . 116

---

A.4	Beam shape at 6.0 nA electron emission current $i_-$ in static mode at $4.4 \times 10^{-8}$ mbar residual gas pressure. The plots are normalized to the intensity of the beam at 7.0 nA electron emission current in Fig. 5.8 on page 70. Top left the plot shows the $1 \times 10^{-5}$ contour lines and top right a vertical cut through peak maximum is shown. Bottom left a horizontal cut through the peak maximum can be seen and bottom right the beam intensity is plotted as a 3D-surface. . . . .	117
B.1	Current measurement setup. . . . .	120
B.2	Beam shape measurement setup. . . . .	121
B.3	The top figure shows a cut through the Faraday cup and the bottom figure the isometric view. . . . .	122
B.4	Gas inlet flange with variable leak valve. . . . .	123
B.5	Front view of the Low Energy Ion Source (LEIS) mounted together with RTOF and the Faraday cup in the CASYMS chamber. The table can be moved so that either RTOF or the Faraday cup is in front of the LEIS. . . . .	124
B.6	Isometric view of the Low Energy Ion Source mounted together with RTOF and the Faraday cup in the CASYMS chamber. . . . .	125
B.7	Low Energy Ion Source power supply circuit diagram. The power OPAMP modules scheme can be seen in Fig. B.8. . . . .	126
B.8	Circuit diagram of the power OPAMP modules. . . . .	127
B.9	Faraday cup pA meter circuit diagram. . . . .	128

## 1. INTRODUCTION

The knowledge about comets has greatly improved due to the access of scientists to space by remote sensing observations and moreover by in situ investigations of comets. In particular, the Giotto mission to comet 1P/Halley in 1986 has enriched our view of the early solar system. Comets present a reservoir of well-preserved material from the time of the formation of the solar system. Some of the material present in comets may even be traced back to the dark molecular cloud from which our solar system emerged.

Several interesting questions on the history of the solar system can hence be answered only by studying comets, in particular in situ. Therefore the European Space Agency (ESA) launched its international Rosetta mission to comet 67P/Churyumov-Gerasimenko (C-G) on March 2, 2004.

The Rosetta Orbiter Spectrometer for Ion and Neutral Analysis (ROSINA) is the contribution of the University of Bern and its Co-I institutions to the Rosetta mission. ROSINA will measure the volatile component of the cometary coma of comet C-G. It consists of the Double Focusing Mass Spectrometer (DFMS), the Reflectron-type Time Of Flight mass spectrometer (RTOF), and the COmet Pressure Sensor (COPS). The prime measurement objective is to determine the elemental, isotopic, and molecular composition of the atmosphere and ionosphere of the comet C-G as well as temperature and bulk velocities of the neutral component and homogenous and inhomogeneous reactions of neutrals and ions in the dusty cometary atmosphere and ionosphere. In addition, several measurements will be taken during Rosetta's journey to comet C-G, namely the two asteroids, three Earth, and the Mars fly-bys.

Already the Ion Mass Spectrometer (IMS) on board of the Giotto spacecraft has proven to be very important in order to achieve the above mentioned tasks: The ion measurements in the vicinity of comet 1P/Halley has significantly increased our knowledge about the chemistry in cometary comae as well as the important processes of the interactions between the comet and the solar wind. Furthermore, the detection of ions has been very helpful for

the identification of parent molecules, which are of great interest, since they are expected to belong to the most pristine material in the solar system.

Driven by this great success both ROSINA mass spectrometers have thus been designed not only for neutral gas but as well for ion measurements. To achieve optimal performance with both mass spectrometers, the electrical parameters (voltages on the ion optical elements) have to be fine-tuned carefully during the ion calibration in the lab. For this purpose DFMS and RTOF depend on an external ion source providing an ion beam which is similar in terms of energy, incident angle, intensity, and composition to the expected environment of the comet. Due to the low relative velocity between the Rosetta orbiter and comet 67P/Churyumov-Gerasimenko, the energies of the cometary ions are only in the order of several eV. This is different to the ions detected at comet 1P/Halley: due to the high relative velocity of about 70 km/s the measured energies relative to the Giotto IMS were in order of several 100 eV.

Compared to the IMS a very different external source for the ROSINA ion mode calibration is needed. Especially the demanded low energy ion beam is very challenging, since in the regime of a few eV even the smallest potentials influence and deflect the charged atoms and molecules. And there are numerous non-negligible effects that can influence a beam at this low energy i.e. different surface materials, surface fouling, space-charging of ions and electrons, non-uniformities and fabrication tolerances of grids and other source parts, dissociative processes of molecules can be in the same order of energy, heating due to filaments, etc. Obviously for the same reasons, it is difficult to obtain useful results with computer simulations for such a source. In general, the technical knowledge for ion sources at these low energies is quite faint as they are only used in a few research areas and in terms of commercial use they are even of very little interest.

In this work a new setup for this type of ion sources will be shown. The design will be discussed and the results of the source characterization will be presented. Furthermore, also the setup for the first ion measurements together with ROSINA RTOF has been added.

## 2. THE ROSETTA MISSION

Rosetta was launched as flight 158 on March 2, 2004, by an Ariane-5G rocket from Kourou, French Guiana. The target is the Kuiper-belt comet 67P/Churyumov-Gerasimenko. ESA's Rosetta spacecraft will be the first to undertake the long-term exploration of a comet at close quarters. It comprises a large orbiter, which is designed to operate for a decade at large distances from the Sun, and a small lander. Each of these carries a large complement of scientific experiments designed to complete the most detailed study of a comet ever attempted.

After entering into orbit around comet 67P/Churyumov-Gerasimenko in 2014, the spacecraft will release a small lander onto the icy nucleus, then spend the next two years orbiting the comet as it heads towards the Sun. On the way to comet C-G, Rosetta will receive gravity assists from Earth and Mars, and fly past main belt asteroids.

The Rosetta orbiter has eleven scientific instruments on board. One of them is ROSINA, the Rosetta Orbiter Spectrometer for Ion and Neutral Analysis which contains the two mass spectrometers DFMS (Double Focusing Mass Spectrometer) and RTOF (Reflectron-type Time Of Flight) as well as the pressure sensor COPS (Comet Pressure Sensor).

### 2.1 *The ROSINA instrument*

The Rosetta Orbiter Spectrometer for Ion and Neutral Analysis is designed to analyze the volatile material of comet 67P/Churyumov-Gerasimenko [AJB<sup>+</sup>04]. For this purpose ROSINA has a wide mass range from 1 amu to > 300 amu, a very high mass resolution ( $m/\Delta m \approx 3000$  at 1% peak height, i.e. the ability to resolve CO from N<sub>2</sub> and <sup>13</sup>C from <sup>12</sup>CH), very wide dynamic range, high sensitivity, and the ability to determine cometary gas velocities and temperatures. ROSINA will address many topics like the outgassing rate of

comet C-G during its journey around the Sun, the elemental composition, the detection of organic molecules, isotopic measurements, and other very interesting features of the comet like seasonal effects and outbursts. In order to fulfill all these tasks, the two mass spectrometers are designed to detect ionized as well as neutral gas. For both measurement modes, ion and neutral, different ion source setups need to be found during the calibration of the sensors.

In the following, the two mass spectrometers are described briefly with special attention to the differences between the neutral gas and the ion mode configurations.

### 2.1.1 The Double Focusing Mass Spectrometer (DFMS)

The DFMS is a very compact state of the art high-resolution double focusing mass spectrometer realized in the Nier-Johnson configuration [AJB<sup>+</sup>04]. The major design requirements have been: mass range  $m/q = 12 - 100$  amu/q, mass resolution  $m/\Delta m > 3000$  at 1% peak level, good energy focusing properties to allow  $\Delta E/E$  of up to 1%, and a high mass dispersion to allow the use of a position sensitive focal plane detector.

Fig. 2.1 gives an overview of DFMS. The two main parts are the sensor (upper part) and the electronics (lower part). The sensor consists of the ion source (upper left), the detectors (upper right) and the mass analyzer (linking ion source and detectors).

Cometary gas and/or positive charged ions can enter the ion source of DFMS in two directions: One in parallel to the ion source axis with a wide field-of-view (FOV) of  $\pm 20^\circ$ , the other orthogonal to it with a narrow angle of  $\pm 2^\circ$  [LAB<sup>+</sup>]. In the normal mode of operation the wide FOV will be used, allowing cometary gas with wide angular spread in the flow direction to enter the ionization region (entrance aperture: 8.9 mm  $\times$  2.9 mm). The narrow FOV could be used to investigate flow directions of the cometary gas jets or the cometary ions. However, this mode requires a turning of the spacecraft by  $90^\circ$ . The axis of the wide FOV would normally have to be directed towards the nucleus and hence be parallel to the axis of the Rosetta cameras. Suitable potentials applied to the entrance electrodes (one ion suppressor and two ion repellers) prevent the entry of ambient low-energy ions into the DFMS in neutral gas mode. Cometary ions with higher energies ( $> 60$  eV) cannot pass through the analyzer, so it is not necessary to prevent their entry

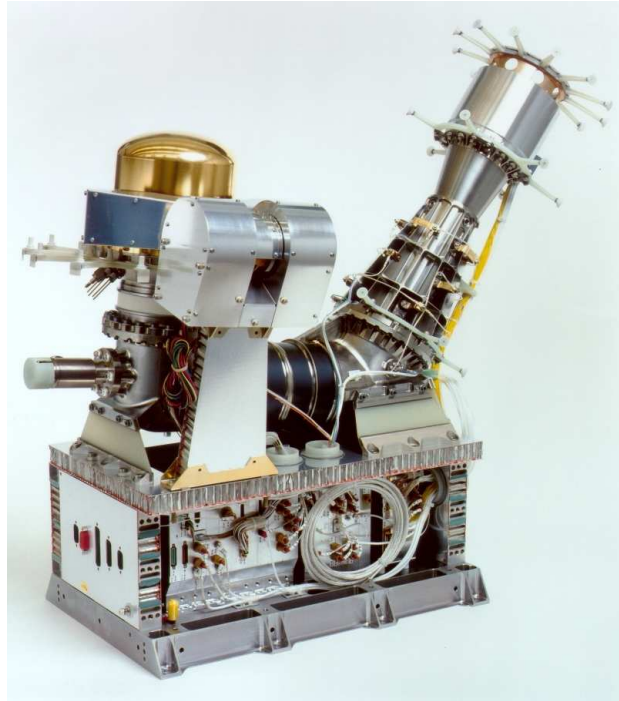


**Fig. 2.1:** Double Focusing Mass Spectrometer (DFMS) without the Multi Layer Insulation foil (MLI) and closed cover.

into the ion source. In the ion mode, the potentials on these electrodes are changed to attract the cometary ions even with a slight positive charging of the spacecraft and to focus them into the gas ionization region of the source. A coarse mesh grid (will be mounted on the stilts around the ion source in Fig. 2.1) at a negative potential surrounding the ion source area to a radial distance of 15 cm may help to augment the ion sampling.

Important parts after the ion source are the transfer optics, which guide the beam through one of the two analyzer entrance slits ( $200\ \mu\text{m}$  for low and  $14\ \mu\text{m}$  for high resolution). The main elements of the following mass per charge analyzer are a  $\pi/2$  radians electrostatic analyzer for energy separation and a  $\pi/3$  radians permanent sector magnet for impulse separation. In the following, several parts to change the beam geometry are implemented e.g. two quadrupoles for zoom and a hexapole to turn the focal plane. Finally, the beam is measured using either the Faraday cup (FC), the multichannel plate (MCP), or the channel electron multiplier (CEM).

### 2.1.2 The Reflectron-type Time-Of-Flight mass spectrometer (RTOF)

The Reflectron-type Time-Of-Flight mass spectrometer (RTOF) complements DFMS with an extended mass range from 1 to  $> 300$  amu/q. RTOF consists of five main components: the ion sources, ion optics, reflector, hard mirror and the detectors.

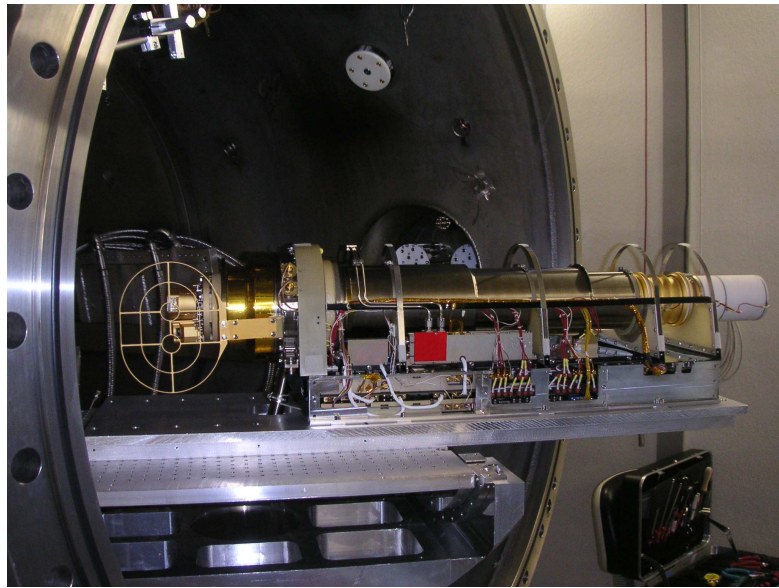


**Fig. 2.2:** Reflectron-type Time-Of-Flight mass spectrometer (RTOF) mounted in the CASYMS chamber.

For RTOF two ion sources are implemented: the electron impact storage ion source ionizes neutral particles and extracts them into the TOF analyzer, while the orthogonal acceleration ion source directs incoming initially ionized particles into the TOF section.

The orthogonal extraction allows for easy coupling of a TOF mass spectrometer with a wide range of external continuous or pulsed ion sources. In case of RTOF, the orthogonal extraction ion source is dedicated to the measurement of the ionized component of the cometary atmosphere [BAB<sup>+</sup>06].



The orthogonal extraction ion source uses off-axis-created ions, either coming from an external ion source (the comet in our case) or using ions formed by electron impact ionization in an off-axis electron impact ionization assembly. Like DFMS in ion mode, the cometary ions are pulled into the entrance system of the off-axis ionization assembly by an external attraction grid.

These ions propagate perpendicular to the principal ion-optical axis of the TOF system with an initial energy of  $< 10$  eV. When passing through the extraction region of the orthogonal extraction ion source, part of these ions are extracted by a fast voltage pulse on the extraction grid and are further accelerated into the drift path of the TOF system.

After a field free drift path the ions are redirected in the reflectron towards the detector (single reflection). These ions pass the drift path twice before they are finally detected on the MCP. Furthermore, it is possible to direct the reflected beam not on the detector but on the implemented hard mirror. This additional reflecting element bends the ions back for a second time to the reflectron, which nearly doubles the flight path of the ions and therefore further increases the (time-)resolution. The mass resolution in this triple reflection mode is  $m/\Delta m > 4500$  at 50% peak height.

Fig. 2.2 gives an overview of RTOF mounted in CASYMS chamber. On the left side, behind the ion attraction grid (or meshed grid), both ion sources can be seen: the orthogonal ion source above and the storage ion source below. On the right side (the white ceramic part) is the reflectron. The center belongs to the field free drift path. The whole electronics package is placed underneath the sensor.

## 2.2 *The target: comet 67P/Churyumov-Gerasimenko*

Comet 67P/Churyumov-Gerasimenko commutes between the orbits of Jupiter and the Earth and originates from the Kuiper belt, which is a belt of small icy bodies extending from past the orbit of Neptune at 30 AU to 50 AU. During its short-lived excursions to the inner solar system, the heat of the Sun causes ices on the comet's surface to evaporate and jets of gas to blast dust grains into the surrounding space. 67P/Churyumov-Gerasimenko is classed as a dusty comet and is joined in this group by objects such as 1P/Halley and 21P/Giacobini-Zinner, as well as non-periodic objects such as C/1975 V1 (West), C/1995 O1 (Hale-Bopp) and C/1996 B2 (Hyakutake).

Unfortunately, although this enveloping coma of dust and gas increases 67P/Churyumov-Gerasimenko's brightness, it also completely hides the comet's nucleus.



**Fig. 2.3:** Image of comet 67P/Churyumov-Gerasimenko.

Rosetta's task is to rendezvous with the comet while it still lingers in the cold regions of the solar system and shows no surface activity. After releasing a lander onto the dormant nucleus, the orbiter will chase comet

67P/Churyumov-Gerasimenko as it charges headlong towards the inner solar system at speeds of over to 100'000 km/h.

Diameter of nucleus	4 km
Orbital period	6.57 years
Perihelion	1.24 AU
Aphelion	5.73 AU
Orbital eccentricity	0.6
Orbital inclination	7.1 degrees
Maximum magnitude	12
Year of discovery	1969
Discoverers	Klim Churyumov Svetlana Gerasimenko

**Tab. 2.1:** Parameters of comet 67P/Churyumov-Gerasimenko

Tab. 2.1 shows the principal parameters of comet C-G. Rosetta will follow the comet to at least its perihelion at 1.24 AU. During these 2 years Rosetta will collect data for the first long term exploration of a comet at close quarters.

### 2.2.1 Ion dynamics in a cometary coma

Ions are produced from the neutral vapor<sup>1</sup> by the classical mechanisms of photoionization (normal and dissociative), charge exchange with solar wind ions and collisional ionization. The main interaction regions are shown in Fig. 2.4.

The newborn ions are picked up by the plasma flow and magnetic field surrounding the comet. In the inner coma an equilibrium between ionization and electron dissociative recombination exists, leading to a radial dependence of the ions in proportion to  $1/r$  ( $r$  distance from the nucleus), while at intermediate distances, as long as life time effects of the neutral molecules are not important, the dependency may approach  $1/r^2$  corresponding to radial outflow [Ip87]. At least with the larger comets close to the Sun there is an inner field-free region, the magnetic cavity or ionosphere, where ion-neutral

<sup>1</sup>mainly H<sub>2</sub>O, sublimating from the cometary nucleus and, possibly, from cometary grains [Joc90]

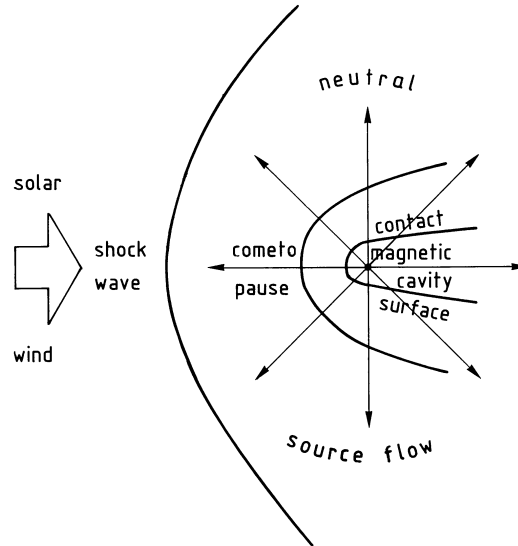


**Fig. 2.4:** Boundaries in the comet - solar wind interaction. [Joc90]

drag prevents the entry of solar wind ions and of the associated solar wind magnetic field. The outer boundary is called ionopause or contact surface. The outermost surface of interest is the shock transition, where the supersonic solar wind notices the cometary obstacle. At the shock transition the admixture of cometary ions to the solar wind, brought about by the pick-up mechanism, amounts to 1% in number density. The space experimenters introduced another boundary between cavity and shock wave, the cometopause or magnetic pile-up region. This boundary represents the smooth, but rather steep transition into the inner portion of the comet, where, even though the solar wind has access, cometary ions dominate the flow. The cometopause apparently coincides with the outer boundary of cometary ions as seen in ground based images.

The mass-loading process at strong comets, i.e. the incorporation of the cometary ions into the solar wind flow, proceeds in three main steps. First, the cometary ions starting with almost zero velocity in the cometary rest frame experience the interplanetary electromagnetic field and start a gyrating motion [BMGK04]. This forms a typical ring distribution around the solar wind velocity found at Halley [BAB<sup>+</sup>86]. Now this non-gyrotropic ring distribution is unstable and decays relatively quickly into a spherical shell

distribution around the solar wind bulk velocity [MKS97]. This distribution, however, is relatively stable, and decays only slowly into a fully thermalized distribution, where the cometary ions are finally Maxwellian and flow with the same velocity as the solar wind.

### 2.2.2 From a weak to a strong comet

In contrast to a strong comet, where the above described boundaries are already formed, this may not be the case for a comet further away from the Sun (weak comet). It is generally accepted that cometary activity is triggered by solar heating, as exemplified by the fact that comets are usually inert when they are at large heliocentric distances, and only start to develop a coma when they get closer to the Sun [dL05]. A cometary nucleus is covered with ice, which sublimates when the comet approaches the Sun. When the sublimated gas evolves off the surface, dust is dragged along. The gas and dust form a comet's coma, and hide the nucleus from view. Many comets are still inert when they cross Jupiter's orbit and brighten considerably when they get closer than 3 AU from the Sun.

The cometary ions of weak comets as well as the solar wind protons have large gyroradii compared to the scales of the interaction region. Consequently, also the interaction times, i.e. the time the involved ions stay in the interaction region is also much smaller than at strong comets. The thermalization of the cometary ions is therefore different from what was described above. Furthermore, in this different regime of mass loading the solar wind is not influenced as in the stronger case, hence, no bow shock is formed. This implies a supersonic solar wind flow in the whole interaction region of a weak comet which leads to complex ion dynamics.

Bagdonat and Motschmann [BMGK04] used a 3D hybrid code in order to simulate comet 67P/Churyumov-Gerasimenko on the way from a weak to a strong comet.

The density of the neutral atoms as function of radial distance  $r$  from the nucleus is given by the following model:

$$n_n(r) = \frac{Q}{4\pi r^2 v_0} \quad , \quad (2.1)$$

where  $Q$  is the H<sub>2</sub>O production rate and  $v_0$  the outgassing velocity, taken to

be  $v_0 = 1$  km/s. The values for the H<sub>2</sub>O production rate are  $7.5 \times 10^{25}$  s<sup>-1</sup> at  $R_{\text{heliocentric}} = 2.8$  AU and  $10^{24}$  s<sup>-1</sup> at  $R_{\text{heliocentric}} = 3.25$  AU. The ionization frequency is given as  $\nu = 10^{-6}$  s<sup>-1</sup>.

For the understanding of the results shown in this section it is convenient to recall the different forces acting on the ions and the magnetic field lines:

$$\vec{E} = - \underbrace{\left( \frac{n_p \vec{v}_p}{n_p + n_h} + \frac{n_h \vec{v}_h}{n_p + n_h} \right)}_{(1)} \times \vec{B} + \underbrace{\frac{(\nabla \times \vec{B}) \times \vec{B}}{\mu_0 e (n_h + n_p)}}_{(2)} - \underbrace{\frac{\nabla p_{e,p} + \nabla p_{e,h}}{e (n_h + n_e)}}_{(3)}, \quad (2.2)$$

where  $n_p$ ,  $\vec{v}_p$ ,  $n_h$ , and  $\vec{v}_h$  are the density of the solar wind protons, the velocity vectors of the solar wind protons, the density of the cometary heavy ions, and their velocity vectors, respectively.

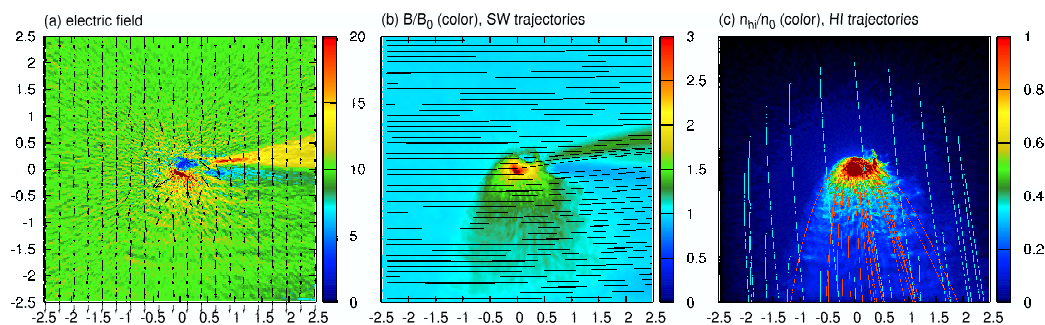
The first term (1) in Eq. 2.2 is dominated by the solar wind bulk velocity  $\vec{v}_p$  because the cometary ion density is low compared to the solar wind density in most places. Therefore the solar wind protons experience the force resulting from this term only when  $n_h$  becomes large. Where this is the case, the electric field becomes smaller, thus, the solar wind protons are deflected upwards. The cometary ions, however, experience the full force of this term and are thus strongly accelerated downwards into regions where  $n_h$  is small. This force will be denoted as the **"pickup-force"** in the following. It always acts perpendicular to the magnetic field and plasma velocity vector. Furthermore, substituted in Faraday's law, this term is responsible for the **"convection"** of the magnetic field along the plasma flow. In regions with high  $n_h$  and low  $\vec{v}_h$ , like in the inner coma, this convection term becomes smaller, thus, the magnetic field lines cannot be transported through this region and experience some sort of **"draping"** around the obstacle.

The electric field arising from the pressure gradient terms (3) in Eq. 2.2 is experienced by both species in the same way. This force mainly acts radially outward from the nucleus, due to the dominant radial density profile of the cometary ions. This accelerates the cometary ions outwards and deflects the solar wind protons around the obstacle. This force will be simply referred to as **"electron pressure"**.

The (2) term in Eq. 2.2 can be split further into the two parts:

$$\underbrace{(\nabla \times \vec{B})}_{(2)} \times \vec{B} = \underbrace{(\vec{B} \cdot \nabla)}_{(4)} \vec{B} - \underbrace{\frac{1}{2} \nabla (B^2)}_{(5)} . \quad (2.3)$$

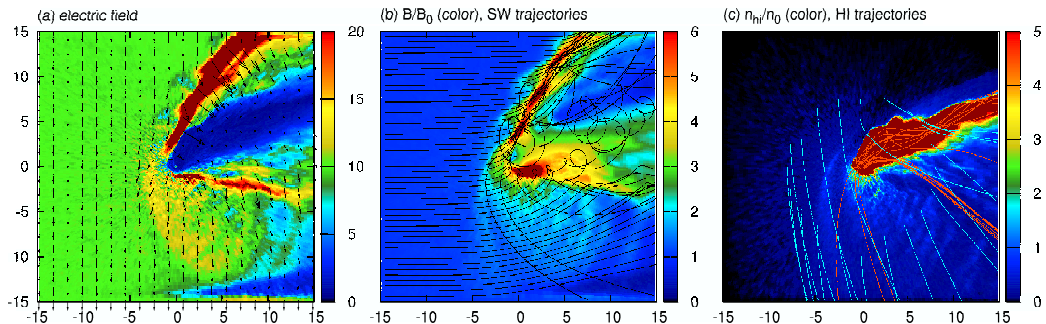
Term (4) in Eq. 2.3 acts as a ”**magnetic tension**”, which tends to shorten the magnetic field lines, when they become curved. Due to this term in Eq. 2.3, also the plasma is accelerated whenever field lines are curved. The (5) term in Eq. 2.3 is called ”**magnetic pressure**”, which tends to expand the magnetic field lines, where their density becomes higher. Again, this magnetic pressure also acts on the plasma pointing in direction of the magnetic pressure gradient.



**Fig. 2.5:** Test particle trajectories for Churyumov-Gerasimenko at 3.25 AU. (a) Electric field strength. Color coded is the absolute value, the arrows give the direction of the field. (b) Magnetic field strength (color coded) and trajectories of solar wind test particles (drawn as black lines). (c) Relative heavy ion (HI) density (color coded) and trajectories of HI test particles. The light blue lines belong to the heavy ions picked up by the solar wind far away from the nucleus, whereas the light red lines are ions generated close to the nucleus.  $Q = 10^{24} \text{ s}^{-1}$ ,  $B_0 = 1.13 \text{ nT}$ , and scale length  $x_0 = 280 \text{ km}$ . The Sun is on the left-hand side. [BM06]

Fig. 2.5 gives the results for Churyumov-Gerasimenko at 3.25 AU (see [BM06]). As the solar wind (SW) particles show, the SW flow is almost undisturbed at this stage. Therefore the electric field is almost constant throughout the whole region, except very close to the nucleus, where it drops off almost to

zero (see term (1) in Eq. 2.2). This results in a decreased pickup efficiency, i.e. the inner heavy ions are mainly influenced by the radial electron pressure gradient, which pushes them radially outward at first (see term (3) in Eq. 2.2). Further away the ions experience the strong solar wind pickup field and are deflected towards the cycloidal tail, where they mix with the outer heavy ions from above.



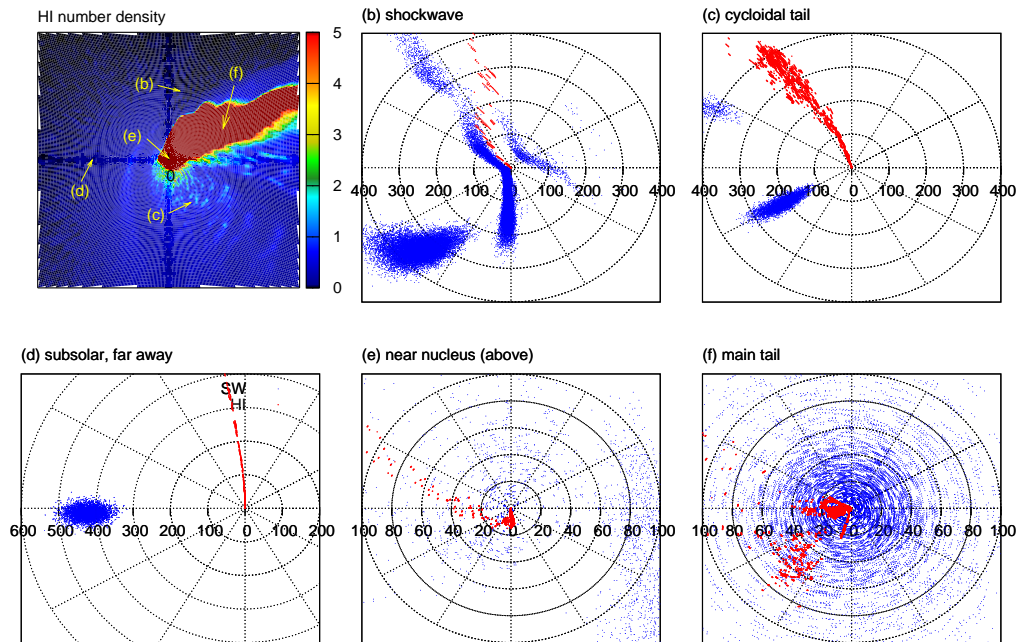
**Fig. 2.6:** Same as Fig. 2.5 for 2.8 AU.  $Q = 7.5 \times 10^{25} \text{ s}^{-1}$ ,  $B_0 = 1.23 \text{ nT}$ , and scale length  $x_0 = 240 \text{ km}$ . The Sun is on the left-hand side. [BM06]

Fig. 2.6 shows the results for Churyumov-Gerasimenko at 2.8 AU (see [BM06]). (a) The electric field is almost zero inside the whole tail region. Directly in front of the nucleus however, the electric field is strongly enhanced due to the increase of the magnetic field strength. (c) This pushes the inner heavy ions back inside the tail, whenever they reach this position. Inside the tail the heavy ions perform a complicated gyro-motion with a comparatively small gyro-radius (due to the low velocity). The outer heavy ions cross the the tail more or less undisturbed. (b) The solar wind particles are strongly deflected upwards. At the non-linear Mach cone they are even reflected forming a complicated flow pattern. This structure will form the bow shock later on. It begins to "reach around" the inner coma, forming a unified structure together with the pile-up region (below the nucleus).



### 2.2.3 Particle distribution functions

To obtain the particle energy distributions shown in Fig. 2.7, the energies of all particles at a certain point are recorded after the simulation has become stationary [BM06].



**Fig. 2.7:** Particle distribution functions in resulting from the complicated flow patterns in Fig. 2.6 for Churyumov-Gerasimenko at 2.8 AU heliocentric distance. (b)-(f) Particle distribution in energy [eV] at different locations indicated in (a) where the position of the nucleus is in the center (0). The points reflect the total kinetic energy of the ions with their angular distribution. The red points show the heavy cometary ions and the blue the solar wind protons, respectively. The total dimension in (a) is  $12 \cdot x_0 \times 12 \cdot x_0$  with  $x_0 = 240$  km similar to Fig. 2.6. The Sun is on the left-hand side. [BM06]

Fig. 2.7 shows the distributions for a heliocentric distance of 2.8 AU, corresponding to Fig. 2.6(c). The blue dots are solar wind protons, whereas the red dots are cometary heavy ions. Fig. 2.7(a) gives an overview of the

locations, where the distributions have been taken. The other panels show the angular distribution of the kinetic energy in the plane perpendicular to the solar wind magnetic field.

Fig. 2.7(d) shows the distribution at a subsolar point, far away from the nucleus ( $\sim 1800$  km). The solar wind exhibits its thermal Maxwellian distribution around  $400 - 500$  eV coming from the left (the sun side). The visible cometary ions are generated far out and were accelerated downwards due to the solar wind electric field (see term (1) in Eq. 2.2) before they reach location (d).

Fig. 2.7(e) corresponds to a position of  $\sim 40$  km "above" the nucleus, well inside the inner coma. The heavy ion distribution shows two distinct components. One is the relatively dense and slow component incoming directly from the nucleus with energies lower than 20 eV. These are heavy ions, which are mainly affected by the electron pressure gradient force. The other component are pickup ions originating from the outer coma, which cross the main tail, as can be seen from the light blue heavy ion trajectories in Fig. 2.6(c).

Fig. 2.7(f) shows the situation downstream, inside the tail. The heavy ions show a pattern similar to the one on panel (e). However, the slow and dense portion seems to be split in two populations, possibly due to the somewhat complicated gyromotion of the heavy ions inside the tail, see Fig. 2.6(c). The solar wind particles enter the tail from below, where they cross the cycloidal tail and the pile up region (Fig. 2.6(b)). Inside the tail (f) they are completely thermalized.

Fig. 2.7(b) and (c) look similar, although being taken in the non-linear shock wave and in the cycloidal tail, respectively. At both places, the heavy ions incoming from "above" are somewhat disturbed compared to the subsolar point in panel (d), because of the disturbances in the magnetic field. The solar wind protons, however, are much more influenced by the field configuration due to their lower mass. As can be seen from Fig. 2.6(b), the solar wind protons perform a gyromotion at the shock wave and also when they enter the pile up region. This forms two distorted populations of solar wind protons in (c) and even three deformed distributions in (b).

In sum, almost all shown particle distributions are far from being Maxwellian. But in each case, cometary heavy ions with very low energies exist (typically  $< 20$  eV), especially inside the tail and in the inner coma.

### 2.3 *Spacecraft environment*

The major difficulty in measuring low energy thermal particles comes from the charging of the spacecraft in regions where the plasma density is low [BR04]. During a large part of the operational phase comet 67P/Churyumov-Gerasimenko and the Rosetta orbiter will be at distances from the Sun larger than 1.5 AU.

The expected temperatures of cometary ions and electrons are very low. Only very close to the nucleus the expected plasma density is large enough to allow the spacecraft to collect enough thermal electrons to counter the photoelectron current emitted by the large solar panels. At larger heliocentric and cometocentric distances where photoemission is the dominant effect, the spacecraft will float positive and thus hindering the measurements of the low energy ions.

For ROSINA, among various other instruments on the Rosetta spacecraft, it is very important to take this effect into account in order to analyze the scientific data. For the ion mode calibration the Low Energy Ion Source has to be floatable in at least the same order of magnitude to provide both ROSINA mass spectrometers DFMS and RTOF with a similar environment in the lab as in the vicinity of the comet.

In this chapter a simplified calculation and results from a numerical model [BR04] as well as experimental tests in a plasma chamber [RB04] are reflected. Both papers were aimed for comet 46P/Wirtanen, the former target of the Rosetta mission. Even though the orbit and the gas production rate are different compared to comet 67P/Churyumov-Gerasimenko, the presented results show the dimensions of the expected effect.

For the simplified analytical determination of the equilibrium potential a reduced representation of the orbiter and the solar panels as electrostatic probes with the corresponding probe current collection models has been used [BR04]. The spacecraft body is considered as a sphere with an equivalent external collecting area whereas the solar panels were taken as planar electrodes when the thickness of the plasma sheath remains small compared with their width, which is the case as long as the Debye length  $\lambda_D$  and the floating potential keep moderate values. When the sheath extension  $l_s$  is large, it is more appropriate to consider the solar panels as cylindrical electrodes with a radius equal to  $\frac{l}{2} + l_s$ . Furthermore, both faces of the solar panels

are conductive and grounded to the same ground potential as the external surface of the orbiter itself.

The equilibrium potential of the spacecraft is reached when the thermal electron current compensates the photoelectron and the thermal ion current. Solar wind has not been taken into account as it is expected to not enter the inner part of the developed coma:

$$I_e = I_{ir} + I_{ph} \quad . \quad (2.4)$$

### 2.3.1 Thermal Electron Current

For the thermal electron current two regimes have to be separated. For a probe at negative potential  $\Phi_p$  with respect to the plasma potential the electron current can be written as

$$I_e = S \cdot j_e \cdot e \left( \frac{q \cdot \Phi_p}{kT_e} \right) \quad , \quad (2.5)$$

where  $j_e$  is the current at plasma potential on a unit area:

$$j_e = -q \cdot n_e \cdot \sqrt{\frac{kT_e}{2\pi m_e}} \quad , \quad (2.6)$$

whereby  $m_e$ ,  $n_e$  and  $T_e$  are the mass, density, and temperature of the electrons, respectively, and  $q$  is the absolute value of the elementary charge. The spacecraft potential  $\Phi_{S/C}$  can only reach negative values of about a few  $kT_e$  when the electron density is large enough. So no further thick sheath approximation is needed.

For a probe at positive potential  $\Phi_p$  with respect to the plasma, the electron collection depends on the ratio  $\xi$  between the probe radius  $r_p$  and the Debye length  $\lambda_D$ . For small values of  $\xi$ , i.e., in the thick sheath case, the collected electron current has been approximated by Orbital Motion Limited values [CTT75] for a sphere:

$$I_e = j_e \left( 1 + \frac{q \cdot \Phi_p}{kT_e} \right) \quad (2.7)$$

and for a cylinder:

$$I_e = S \cdot j_e \cdot \frac{2}{\sqrt{\pi}} \left( \sqrt{\frac{q \cdot \Phi_p}{kT_e}} + \frac{\sqrt{\pi}}{2} e^{\left(\frac{q \cdot \Phi_p}{kT_e}\right)} \left(1 - \operatorname{erf}\left(\frac{q \cdot \Phi_p}{kT_e}\right)\right) \right) . \quad (2.8)$$

In the thin sheath approximation for large values of  $\xi$  the collected electron current is equal to

$$I_e = S_{\text{sh}} \cdot j_e , \quad (2.9)$$

where  $S_{\text{sh}}$  is the external area of the sheath surrounding the probe where the local potential is  $\sim kT_e$  (Bohm criterion). Determining  $S_{\text{sh}}$  is delicate:

$$l_s \sim \lambda_D \left( \frac{q \cdot \Phi_p}{kT_e} \right)^\alpha , \quad (2.10)$$

with  $\alpha = 0$  ( $l_s \sim \lambda_D$ ) for small potentials and for large potentials  $\alpha = 0.75$  in the thin sheath and  $\alpha = 0.5$  in the thick sheath approximation (close to the Orbital Motion Limited case).

### 2.3.2 Ion Current

In the inner coma, the cometary neutral and ionized gas flow is collisional and the cometary plasma ram velocity is therefore equal to the velocity of the neutral gas outflowing from the nucleus (0.3 km/s to 1 km/s). Both the ram current and the random thermal current ( $\sim 50$  K) need to be taken into account when the spacecraft potential is close to the plasma potential. The ram current can be approximated by

$$\begin{aligned} I_{\text{ir}} &= S_R \cdot n_i \cdot q \cdot V_i && \text{for } \frac{1}{2} m_i v_i^2 \geq q \cdot \Phi_{\text{S/C}} \text{ and} \\ I_{\text{ir}} &= 0 && \text{for } \frac{1}{2} m_i v_i^2 < q \cdot \Phi_{\text{S/C}}, \end{aligned} \quad (2.11)$$

where  $S_R$  is the cross sectional area of the orbiter and solar panels perpendicular to the ram velocity,  $m_i$  and  $n_i$  are the mass and density of cometary

thermal ions (mainly water ions  $\text{H}_2\text{O}^+$ ), respectively, and  $v_i$  is their drift velocity.

### 2.3.3 Photoelectric Current

In absence of a magnetic field in the inner coma one can assume that photoelectrons which have enough energy to leave the sunlit surface of the orbiter and the solar panels will not be collected on another section of the spacecraft. The variation of the photoelectron current density as function of the spacecraft potential has been expressed according to [Ped95] as

$$J_{\text{ph}} = J_1 \cdot e^{\left(-\frac{\Phi_{\text{S/C}}}{2.5}\right)} + J_2 \cdot e^{\left(-\frac{\Phi_{\text{S/C}}}{7.5}\right)}, \quad (2.12)$$

using

$J_1 = 5 \text{ nA/cm}^2$ : solar UV and

$J_2 = 0.3 \text{ nA/cm}^2$ : soft X-ray,

both at 1 AU.

### 2.3.4 Results and Discussion

The results from these calculations can be seen in Tab. 2.2. The spacecraft body in the presented results is connected electrically to the solar panels. Furthermore, the spacecraft is located between the cometary nucleus and the Sun. Thus the solar panels point towards the Sun respectively the back-side towards the comet (see Fig. 2.8).

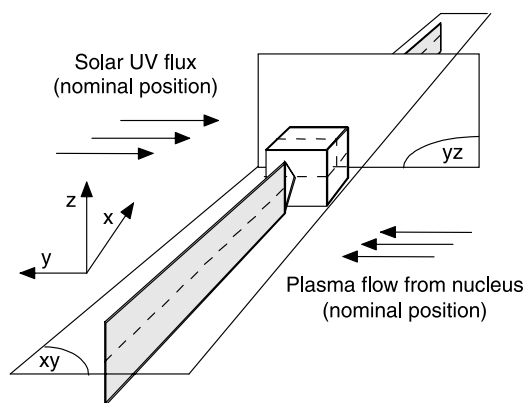


**Fig. 2.8:** Sketch of the Rosetta orbiter showing the plasma flow and solar direction in the nominal position. The symmetry planes, XY and YZ, are also indicated. [BR04]

In general, the solar panels point towards the Sun to provide the spacecraft with full power. But the spacecraft can have different angles pertaining to the comet, which diminishes the effective surface area of the solar panels pointing towards the comet, e.g. sun-spacecraft-comet forming a right angle. This effect can further increase the equilibrium potential of the spacecraft indicated in Tab. 2.2, since the effective area of the solar panels is larger for the photoelectron current than for the thermal electron current.

At 1 AU and close to the comet the equilibrium potential is quite close to the local plasma potential because the current collected from the plasma dominates above the photoelectron current. This is different at larger cometocentric distances where the density of thermal electrons is lower: The equilibrium potential reaches high positive value of  $\sim 7$  V, which is some two orders of magnitude larger than the characteristic energies of cometary thermal ions and electrons.

Distance to Sun [AU]	Distance to Comet [ $R_{\text{nucleus}}$ ]	Plasma Density [ $\text{cm}^{-3}$ ]	Debye Length [cm]	Analytical		Numerically computed [V]
				$\alpha = 0.5$ [V]	$\alpha = 0.6$ [V]	
1	1	$10^5$	0.15	-0.007	-0.007	-0.023
1	100	$10^3$	1.5	7.2	5.4	1.8
3	1	$10^3$	1.5	1.5	1.5	0.0015
3	100	10	15	7.4	5.7	4.3

**Tab. 2.2:** Floating potentials obtained through the analytical model and the numerical model presented in [BR04].

At 3 AU the electron density in the coma is decreased compared to values at 1 AU owing to the lower sublimation rate of the nucleus and the reduced ionizing solar radiation intensity (10%). Even though the photoelectron current loses intensity correspondingly, the equilibrium potential still reaches high positive values compared to the thermal ion energies, especially at large distances to the nucleus.

The results from the simplified analytical determination of the equilibrium potential also fits quite well the numerical results obtained in [BR04] and shown in the last column of Tab. 2.2 as well as the results from the laboratory measurements in [RB04]. Fig. 2.9 shows the results of the numerical simulations for the most interesting parameters: the potential, the ion density, and the photoelectron density for different situations: the heliocentric distance of the comet is at 1 AU (perihelion) and the cometocentric distance of the spacecraft is at either  $1 R_{\text{nucleus}}$  ( $R_n$  in the following) or  $100 R_n$ . The results are presented in the two planes of symmetry XY and YZ (see Fig. 2.8). In Fig. 2.9(a) the spacecraft floating potential is  $-0.02$  V (close to the analytically calculated  $-0.01$  V; see Tab. 2.2) and therefore in the order of a few  $kT_e$ . The thermal electron current dominates the photoelectron emission. The sheath extension is in the order of a few Debye lengths and the ion density towards the comet is slightly increased due to the negative floating potential. In Fig. 2.9(b) the distance between the spacecraft and the nucleus is at  $100 R_n$  and thus the electron density much lower. Photoelectron emission starts to be a major effect. The floating potential of the spacecraft increases to 1.8 V as well as the sheath extends to about 1 m. The ion density



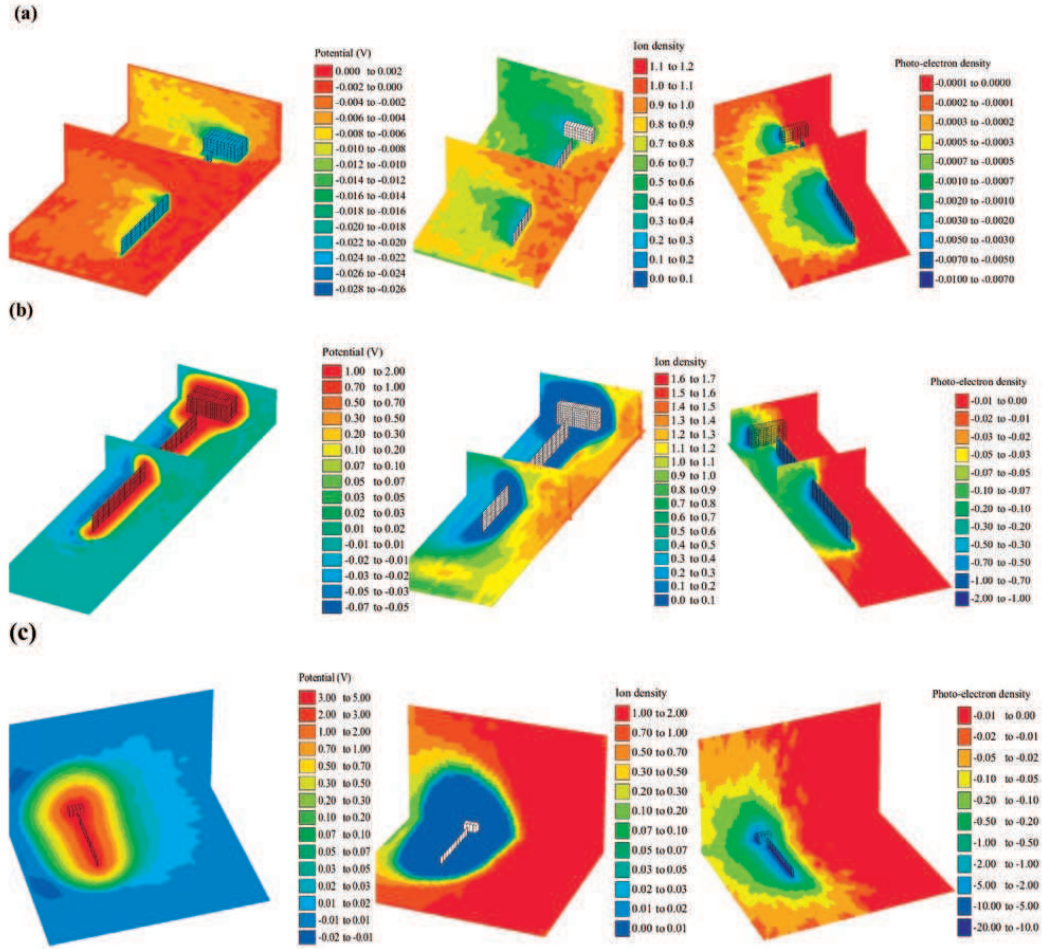


**Fig. 2.9:** Potential [V], ion, and photoelectron densities (normalized to ambient plasma density) for the nominal position of the spacecraft with the nucleus on the right-hand side and the Sun on the left-hand side. Three different situations have been simulated: (a) nucleus at 1 AU from the Sun (perihelion) and the S/C (spacecraft) at  $1 R_n$  from the nucleus, (b) nucleus at 1 AU from the Sun and the S/C at  $100 R_n$  from the nucleus, (c) nucleus at 3 AU from the Sun and the S/C at  $100 R_n$  from the nucleus. [BR04]

is decreased dramatically close to the spacecraft and ion measurements will be strongly influenced and only possible if attraction potentials near the en-

trance of the ion analyzers are able to penetrate the sheath. In the last case, presented in Fig. 2.9(c), the comet is at 3 AU to the Sun and the spacecraft at  $100 R_n$  to the nucleus. The spacecraft floating potential rises to 4.3 V and the sheath expands to 7.5 m. Ion measurements are no more possible, even with the use of attracting potentials. Also caused by the sheath extension numerous photoelectrons from the Sun side are bent back towards the night side of the solar panels where they influence the structure of the sheath.

## 3. SETUP OF THE LOW ENERGY ION SOURCE

### 3.1 *Requirements*

This chapter presents the principal setup for the Low Energy Ion Source (LEIS). The previous chapter showed that both ROSINA mass spectrometers are confronted with various difficulties during the ion measurements at comet 67P/Churyumov-Gerasimenko (C-G). Thus for a useful preparation, testing, and calibration of the mass spectrometers, the LEIS should be able to provide DFMS and RTOF with an ion beam very similar to the expected environment at the comet. This chapter lists all the specific requirements for the LEIS as well as the way they have been fulfilled.

- The expected ion energies at comet C-G range from 0 to several 100 eV (e.g.  $\sim 450$  eV protons in the slow solar wind shown in Fig. 2.7(d) on page 15). The LEIS has to be designed for the cometary ions at energies well below 20 eV. As already seen in Fig. 2.7 on page 15, these ions can be found up to large distances, but especially very close to the nucleus. Generating an ion beam at this low energy is very challenging as it is affected by the smallest potentials nearby. These influences are reduced by gold-plating the whole source, electromagnetic shielding of the wiring, and by using a microtip electron emission surface. The use of a microtip field emitter instead of a filament for the electron impact ionization has several advantages. On one hand, ions do not get more energy by heating since the emission is cold. On the other hand, the electron current is more or less emitted over the whole microtip surface instead of the punctual emission of a filament. This leads to a lower space charge of the electrons (see Eq. 4.23 on page 46) and to a more homogeneous ion beam.

Magnets, which are often used in ion sources to enlarge the electron flight path and thus to rise the electron ionization probability, cannot be used in the LEIS because the magnetic field would deflect the ions before they even reach the source exit.

- At the comet various chemical elements and molecules are expected. The LEIS is also designed to be operated with different gases and gas mixtures. Therefore two gas inlets are implemented, one leading the gas directly into the ion source (dynamic mode) and one at the chamber wall to flood the entire chamber equally (static mode).
- Due to spacecraft charging (see Fig. 2.9 on page 23), Rosetta can be on a different potential compared to its surroundings. For this purpose the LEIS needs to be floatable for several volts.
- In order to keep the energy distribution very narrow the source works without any extraction inside the ionization zone. When gas is introduced into the source (dynamic mode) it has to pass a glass capillary plate before ionization (see Fig. 3.1). This ensures that only gas with a velocity in forward direction can pass into the source, whereas in static or residual gas mode, the gas velocity vectors inside the source are randomly distributed and therefore the sensitivity is a bit lower and the energy distribution slightly broader.

Important: There is no pressure gauge mounted inside the LEIS. When gas is introduced directly into the ionization zone, the actual pressure close to the microtip is unknown but vastly higher than the measured pressure at the chamber wall. Since the microtip must not be operated above  $1 \times 10^{-6}$  mbar pressure, the dynamic mode has to be previously cross-calibrated with the use of the measured signal in static mode at the same pressure. The signal in dynamic mode at a certain electron emission must not pass the maximum signal acquired in static mode at  $1 \times 10^{-6}$  mbar chamber pressure and the same electron current.

- The obtainable ion current has to reach several pA. Since at very low ion energies the angle of beam spread is expected to be quite large ( $65^\circ$ ; see chapter 5.4.3), this has to be compensated by a higher ion current. Moreover, a high intensity should also allow to enlarge the distance to the mass spectrometer entrance up to several 10 cm in order to find the optimal parameters for the RTOF and DFMS attraction grids to penetrate the  $\sim kT_e$  sheath discussed in chapter 2.3.
- To know better how the attraction grids of the two ROSINA mass spectrometers can influence the ion measurements, the ion source has been designed to generate a beam quite large in diameter i.e. larger

than the central structure in the RTOF attraction grid (meshed grid). Furthermore, a large beam also lowers space-charging effects compared to a narrow beam of the same intensity.

- For a useful ion mode calibration it is necessary to provide ROSINA DFMS and RTOF with a stable ion beam. In particular, the microtip emission needs to be constant over a time longer than the measurement modes of DFMS or RTOF, which require from a few minutes up to a few hours [PB94].

In addition, also the flow rate through the gas inlet (both, static and dynamic mode) has to be stable during the same period of time. This is done by a pressure reduction valve generating a stable pressure at the gas inlet.

- When the spacecraft orbits around the comet, the incident angle of the ions varies with respect to the ion optical axis of both mass spectrometers. Thus it is also important to test the angle dependency of the signal measured with both mass spectrometers. With e.g. the wide FOV of DFMS (see chapter 2.1.1 on page 4) ions of very different incident angles and energies are expected (compare the  $\pm 20^\circ$  of the DFMS wide FOV with the particle energy and angle distribution in Fig. 2.7 on page 15).

For this purpose a special setup has been arranged to mount the LEIS in front of the mass spectrometers: three moveable arms allow all relative positions and angles with respect to the ROSINA DFMS and RTOF source entrance axis (see chapter 5.6).

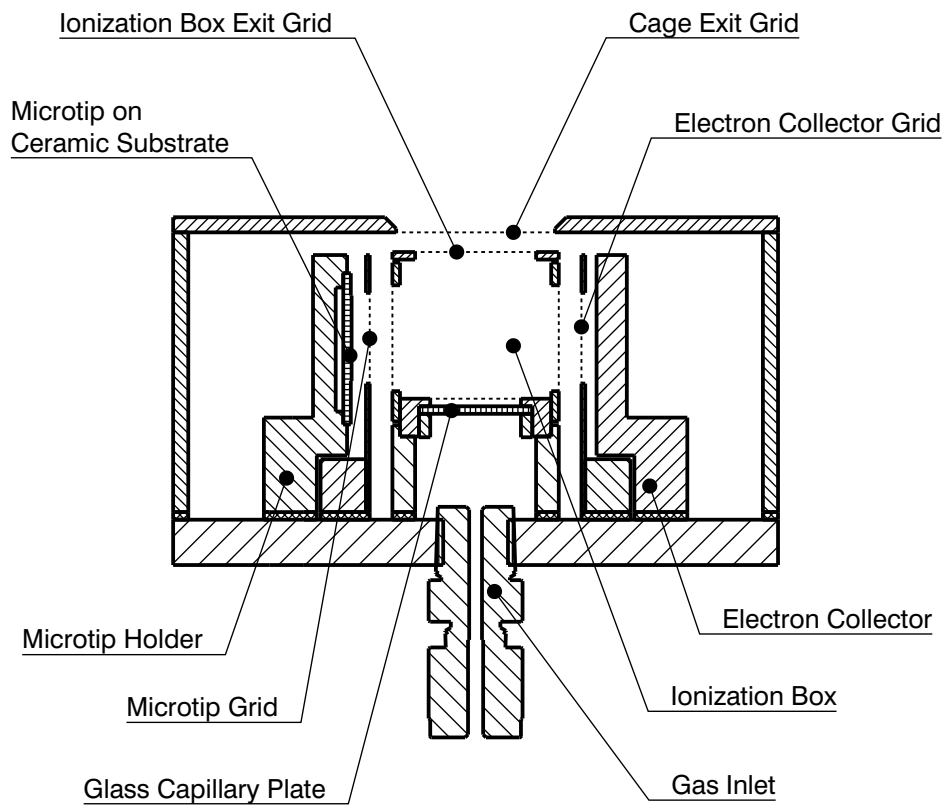
- At the comet both mass spectrometers are not only confronted with ions but also electrons. Therefore both mass spectrometers, DFMS and RTOF, are built to reject incoming electrons.

The LEIS also emits electrons: According to chapter 5.2 on page 58 a few percent of the electrons leave the source, probably due to collisions with grids and other parts within the source. There is no need to suppress these electrons with energies up to 75 eV, because they can be used to test if they have any influence on the mass spectrometers.

The final configuration of the source derived from this chapter will be presented in the following part.

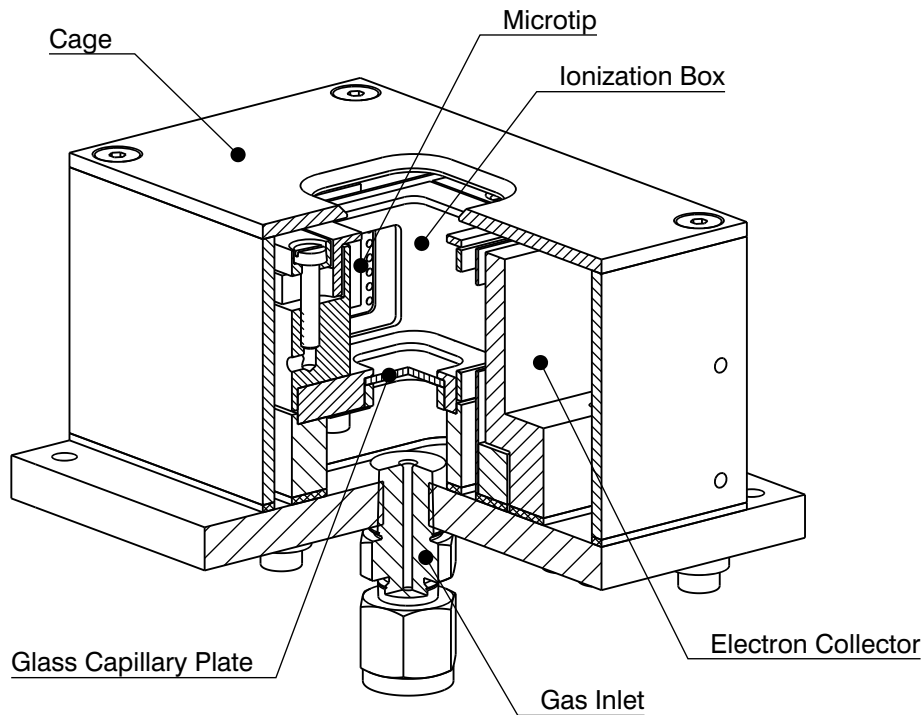
### 3.2 Source layout

Fig. 3.1 shows a cut through and Fig. 3.2 an isometric view of the LEIS. On the left side of the ionization box the Microtip can be seen, attached on a ceramic substrate. The glass capillary plate is mounted in front of the gas inlet and separates the region with higher pressure behind the plate from the ionization box.



**Fig. 3.1:** Cut through the Low Energy Ion Source. Scale 1:1.

All mechanical parts have been gold-plated in order to minimize effects like surface charging or oxidation of the surfaces. Fig. 3.3 shows the open Low



**Fig. 3.2:** Low Energy Ion Source isometric view.

Energy Ion Source without the outer cage. In this picture the microtip is placed on the right side. The nine white cables, which can be seen on the ceramic substrate, connect the eight microtip groups (microtip back) and the microtip front voltage (see chapter 3.2.3). The ionization box exit grid and its connection (metal wire mounted on the front side) to the baseplate feedthrough is visible as well.

### 3.2.1 *Electron flight path*

In nominal mode (see Tab. 3.2 on page 33) the 75 eV electrons, which are emitted by the microtip (microtip front 0 V), are accelerated towards the microtip grid (10 V) before they reach the Ionization zone (0 V). The majority

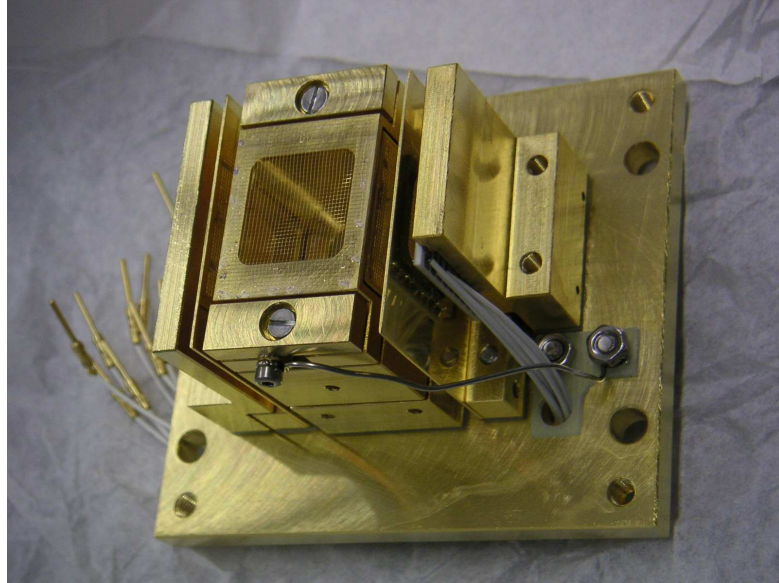


**Fig. 3.3:** Low Energy Ion Source without Cage.

of the electrons leave the ionization zone on the right side in Fig. 3.1, pass the electron collector grid, which is on the same potential as the microtip grid, and hit the electron collector (50 V), where the electron emission current is measured.

### 3.2.2 Neutral gas and ion flight path

Neutral gas which passed the glass capillary plate in dynamic mode (from below in Fig. 3.1) or has been introduced through the bypass (see Fig. B.4 on page 123) as well as the residual gas is ionized in the ionization box. The potential of the ionization box exit grid can be adjusted to extract the charged particles, but normally the ionization box, the ionization box exit grid as well as the cage exit grid are on the same potential to keep the whole ion flight path field-free. Thus whether an ion leaves the source or not is defined only by its flying direction after ionization (neglecting space charge effects and collisions in molecular flow). The cage exit aperture is roughly 21 mm  $\times$  21 mm.



### 3.2.3 Microtip

A microtip consists of micrometer sized metal spikes which emit electrons when applying a potential difference to a nearby grid.

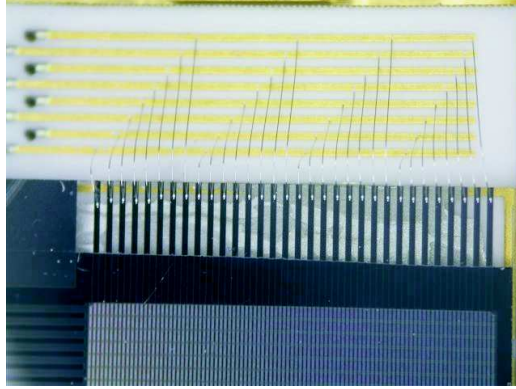


**Fig. 3.4:** Wire-bonding of the 8 groups. At the bottom the active area of the microtip can be seen.

Since the gate aperture between spike (cathode) and grid (anode) is between  $1.2 \mu\text{m}$  -  $1.4 \mu\text{m}$  and the voltage difference is in the order of several 10 V, the electric field strength rises close to 100 MV/m. Due to this large electric fields, metals can emit electrons according to Fowler-Nordheim [FN28]: the work function of typically 2 - 5 eV is substantially lowered so that the residual potential barrier can be tunnelled by numerous electrons. The current density  $j_e$  can be calculated using the following equation:

$$j_e(E) = K_1 \cdot \frac{E^2}{\Phi} \cdot e^{-\frac{K_2 \cdot \Phi^{\frac{3}{2}}}{|E|}}, \quad (3.1)$$

with

$E$ : electric field strength,

$K_1$  and  $K_2$ : soft field and material dependent parameters, and

$\Phi$ : work function of the spike material.

The microtip we use is a Spindt type [Mey66] LETI/CEA  $32 \times 32$  matrix molybdenum microtip that is arranged in 8 groups with 4 lines each (see Figs. 3.4 and 3.5). The dimension of the active area is roughly  $1.1 \text{ cm} \times 1.1 \text{ cm}$ . It is mounted on a gold printed ceramic plate already used for the ROSINA COPS [Roh01]. The connections from the microtip to the plate were made by the Hybrid SA in Switzerland with AlSi1  $25 \mu\text{m}$  strands on a KNS 8060 wire-bonder.

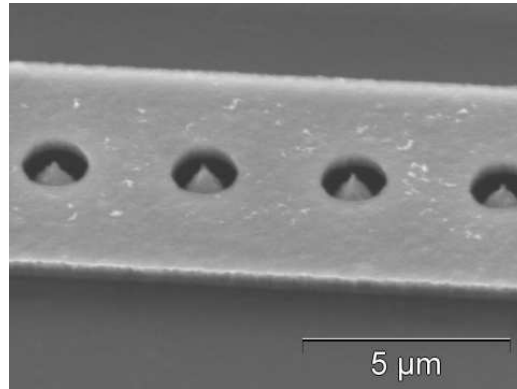


**Fig. 3.5:** Scanning electron microscope (SEM) image of a microtip line section.

#### 3.2.4 Glass capillary plate

The capillary plate consists of a two dimensional, regular array of glass tubes with an inner diameter of  $25 \mu\text{m}$ . These glass tubes are fused together, sliced, and integrated into a disc shape of  $1 \text{ mm}$  thickness. Each glass tube has excellent linearity as well as a hole diameter and tube length accuracy within  $\pm 1\%$ . The capillary plate with the characteristics listed in Tab. 3.1 has been chosen according to the calculations presented in chapter 4.

HAMAMATSU Capillary Plate J 5022-21	
Size $\varnothing$	87 mm
Thickness	1.0 mm
Channel diameter	25 $\mu\text{m}$
Center to center distance	32 $\mu\text{m}$

**Tab. 3.1:** Parameters of the used glass capillary plate

For the LEIS a piece of 1.4 cm  $\times$  1.4 cm (1.96 cm<sup>2</sup>) has been cut out from this plate.

### 3.2.5 Nominal potentials of the Low Energy Ion Source

Tab. 3.2 shows the nominal potentials for the LEIS. The cage exit defines the potential on the whole front surface of the source and is thus very important for the acceleration/deceleration of the ions once they have left the source. All other power supplies are floating on this potential. This allows to lift and lower the whole source without changing the relative potentials inside the source, the microtip extraction voltage in particular can be kept constant.

Electrode	Potential [V]	remark
Microtip holder	0...-75	floating
Microtip front	0...-75	floating
Microtip back	-75	floating
Microtip grid	10	floating
Ionization box	0	floating
Electron collector grid	10	floating
Electron collector	50	floating
Ionization box exit	0	floating
Cage exit	0... $\pm$ 20	

**Tab. 3.2:** Nominal potentials for the Low Energy Ion Source. The floating potentials are always related to the cage exit voltage which can be varied from  $-20\dots 20$  volts (see Fig. 3.1).

In general, microtip holder and microtip front are short-circuited outside of the vacuum chamber. The emission of the microtip is caused by the voltage

difference between the microtip back and the microtip front. Furthermore, the microtip back voltage defines the electron energy which is 75 eV during normal use. By changing the microtip front voltage, the emission of the microtip can be regulated without changing the electron energy. Once the microtip is conditioned (see chapter 5.1) the switch-on process should look as follows: Both, the microtip front and the microtip back voltage, should be lowered alternating to -75 V (with respect to the floating voltage) by turns of typically 20 V. When the microtip back voltage reaches -75 V the difference to the front voltage can be increased ( $\sim 5$  V/min) for the desired electron emission current.

Since both grids, the microtip grid and the electron collector grid, are normally on the same potential for symmetry purpose, they can be short-circuited, too. Finally, the ionization box and the ionization box exit can also be short-circuited to the cage exit, which leads to a uniform potential in the whole region accessible for the ions. For comparison, Fig. 6.3 on page 99 shows the potential energy view of the nominal source setup in the ion simulation program SIMION.

### 3.3 *Standards for the used electronics*

During the testing phase, the LEIS is powered by laboratory electronics. There are specific requirements in order not to interfere with ions at these low energies: the used power supplies should be stable (regulated) and their connections to the source need to be well shielded.

The potential difference of the cage exit and the ion collecting element (i.e. RTOF orthogonal source) defines the ion energy. Thus the whole power supplies have to be floatable with respect to the cage exit potential.

There is currently a custom-built electronics package in development in order to merge all the used power supplies as well as the ammeters. Furthermore, a computer interface is planned for monitoring and operation. The circuit diagrams can be found in Figs. B.7 and B.8 on page 126 and following.

## 4. THEORY

After fixing the principal setup, the Low Energy Ion Source key parameters can be derived theoretically for further comparison with the measured results in chapter 5. The main goal will be to calculate the ion current which is generated by the ion source as a function of the parameters which can be adjusted by the operator: the microtip extraction voltage, which is responsible for the electron current, the gas inlet valve, which is used to rise the pressure in the whole vacuum chamber (static mode) or mainly inside the source only (dynamic mode), and the source floating voltage (cage exit), which is responsible<sup>1</sup> for the effective ion energy.

This chapter is divided into three parts. In dynamic mode, the glass capillary array plays a central role. The first part of this chapter is thus devoted to the conductance of the capillary plate. Second, the estimated ion current range is calculated and space-charging effects are studied. Finally, the third part covers the expected equilibrium pressure in the vacuum chamber while pumping and introducing gas through the source inlet.

Surface contamination and depletion, electronic noise, and influences on the beam outside of the source may also affect the performance of the ion source. Nevertheless, these effects are skipped in this theoretical part of the work, since only the measurements can show us their importance.

---

<sup>1</sup>more precisely its difference to the collecting element (MCP, ion collector, attraction grid, etc.)

### 4.1 The glass capillary array

This section treats the gas flow through the capillary plate. An adequate plate has been chosen (see Tab. 3.1 on page 33) and its parameters will already be used for the calculations in this section.

The channel diameter to length ratio ( $d/l$ ) of the capillary plate is given by

$$d/l = 1/40. \quad (4.1)$$

The maximum possible incident angle for a gas atom or molecule in order to pass a single channel without hitting the surface:

$$\alpha = \arctan(d/l) = 1.43^\circ. \quad (4.2)$$

The flow through one capillary is calculated and then multiplied by the number of channels in order to attain the conductivity of the whole array. This value is used afterwards to calculate the ion current generated by the source.

#### 4.1.1 The gas flow

Dushman and Lafferty [DL66, chapter 2] divide the gas flow in three parts that are specified by a dimensionless parameter called the Knudsen number  $K_n$ . This number is defined by the ratio of the mean free path of a molecule to the characteristic dimension of the system: let  $f$  be the mean free path evaluated at the average pressure in the channel, and let  $d$  be the characteristic dimension, e.g. the diameter in the case of a cylindrical tube:

Where  $f/d < 0.01$ , the flow is viscous.

Where  $f/d > 1.00$ , the flow is molecular.

Where  $0.01 < f/d < 1.00$ , the flow is in the transition regime.

The Knudsen number can be calculated in the following way:

$$K_n = \frac{f}{d} = \frac{\frac{V/N}{\sqrt{2} \cdot \sigma}}{d} = \frac{k \cdot T}{\sqrt{2} \cdot \pi \cdot \delta^2 \cdot p \cdot d}, \quad (4.3)$$

using

$f$ : mean free path,

$d = 25 \mu\text{m}$ : characteristic dimension (tube diameter),

$V$ : volume,

$N$ : number of molecules,

$\sigma$ : collision cross section,

$k = 1.38 \times 10^{-23} \text{ J/K}$ : Boltzmann constant,

$T = 300 \text{ K}$ : temperature,

$\delta = 3 \times 10^{-8} \text{ cm}$ : typical molecule radius, and

$p$ : pressure.

#### 4.1.1.1 Prerequisites for molecular flow

At low pressures, the mean free path is large to the characteristic dimension and the flow of gas is limited by molecular collisions with the walls of the channel. Since there are very few interactions between the molecules, each of them acts independently [DL66, p. 80].

Given the parameters of the capillary plate (listed in Tab. 3.1 on page 33) one can calculate the upper limit of the pressure for molecular flow, using Eq. 4.3. In this region  $K_n$  must exceed 1.00:

$$p \leq \frac{k \cdot T}{\sqrt{2} \cdot \pi \cdot \delta^2 \cdot d \cdot K_n} . \quad (4.4)$$

Due to the small characteristic dimension ( $25 \mu\text{m}$  tube diameter) the maximum pressure is quite high:

$$p \leq 4.14 \text{ mbar} .$$

Since the LEIS will be operated in a much lower pressure range, namely below  $1 \times 10^{-6} \text{ mbar}$ , it is sufficient to calculate the conductivity for the molecular flow region only.

#### 4.1.1.2 Number of holes in the plate

The conductivity of the capillary plate can be approximated by the conductivity of a single tube which is multiplied by the number of tubes in the plate. The number of channels can be computed with the known parameters of the plate, listed in Tab. 3.1 page 33.

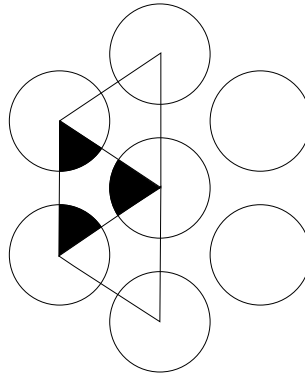


**Fig. 4.1:** Hexagonal configuration of the glass capillary array

The area of one triangle in Fig. 4.1 is equal to

$$F_{\text{Triangle}} = \frac{1}{2} \cdot c^2 \cdot \sin\left(\frac{\pi}{3}\right) , \quad (4.5)$$

using

$c=32 \mu\text{m}$ : center to center distance.

The area of holes in such a triangle (black colored area in Fig. 4.1) is equal to half the area of a single hole:

$$F_{\text{Hole area in Triangle}} = \frac{1}{2} \cdot F_{\text{Hole}} = \frac{1}{2} \cdot a^2 \cdot \pi , \quad (4.6)$$

using

$a=12.5 \mu\text{m}$ : channel radius.



The whole active area of the glass capillary array is a square with the following dimensions (see chapter 3.2.4):

$$F_{\text{Active}} = 1.4 \text{ mm} \times 1.4 \text{ mm} = 1.96 \text{ mm}^2 \quad . \quad (4.7)$$

The open area ratio and the number of holes in the glass capillary array can now be computed with the use of Eqs. 4.5, 4.6, and 4.7:

$$R_{\text{Open area}} = \frac{F_{\text{Hole area in Triangle}}}{F_{\text{Triangle}}} \approx 55\% \quad \text{and} \quad (4.8)$$

$$N_{\text{Holes}} = \frac{R_{\text{Open area}} \cdot F_{\text{Active}}}{a^2 \cdot \pi} \approx 221'000 \quad . \quad (4.9)$$

#### 4.1.1.3 Gas flow through the capillary plate

The capillary plate consists of  $N_{\text{Holes}} \approx 221'000$  parallel tubes. The relation between the flow rate through one of these tubes  $Q_{\text{Single Tube}}$  and through the whole capillary plate  $Q_{\text{Total}}$  can be described as follows:

$$Q_{\text{Total}} = N_{\text{Holes}} \cdot Q_{\text{Single Tube}} \quad . \quad (4.10)$$

The molecular flow rate through a small<sup>1</sup> tube between two vessels A and B is given by [DL66]

$$Q_{\text{Single Tube}} = p \cdot \frac{dV}{dt} = k \cdot T \cdot \frac{dN}{dt} \quad , \quad (4.11)$$

---

<sup>1</sup>(a) small in dimension compared to the mean free path and (b) small in area compared to the area of the vessels

with  $\frac{dN}{dt}$  being the difference in the number of particles moving from vessel  $A \rightarrow B$  and from  $B \rightarrow A$ :

$$\frac{dN}{dt} = \frac{dN}{dt}(A \rightarrow B) - \frac{dN}{dt}(B \rightarrow A) = \frac{1}{4} \cdot v_a \cdot F_T \cdot K \cdot (n_A - n_B) . \quad (4.12)$$

For an ideal gas using:

$$p \cdot V = N \cdot k \cdot T , \quad (4.13)$$

the molecular flow rate through on single tube  $Q_{\text{Single Tube}}$  is

$$Q_{\text{Single Tube}} = \frac{1}{4} \cdot v_a \cdot F_T \cdot K \cdot (p_A - p_B) , \quad (4.14)$$

with

$F_T = 490 \mu\text{m}^2$ : cross section of one tube,

$K = \frac{8}{3} \cdot \frac{a}{l} = 3.33 \times 10^{-2}$ : the factor  $K$  may be regarded as ratio between the rate at which gas leaves the outlet of the tube and the rate at which gas strikes the inlet,

$n_A, n_B, p_A, \text{ and } p_B$ : molecule densities and pressures in both vessels, and

$v_a = \sqrt{\frac{8 \cdot k \cdot T}{\pi \cdot m}}$ : mean molecular speed e.g. 476 m/s for  $\text{N}_2$  ( $m = 28$  amu) at a temperature of 300 K.

Fig. 4.2 shows the total flow rate calculated with Eq. 4.10 as a function of the pressure behind the capillary plate  $p_A$  and the residual gas pressure in the vacuum chamber  $p_B = 5 \times 10^{-8}$  mbar.

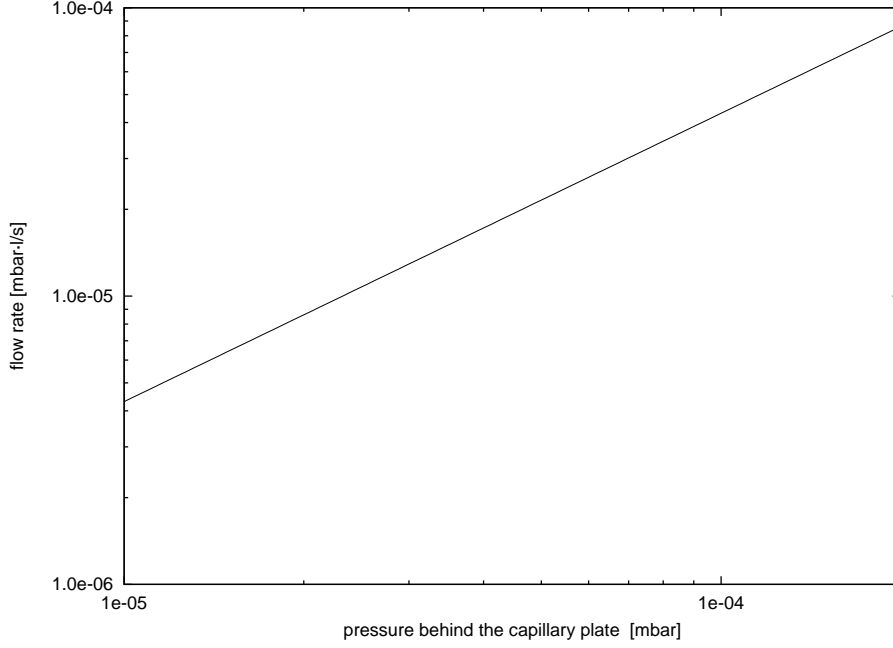


**Fig. 4.2:** Flow rate  $Q_{\text{Total}} = N_{\text{Holes}} \cdot Q_{\text{Single Tube}}$  through all orifices plotted against the pressure behind the plate  $p_A$  ( $\text{N}_2$  molecules, residual gas pressure set to  $p_B = 5 \times 10^{-8}$  mbar).

With Eq. 4.10 and Eq. 4.14 it is possible to calculate the number of molecules passing through the whole plate per time:

$$\frac{dN}{dt} = \frac{N_{\text{Holes}} \cdot Q_{\text{Single Tube}}}{k \cdot T} = \frac{Q_{\text{Total}}}{k \cdot T} . \quad (4.15)$$

Considering all the molecules passing uniformly through the active area of the plate with a mean velocity of  $v_a$  the density and with Eq. 4.13 the pressure of the molecules inside the ion source can be calculated:

$$n_{\text{Source}} = \frac{Q_{\text{Total}}}{F_{\text{Active}} \cdot v_a} \quad \text{and} \quad (4.16)$$

$$p = n_{\text{Source}} \cdot k \cdot T . \quad (4.17)$$

In Fig. 4.3 the additional pressure inside the source, caused by the neutral gas passing through the capillary plate (Eq. 4.17), is plotted versus  $p_A$ , the pressure behind the plate. For the total pressure inside the source the residual pressure ( $p_B = 5 \times 10^{-8}$  mbar) needs to be added to the plotted value. For instance at a pressure behind the capillary plate of  $p_A = 1 \times 10^{-5}$  mbar, the ratio of residual pressure to introduced gas inside the source is 1:1. On the other hand, raising the pressure close to  $p_A = 2 \times 10^{-4}$  mbar behind the capillary plate leads to a ratio of 1 : 20.

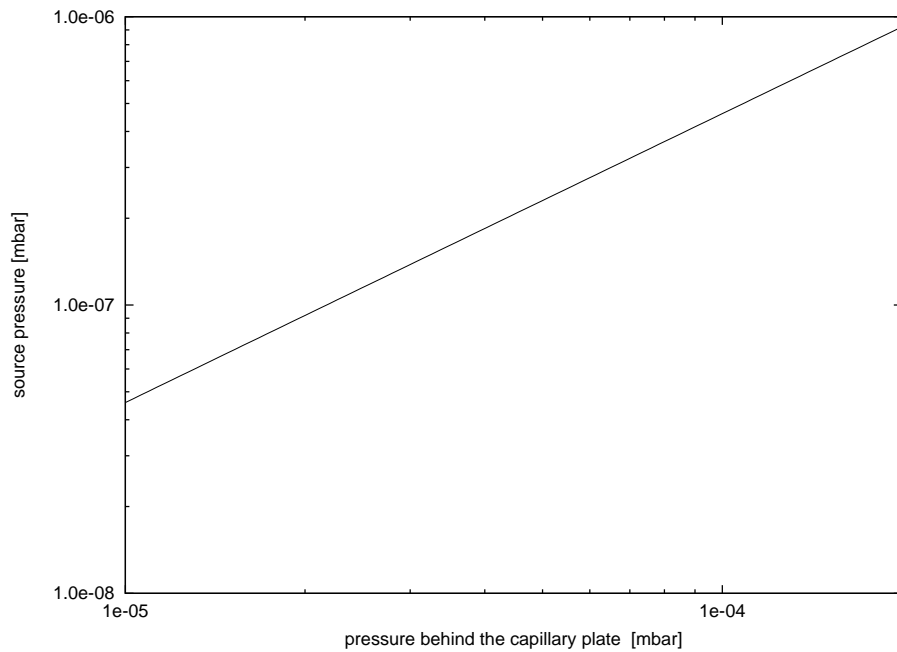


**Fig. 4.3:** Pressure of introduced gas inside the ionization volume of the Low Energy Ion Source versus the pressure  $p_A$  behind the capillary plate ( $N_2$  molecules). For the total pressure the residual gas pressure  $p_B = 5 \times 10^{-8}$  mbar needs to be added.

## 4.2 Ionizing the neutral gas beam in the source

The ion source uses an electron impact method to generate ions from the neutrals. The integrated electron source is a microtip array with a cold emission of electrons.

The electron impact ionization process requires the transfer of sufficient excitation energy from an electron to an atom or a molecule so that the particle is ionized. Dissociative processes are not treated in this section.

The use of a cold electron emission method, in contrast to a hot filament, grants that the molecules will not be heated up lest they broaden the energy distribution additionally.

### 4.2.1 The ion current

The current of ions  $i_+$  of a single species can be calculated [WB73, pp. 13–23] the following way (plotted in Fig. 4.4):

$$i_+ = \beta \cdot \sigma \cdot n \cdot l \cdot i_- , \quad (4.18)$$

using

$\beta$ : correction factor ( $0 \leq \beta \leq 1$ ) including grid transmissions etc.,

$\sigma$ : cross section for electron impact ionization e.g.  $2.508 \text{ \AA}^2$  for 70 eV electrons on  $\text{N}_2$  molecules,

$n$ : molecule density,

$l = 1.4 \text{ cm}$ : ionization path of the electrons, and

$i_-$ : electron current emitted by the microtip array.

Furthermore, it is possible to compute the ratio between ionized molecules and the number of all molecules:

$$R_{\text{Ionization}} = \frac{\frac{i_+}{q}}{\frac{Q_{\text{Total}}}{k \cdot T}} , \quad (4.19)$$

whereby

$q = 1.602 \times 10^{-19}$  C: elementary charge.

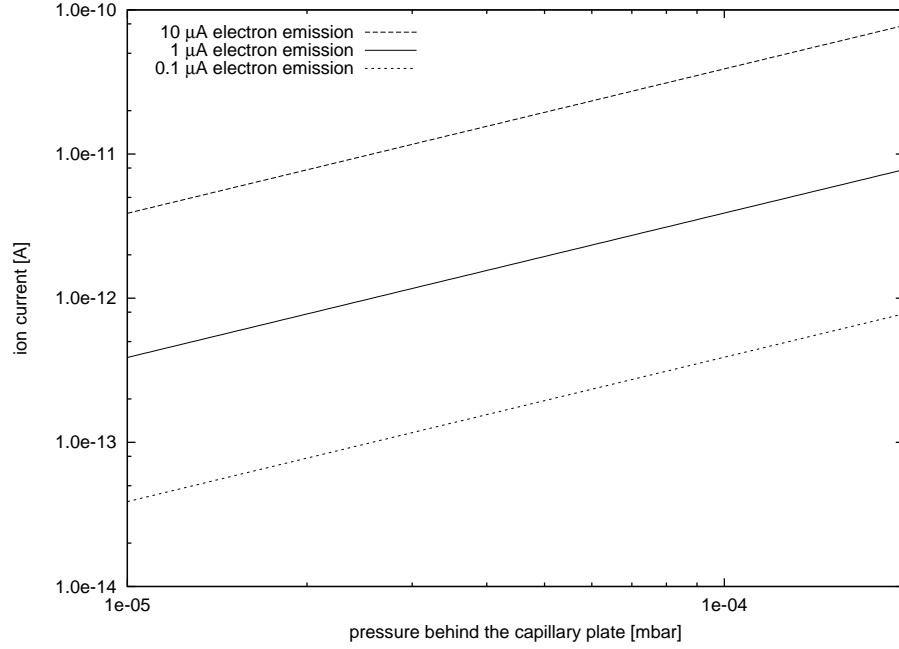


**Fig. 4.4:** Ion current dependent of pressure behind capillary plate and electron emission current ( $\text{N}_2$  molecules, residual gas pressure  $p_B = 5 \times 10^{-8}$  mbar).  $\beta$  has been set to 1.

The mean path for ionization of the electrons  $\gamma$  can be calculated the following:

$$\gamma = \frac{1}{\sigma \cdot n} = \frac{k \cdot T}{\sigma \cdot p}, \quad (4.20)$$

using

$\sigma$ : cross section for electron impact ionization e.g.  $2.508 \text{ \AA}^2$  for 70 eV electrons on  $\text{N}_2$  molecules,

$n$ : number density of molecules,

$T$ : temperature, and

$p$ : gas pressure.

The collision frequency  $f_{\text{Collision}}$  then calculates:

$$f_{\text{Collision}} = \frac{v_e}{\gamma} , \quad (4.21)$$

with

$v_e$ : mean electron velocity e.g. 4960 km/s for 70 eV electrons.

For instance, at  $T = 300$  K,  $p = 1 \times 10^{-6}$  mbar, and  $\sigma = 2.508 \text{ \AA}^2$  the mean free path of the electrons is  $\gamma = 1.657$  km and the collision frequency is  $f_{\text{Collision}} = 3$  kHz.

#### 4.2.2 Space-charge effects

At pressures below  $1 \times 10^{-5}$  mbar the mean free paths of electrons and ions much longer than the characteristic system dimensions. Although collisions are rare, there are ion-ion, electron-ion, and electron-electron interactions caused by their electrical charge. In this chapter the maximum allowed ion current is calculated and the corresponding maximum charges per volume ratio to prevent space-charge effects.

The charges within an ion or electron beam creates an electric field. This force is predominantly transverse (outward) and disperses these charges in the plane perpendicular to the beam axis, i.e., it will cause the beam to expand in diameter. The charge to volume ratio of ions  $C_+$  can be calculated with the use of Eqs. 4.7, 4.16, and 4.19:

$$C_+ = \frac{i_+}{F \cdot v_a} , \quad (4.22)$$

using

$q = 1.602 \times 10^{-19}$  C: elementary charge,

$v_a = \sqrt{\frac{8 \cdot k \cdot T}{\pi \cdot m}}$ : mean molecular speed, and

$F = 4.41 \text{ cm}^2$ : profile of the beam i.e. aperture of the cage exit grid.

The same formula holds true for the electrons:

$$C_- = \frac{\frac{i_-}{q}}{F_{\text{Microtip}} \cdot v_e} , \quad (4.23)$$

where

$q = 1.602 \times 10^{-19}$  C: elementary charge,

$F_{\text{Microtip}} = 1.21 \text{ cm}^2$ : active area of the microtip, and

$v_e$ : mean electron velocity e.g. 4960 km/s for 70 eV electrons.

Wilson and Brewer [WB73, pp. 132–143] give an upper limit for the current above which space-charge effects can be the dominant influence on a cylindrical beam shape. This equation is for an ion mass of 30 amu and valid for one species of charged particles:

$$i_{\text{max}} = 0.35 \times 10^{-7} \cdot \frac{V^{\frac{3}{2}}}{\left(\frac{L}{r_o}\right)^2} , \quad (4.24)$$

with

$i_{\text{max}}$ : ion current maximum to avoid space charge effects ( $i_+ \leq i_{\text{max}}$ ),

$V$ : beam energy in units of volts,

$L$ : beam length, and

$r_o$ : initial beam radius.

For example, the current of an ion beam of roughly 0.7 cm in radius and 1 cm long (normally the source is mounted close to the detecting element) at 200 V should be below 50  $\mu\text{A}$  in order to avoid space-charge effects. Or, for a 4 V ion beam of the same dimensions which is typical for the LEIS, the current limit  $i_{\text{max}}$  is around 140 nA. Together with Eq. 4.22 the maximum allowed number of charges per volume is typically  $C_+ < 4000 \text{ mm}^{-3}$  for this 4 V  $\text{N}_2$  beam. Although the low energy ion beam is not cylindrical one has an approximation for the upper limit  $i_{\text{max}}$  for the ion current  $i_+$  to prevent these negative effects. Fig. 4.4 shows that the source ion current output is lower than the calculated upper limits above. Thus there are no major space-charging effects expected with the LEIS.



### 4.3 The vacuum system

Since the whole ion source is integrated in a vacuum chamber, the pressure inside depends on the vacuum pumping system, the residual gas, and the gas flow through the capillary plate (namely the gas inlet valve and the flow rate through the capillary plate, see chapter 4.1.1.3).

The gas flow  $Q_{\text{tot}}$  through the capillary plate rises the pressure in the chamber. The final pressure depends on the pumping efficiency, which depends on the ion species and the used pumps. To simplify matters the calculations are made for  $\text{N}_2$  molecules and a pumping efficiency of 250 l/s and 1000 l/s. The resulting pressure in the chamber  $p_{\text{Target}}$  when introducing gas will thus be equal to

$$p_{\text{Target}} = \frac{Q_{\text{Total}}}{P} + p_{\text{Residual}} \quad , \quad (4.25)$$

using

$P$ : pumping capacity i.e. 250 l/s or 1000 l/s and

$p_{\text{Residual}}$ : residual pressure with closed valve after a long period of time; still set to a typical value of  $p_{\text{B}} = 5 \times 10^{-8}$  mbar.

Eq. 4.25 is plotted in Fig. 4.5 for two different pumping capacities  $P = 250$  l/s and  $P = 1000$  l/s. The pumping efficiency of a certain species or the type of the pump itself has large influence on the equilibrium pressure when introducing gas through the source into the vacuum chamber. Especially with a high pumping capacity, the pressure inside the vacuum chamber rises much slower than the pressure inside the source (compare Fig.4.3 with Fig. 4.5).

The gas inlet system has an additional resistance. The gas inlet valve (see Fig. B.4 on page 123) and the back side of the glass capillary array are connected by a tube with a length of around 10 cm and a diameter of 4 mm plus a thin tube of about 1 m length and a diameter of 0.5 mm.

Oatley [Oat57] calculated the flow rate through a system of two tubes under the following conditions

- the rate of the flow of gas through a single tube must be proportional to the pressure difference between the ends
- the conductivity of a tube must be independent of the components to which its ends are connected

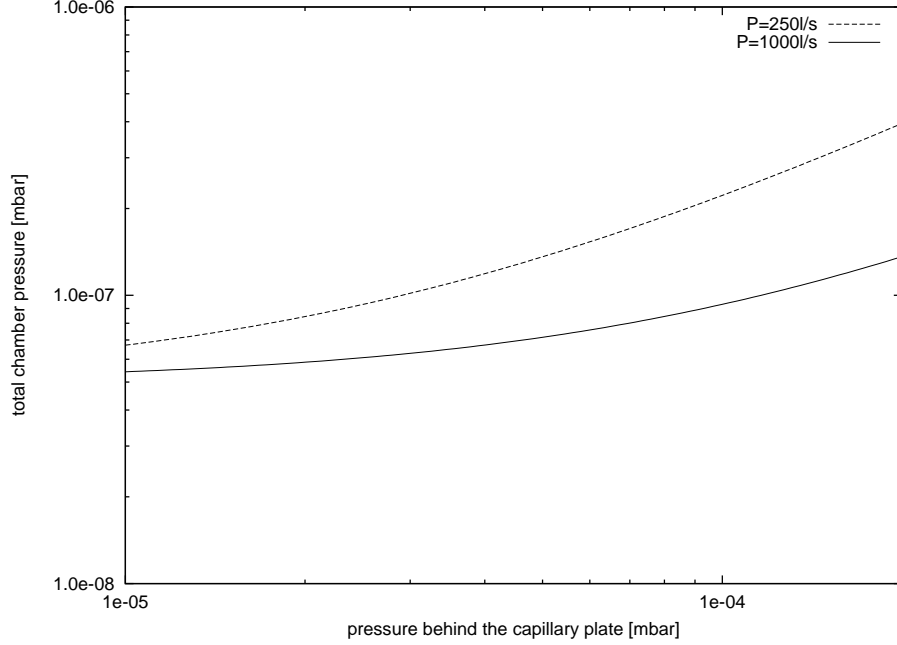


**Fig. 4.5:** Total chamber pressure versus pressure behind capillary plate ( $N_2$  molecules, residual gas pressure  $p_B = 5 \times 10^{-8}$  mbar). Pumping capacity  $P = 250$  l/s and  $P = 1000$  l/s.

The flow can be computed equally to 4.14 but with a correction to  $K = \frac{8}{3} \cdot \frac{a}{l}$ . The new  $K$  depends on the pumping direction and can be calculated the following way:

$$\frac{1}{K_{12}} = \frac{1}{K_1} + \frac{1}{g \cdot K_2} + \frac{1}{g}, \quad (4.26)$$

using

$K_{12}$ : the new  $K$  factor for the whole system of two tubes,

$K_1$ :  $K$  factor of the first tube,

$K_2$ :  $K$  factor of the second tube, and

$g = \frac{F_{T2}}{F_{T1}}$ : the ratio between the cross sections of the tubes.

The direction of the gas flow is from tube 1 to tube 2. Applied on the ion source, tube 1 corresponds to the shorter one of 10 cm length and tube 2 to the one with a length of  $\sim 1$  m. Thus  $K_{12}$  is  $6.665 \times 10^{-4}$  and the conductivity  $L = 1.557 \times 10^{-5}$  l/s for the LEIS. Therefore the pressure behind the capillary plate and the gas inlet is different due to the low conductance of the thin and long tubes connecting both parts.

#### 4.4 *Summary from theoretical considerations*

The ion current generated by the LEIS is highly variable. By changing the microtip electron emission and by varying the pressure inside the source, the ion current can reach up to several 10 pA (see Fig. 4.4). Despite the low energy of the beam no space-charge effects are expected, especially due to the large diameter of the ion source (see chapter 4.2.2).

Important: The gas inlet is the most delicate part of the LEIS. It is easily possible to raise the pressure close to the microtip above  $1 \times 10^{-6}$  mbar (see Fig. 4.3). But, in order not to damage the emission surface, the microtip should not be used above this pressure (see chapter 5.1.2). The operator has to be aware that in dynamic mode the pressure inside the source is higher than the pressure reading at the gauge mounted inside the wall of the vacuum chamber (compare Fig. 4.3 to Fig. 4.5).



## 5. CHARACTERIZATION OF THE LOW ENERGY ION SOURCE

### 5.1 *Microtip conditioning*

During the formation period the surface state of the microtip is changing to reach its optimum in intensity and stability [PB94] as far as the emission is concerned. This effect of surface reshaping is not fully understood yet, but has already been observed [Con98]. Degassing of the microtip, even after backing out, plays an important role in the seasoning phase (see Fig. 5.1). Gas, which is trapped during the production process in the (sub-)micrometer structures, is released gradually with the applied extraction voltage. No official procedure exists for the used microtip, but following steps are proven and tested.

#### 5.1.1 *Required conditions*

The tip to grid resistance of each line should be around 20 M $\Omega$ . Once this is checked, the microtip can be installed in the vacuum chamber. The used setup can be seen in Fig. 5.2. It typically consists of a microtip holder and a collector anode about 1 cm in front of the microtip.

Before applying voltages we proceed with following steps:

- A vacuum in the  $10^{-9}$  mbar region is strongly recommended. For that purpose the microtip should be baked out at 150° Celsius for at least 24 hours.
- Used power supplies should not produce any voltage or power spikes.
- The electron emission current should be collected and measured on an anode with at least 20 volts with respect to the microtip front.

- Some monitor values are needed for the microtip formation:
  - The extraction voltage  $U_{\text{eff}}$ , which is defined by the difference of the microtip front and the microtip back voltage and which should not exceed 75 V.
  - The emitted current  $i_-$ , which is measured on the collector anode.
  - The microtip current  $i_{\text{em}}$ , defined as the current through the microtip.

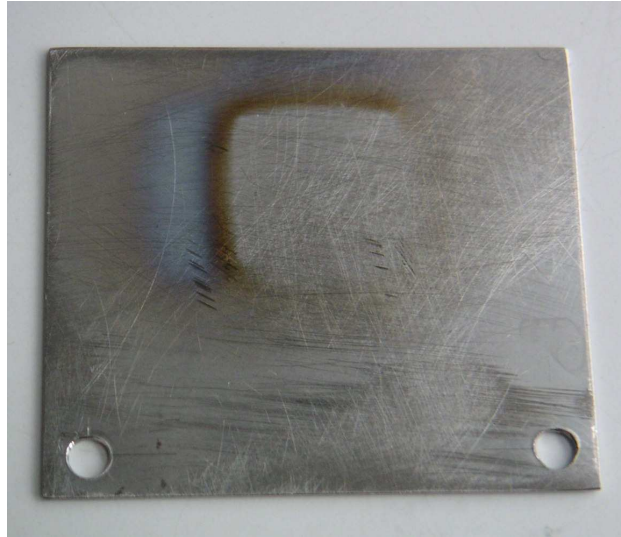


**Fig. 5.1:** Collector anode after microtip seasoning phase. The silhouette of the active area is visible (electron polished area) in the center, the blue area left to it comes from degassing of the soldering, and the brown part is caused by the microtip degassing. Degassing of the bonding wires (Fig. 3.4) would take place on the right side of the active area, but has not been observed on the collector anode.

### 5.1.2 Formation procedure

The conditioning procedure includes several steps and some of them need to be repeated for each of the eight groups individually. Generally, the microtip seasoning is very time-consuming and can last several days. During each

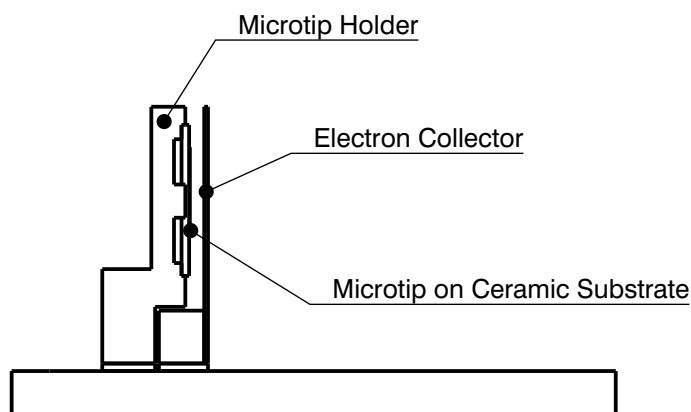


**Fig. 5.2:** Microtip conditioning setup.

step (typically +5 volts in extraction voltage  $U_{\text{eff}}$ ) it is recommended to wait until the emitted current  $i_-$  and the microtip current (current through the microtip)  $i_{\text{em}}$  are stable. During the first few steps, before the microtip emits electrons (extraction voltage  $U_{\text{eff}}$  typically below 30 volts), a stable microtip current is quickly achieved. Afterwards, in the upper regions of the extraction voltage ( $U_{\text{eff}}$  close to 75 volts), up to one day is needed per group and step.

1. The first step is to connect all eight groups together and step up to an extraction voltage of 30 volts in order to see the general behavior of the microtip array<sup>1</sup>. Recommended steps are typically 5 volts in 10 minutes.
2. Once at 30 volts the microtip should run in this mode for several hours.
3. Afterwards step down voltage (around 5 V/min)

---

<sup>1</sup>The used microtip for the LEIS actually showed problems here. It turned out to have no advantage to use two neighbouring groups since the emission of electrons is nearly the same as for just one group. Thus this part of conditioning has been done twice, once using groups 1, 3, 5, and 7 and once 2, 4, 6, and 8.

4. Then each group should be treated individually. The rest of the lines are connected to the front of the microtip and therefore have 0 volts extraction potential. The extraction voltage of the one group is stepped up by 5 volts in typically 10 minutes below 30 volts and 1 hour above 30 volts until first emission occurs (45 – 50 volts).
5. Once again the microtip should run in this mode for a few hours.
6. Above emission threshold each step of 5 volts takes several hours up to one day until the emission current  $i_-$  and the current through the microtip  $i_{em}$  are stable.
7. Once the group provides a stable emission at 75 volts, step down the extraction voltage (around 1 minute per step), change group, and restart with step 4, until all groups are done.

Finally, it is recommended to repeat the conditioning from step 4 but using all groups or a set of groups together (i.e. 1, 3, 5, and 7 or 2, 4, 6, and 8).

After the formation period the microtip should not be operated above  $1 \times 10^{-6}$  mbar.



### 5.1.3 Conditioning results for the Low Energy Ion Source microtip

Tabs. 5.1 and 5.2 show typical values for the LEIS microtip after conditioning. Values may vary fairly, especially for the microtip current  $i_{\text{em}}$ . These values can be used to monitor the microtip in the assembled ion source since the electron emission current  $i_-$ , obtained during the microtip conditioning, cannot be directly compared with the measured current in the assembled ion source, because of the different setup used for microtip conditioning (compare Fig. 3.1 on page 28 with the assembly in Fig. 5.2 on page 53).

We encountered two different problems with the microtip. One problem is the needed settle time after changing the extraction voltage  $U_{\text{eff}}$ . Especially after the microtip has been inactive for several days, it needs some time to stabilize. In such a case we turned on the microtip typically one day in advance of the use, according to the seasoning in chapter 5.1.2.

On the other hand, we detected a strong influence of neighbouring groups on each other. Especially when using all eight groups together, there is almost no additional emission current compared to the use of only four non-neighbouring groups (e.g. 1, 3, 5, and 7). Thus we decided to use groups 2, 4, 6, and 8 for standard ion source operation and keep groups 1, 3, 5, and 7 as backup. Both problems are not very well understood yet, but they are critical neither.

In general, the microtip must be handled with care. Especially after a longer period of inactivity the stepping up of the extraction voltage  $U_{\text{eff}}$  should be done slowly and cautiously. Furthermore, it is strongly recommended not to use the microtip above  $1 \times 10^{-6}$  mbar pressure in order to prevent arcing. Finally, the microtip should be stored under vacuum while not in use to protect the surface from contamination and from mechanical damage.

$U_{\text{eff}}$ [V]	Microtip current $i_{\text{em}}$ [ $\mu\text{A}$ ] through group(s)													
									1, 3, 5, & 7		2, 4, 6, & 8		all groups	
	1	2	3	4	5	6	7	8	sum	eff	sum	eff	sum	eff
0	0.5	0.6	0.4	0.5	0.5	0.4	0.5	0.4	1.9	1.1	1.9	1.5	3.8	0.2
5	16.9	20.7	16.2	20.7	16.2	19.5	18.2	15.0	67.5	62.5	75.9	82.2	143.4	10.7
10	34.0	41.5	32.5	41.8	31.9	39.0	36.4	30.4	134.8	127.7	152.7	166.5	287.5	26.2
15	51.1	62.4	48.9	63.1	48.5	58.9	55.0	45.9	203.5	192.8	230.3	252.2	433.8	45.1
20	68.3	84.0	65.6	84.8	64.7	79.5	73.4	61.8	272.0	259.3	310.1	340.9	582.1	67.2
25	85.4	106.0	82.6	107.1	81.7	99.8	92.7	78.2	342.4	328.9	391.1	430.0	733.5	91.9
30	103.6	128.5	99.8	130.1	98.6	121.5	112.4	95.2	414.4	399.5	475.3	522.0	889.7	119.3
35	121.6	151.5	117.7	153.6	116.5	143.4	132.5	112.5	488.3	472.0	561.0	616.0	1049.3	149.3
40	139.9	174.9	135.7	177.9	134.7	166.4	153.0	130.5	563.3	548.0	649.7	714.0	1213.0	182.0
45	159.0	199.5	154.7	203.2	153.9	190.0	174.2	149.4	641.8	626.0	742.1	817.0	1383.9	218.4
50	179.3	225.5	174.9	230.1	173.6	215.6	197.3	169.6	725.1	707.0	840.8	926.0	1565.9	259.9
55	200.7	253.4	196.6	259.4	195.6	243.4	221.9	192.2	814.8	796.0	948.4	1041.0	1763.2	308.1
60	224.3	284.0	220.5	291.2	219.6	274.4	248.8	217.4	913.2	890.0	1067.0	1171.0	1980.2	365.0
65	250.3	318.4	247.5	327.8	246.0	310.2	278.6	245.6	1022.4	995.0	1202.0	1312.0	2224.4	432.0
70	280.0	357.4	277.6	368.8	277.1	352.2	311.7	279.7	1146.4	1114.0	1358.1	1485.0	2504.5	518.0
75	314.9	408.3	314.0	420.0	313.7	404.6	352.6	321.2	1295.2	1262.0	1554.1	1704.0	2849.3	634.0

**Tab. 5.1:** Microtip current  $i_{\text{em}}$  of single and combined groups. The 'sum' column indicates the summation of the corresponding groups in single operation and can be compared to the effective measured value in the 'eff' column.

$U_{\text{eff}}$ [V]	Microtip emission current $i_-$ [ $\mu\text{A}$ ] from group(s)													
									1, 3, 5, & 7		2, 4, 6, & 8		all groups	
	1	2	3	4	5	6	7	8	sum	eff	sum	eff	sum	eff
0	0.00	0.00	0.00	0.00	0.00	0.00	0.00	0.00	0.00	0.00	0.00	0.00	0.00	0.00
5	0.00	0.00	0.00	0.00	0.00	0.00	0.00	0.00	0.00	0.00	0.00	0.00	0.00	0.00
10	0.00	0.00	0.00	0.00	0.00	0.00	0.00	0.00	0.00	0.00	0.00	0.00	0.00	0.00
15	0.00	0.00	0.00	0.00	0.00	0.00	0.00	0.00	0.00	0.00	0.00	0.00	0.00	0.00
20	0.00	0.00	0.00	0.00	0.00	0.00	0.00	0.00	0.00	0.00	0.00	0.00	0.00	0.00
25	0.00	0.00	0.00	0.00	0.00	0.00	0.00	0.00	0.00	0.00	0.00	0.00	0.00	0.00
30	0.00	0.00	0.00	0.00	0.00	0.00	0.00	0.00	0.00	0.00	0.00	0.00	0.00	0.00
35	0.00	0.00	0.00	-0.01	-0.01	-0.01	-0.01	-0.01	-0.02	-0.01	-0.03	-0.02	-0.05	-0.01
40	-0.07	-0.09	-0.08	-0.08	-0.08	-0.11	-0.09	-0.11	-0.32	-0.14	-0.39	-0.20	-0.71	-0.18
45	-0.38	-0.51	-0.42	-0.43	-0.39	-0.52	-0.42	-0.53	-1.61	-0.71	-1.99	-1.12	-3.60	-1.03
50	-1.18	-1.60	-1.31	-1.52	-1.19	-1.73	-1.34	-1.67	-5.02	-2.38	-6.25	-3.94	-11.54	-3.68
55	-2.86	-3.84	-3.08	-3.78	-2.92	-4.06	-3.12	-3.95	-11.98	-5.71	-15.63	-8.66	-27.61	-8.82
60	-5.54	-7.39	-6.01	-7.48	-5.57	-8.06	-5.96	-7.69	-22.99	-11.06	-30.62	-16.97	-53.61	-17.98
65	-9.32	-12.69	-10.02	-13.16	-9.12	-14.41	-9.92	-16.14	-38.38	-18.77	-56.40	-29.77	-94.78	-31.21
70	-15.21	-20.72	-15.25	-20.96	-14.76	-22.87	-15.60	-21.11	-60.82	-29.44	-85.60	-48.45	-146.48	-52.51
75	-23.81	-33.01	-23.24	-33.93	-22.85	-37.26	-23.40	-33.28	-93.30	-46.52	-137.48	-80.01	-230.78	-87.04

**Tab. 5.2:** Microtip emission current  $i_-$  of single and combined groups. The 'sum' column indicates the summation of the corresponding groups in single operation and can be compared to the effective measured value in the 'eff' column.

## 5.2 Grid transmissions

After the microtip seasoning phase, the LEIS has been assembled according to Fig. 3.1 on page 28. The electron current  $i_-$  generated by the microtip not only hits the gas and the collector anode but also all other components (especially grids) of the ion source. It is possible to measure all these currents on the individual elements to gain an overview of the electron transmissions of each grid in this specific ion source setup.

The geometric transmission of the used Buckbee Mears grids is  $88 \pm 1\%$ , but since the electrons can also hit the grid holding structure and other electrodes, the effective transmission of the used parts is lower.

Electrode	Potential [V]	Transmission	Fraction of total current	Current [ $\mu$ A]
Microtip holder	0			0.00
Microtip grid	10	73.2%	26.8%	-25.50
Ionization box	0	57.8%/76.1%	30.9%	-29.40
Electron collector grid	10	69.5%	10.3%	-9.80
Electron collector	50		<b>23.4%</b>	-22.32
Ionization box exit	0	58.6%	3.6%	-3.40
Cage exit	0	43.6%	2.9%	-2.72
ext. Collector anode	0		<b>2.2%</b>	-2.10
Total emission			100%	-95.24

**Tab. 5.3:** Transmissions and collected electron currents (75 eV electron energy) of the individual ion source parts and an external collector anode in front of the source. Since the ionization box consists of two grids the first value in the "Transmission" column represents the overall transmission and the second value its square root as an estimation of the transmission per grid.

Tab. 5.3 lists those collected currents of the individual ion source parts. First of all we see that roughly 2% of all electrons leave the ion source and reach the external collector anode. Since this current is larger than the overall current from positive ions (order of  $10^{-6}$  see chapter 5.3) an extra electron suppression grid is needed in front of the source for the following intensity,

beam shape, and energy distribution measurements<sup>1</sup>.

Furthermore, the measured current on the electron collector is only around 25% of the effective electron current emitted by the microtip (see Tab. 5.2 on page 57). The rest is picked up by other parts of the ion source.

The lower transmission values for the ionization box exit and the cage exit implies that some of the corresponding electrons hit these grids in a non-perpendicular angle: Fig. 3.1 on page 28 shows that those grids are placed in parallel to the general electron flight path from the microtip to the collector (see chapter 3.2.1). If we use the external collector anode as a retarding potential analyzer we see that the potential must be larger than the electron energy of 75 eV in order to significantly suppress these electrons. So a considerable portion of them leave the source perpendicular to the cage exit and to the ionization box exit grids (or parallel to the ions). This can't be explained geometrically nor is it a function of electric fields since the inner part of the source is on the same potential (see column "Potential" in Tab. 5.3). Surface impacts and rejections might explain this effect.

---

<sup>1</sup>This extra grid is not necessary for measurements with the ROSINA instruments DFMS & RTOF. Both instruments are capable to operate in plasma environment.

### 5.3 Sensitivity and intensity

The sensitivity of the LEIS has been obtained with the setup shown in Fig. B.1 on page 120. The potential between the ion collector anode and the ion source is 200 V in order to reflect the electrons and accelerate the ions. The measurements have been performed mainly with argon in order to avoid additional effects such as the dissociation of molecules. Additionally, this chapter also includes the comparison between static and dynamic mode sensitivity.

Starting from Eq. 4.18 on page 43 for a single ideal gas the sensitivity  $S$  is defined as following:

$$\frac{i_+}{i_-} = \underbrace{\frac{\beta \cdot \sigma \cdot l}{k \cdot T}}_S \cdot p \quad , \quad (5.1)$$

whereby

$i_+$ : current of argon ions,

$i_-$ : electron current emitted by the microtip array,

$\beta$ : correction factor ( $0 \leq \beta \leq 1$ ) including e.g. grids and the source geometry,

$\sigma = 2.972 \text{ \AA}^2$ : argon cross section for 75 eV electron impact ionization [SRL<sup>+</sup>95],

$k = 1.38 \times 10^{-23} \text{ J/K}$ : Boltzmann constant,

$T = 293 \text{ K}$ : temperature, and

$l = 1.6 \text{ cm}$ : ionization path of the electrons.

A simplified model for the calculation of the correction factor  $\beta_{\text{static}}$  in static mode consists of two grids in the flight path of the ions with 88% transmission each (cage exit grid and ionization box exit grid). Furthermore, the source geometry can be reduced to a cube with only the front face open ( $\frac{1}{6}$  of the surface):

$$\beta_{\text{theoretical}} = \frac{1}{6} \cdot (0.88)^2 \quad . \quad (5.2)$$

With Eqs. 5.2 and 5.1 the calculated sensitivity  $S_{\text{calculated}}$  is  $1.51 \text{ mbar}^{-1}$ .

### 5.3.1 Static mode sensitivity

In static mode argon has been introduced through the bypass (see Fig. B.4 on page 123). The partial argon pressure, measured with a Granville-Phillips gauge and corrected for argon, is assumed to be uniform in the whole vacuum chamber and especially inside the source.

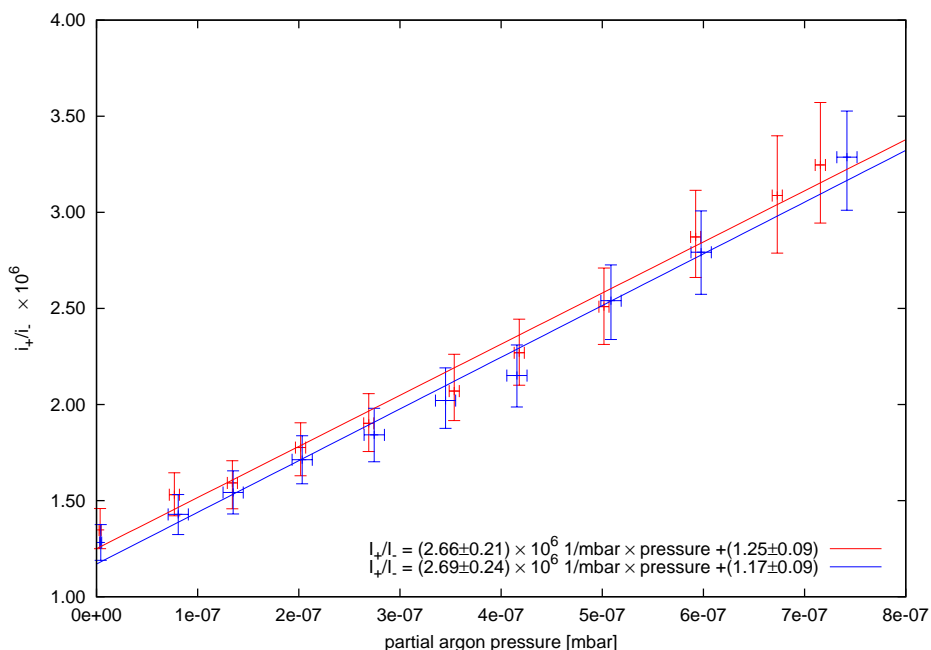


**Fig. 5.3:** Two sets of sensitivity measurements in static mode. Plotted is the ion current per electron current dependent of the partial argon pressure measured at the chamber wall. The residual gas pressure is  $2.87 \times 10^{-8}$  mbar and the ion energy was set to  $U_{\text{ion}} = 200$  eV. The blue curve (lower curve) was measured approximately one hour after the red curve. The indicated error for the slope and the offset of the fit give the 95% confidence interval.

In Fig. 5.3 the collected ion current is plotted versus the partial argon pressure in the vacuum chamber. The measured sensitivity  $S_{\text{static}} \approx 2.7 \text{ mbar}^{-1}$  is almost double the value of the theoretical calculated value ( $S_{\text{calculated}} \approx 1.5 \text{ mbar}^{-1}$ ). This is mainly due to the correction factor  $\beta_{\text{static}}$ , which is more complex than estimated in Eq. 5.2 ( $\beta_{\text{static}} > \beta_{\text{theoretical}}$ ): the 200 V ion acceleration potential slightly penetrates the cage exit grid [RBBW98] and attracts some extra ions. Both curves in Fig. 5.3 show off-

sets. This can be caused on one hand by a higher pressure inside the source compared to outside at the chamber wall where the pressure is measured. Degassing of the microtip (see Fig. 3.4 on page 31) or some other pollution close to the source are possible. On the other hand, the used picoamperemeter is operated at its lower limit (typically below 5 pA) and it is therefore sensitive to noise coming e.g. from the close-by railway station, even through shielded cables. Especially, when looking at the noise of the single measurements (see the large errorbars in Figs. 5.3, 5.4, and 5.5) an electrical problem cannot be excluded. Furthermore, the lower curve has been obtained about one hour after the red one, so the effect could be time dependent even though the error for the offset is just in the same order ( $\pm 0.09$ ).

### 5.3.2 Maximum current

The maximum ion current reached in static mode of the source was  $\approx 33$  pA at a chamber pressure of  $1 \times 10^{-6}$  mbar and a measured electron emission current  $i_- \approx 8.5 \mu\text{A}$ . This value for maximum intensity can change quite a bit. The microtip needs some time to settle down for a stable emission. Furthermore, the measured ion current depends also on the offset which changes with time as described above.

Every time when the source is mounted in a different chamber it is important to gather the maximum ion current at a chamber pressure of  $1 \times 10^{-6}$  mbar in static measurement mode. From that moment, this value should never be exceeded in order not to damage the microtip. This applies in particular to the dynamic mode, where the gas is introduced directly into the source. In this case the actual pressure close to the microtip can only be guessed since there is no pressure gauge inside the source. But as long as the measured current in dynamic mode does not exceed the maximum current obtained in static mode ( $1 \times 10^{-6}$  mbar chamber pressure) at the same electron emission, one can be sure that the pressure close to the microtip is also below  $1 \times 10^{-6}$  mbar.

An even higher ion current could only be achieved by stepping up the microtip extraction voltage beyond 75 V. But this has never been done with this microtip before and may be risky. Since both ROSINA mass spectrometers RTOF and DFMS are purpose-built for requiring only some  $10^3$  ions for a distinct signal, it seems also needless to further increase the intensity<sup>1</sup>.

---

<sup>1</sup>the plasma density at the comet is typically below several  $10^5 \text{ cm}^{-3}$  and reaches down to only a few ions per  $\text{cm}^{-3}$  ( Tab. 2.2 on page 22). A low density needs to be compensated by a longer accumulation time.



### 5.3.3 Dynamic mode sensitivity

In dynamic mode the bypass is closed and the argon has been introduced through the source. The pressure is still measured at the wall of the vacuum chamber and therefore is lower than the actual pressure in the source (see Fig. 5.5).

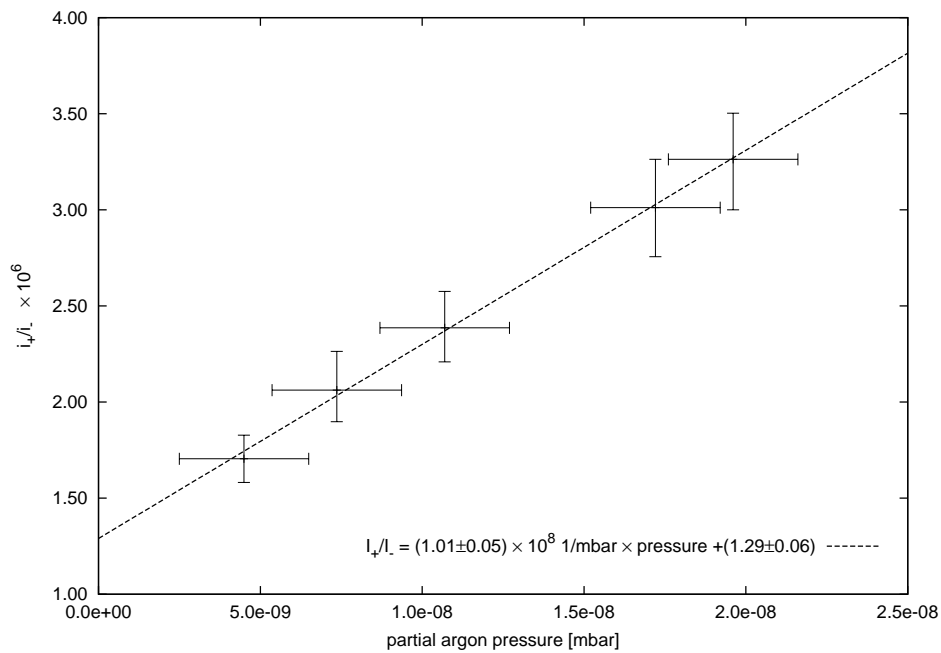


**Fig. 5.4:** Sensitivity measurement in dynamic mode. Plotted is the ion current per electron current dependent of the partial argon pressure measured at the chamber wall. The residual gas pressure is  $2.87 \times 10^{-8}$  mbar and the ion energy was set to  $U_{\text{ion}} = 200$  eV. The indicated errors for the slope and the offset of the fit give the 95% confidence interval.

Fig. 5.4 shows the measured sensitivity in dynamic mode. Even though the errorbars are quite large, the measured points do nicely fit a straight line. The measured sensitivity  $S_{\text{dynamic}} \approx 1.0 \times 10^2 \text{ mbar}^{-1}$  is a bit misleading, since the current is related to the pressure measured at the chamber wall and not to the real (unknown) pressure inside the ion source. Nonetheless, the measured offset is of the same order as for the static mode.

The results from the static and dynamic sensitivity measurements can be combined via the measured ion current in order to calculate the effective pressure inside the ionization volume as a function of the pressure reading at the chamber wall. This can be seen in Fig. 5.5. When gas is introduced directly into the source, the real pressure inside is about forty times higher than the one measured outside the source. This value differs from chamber to chamber but is very important. Furthermore, instruments mounted in front of the LEIS can also be influenced by the higher local pressure.

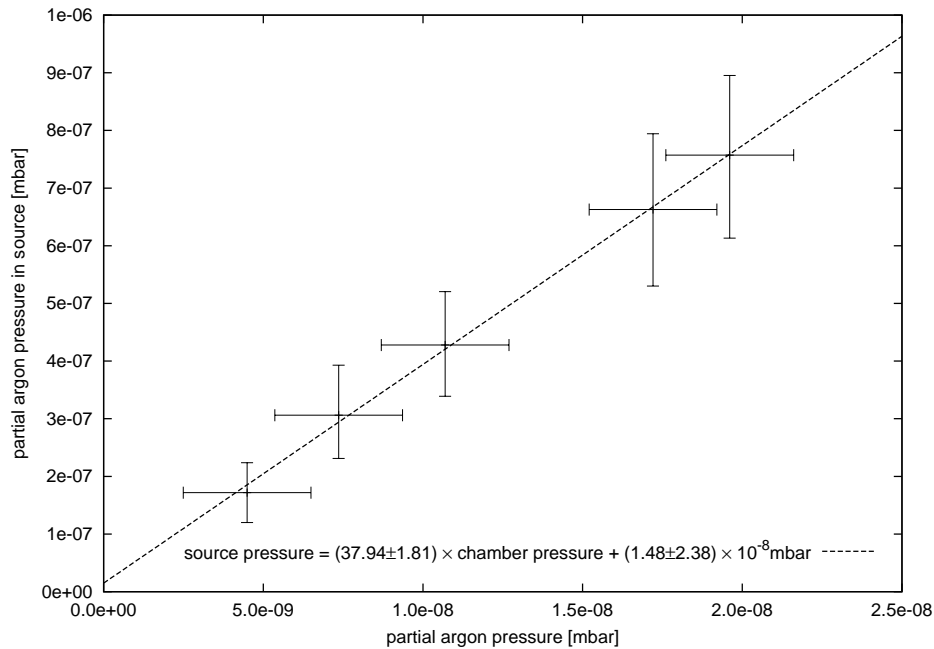


**Fig. 5.5:** Relation between partial argon pressure in the source and pressure reading at the chamber wall. When gas is introduced into the ion source the pressure inside the ionization zone is higher by approximately a factor of forty than the one outside at the wall of the chamber. The residual gas pressure is  $2.87 \times 10^{-8}$  mbar and the ion energy was set to 200 eV. The indicated errors for the slope and the offset of the fit give the 95% confidence interval.

The offset of the linear fit in Fig. 5.5 implies a small origin of gas inside the source. As already mentioned this could be caused by the microtip degassing or the gas inlet valve not being perfectly vacuum sealed. But the offset is

small enough ( $1.48 \times 10^{-8}$  mbar) compared to the 95% confidence interval ( $\pm 2.38 \times 10^{-8}$  mbar) that it is not (statistically) significant.

#### 5.4 *Beam shape measurements*

The beam shape of the LEIS has been measured with a series 3300 MCP/RAE [Qua91a] position sensitive detector from Quantar Technology. It consists of a resistive anode (charge-division) position encoder (RAE), five wafer type, microchannel-plate electron multipliers (MCPs), and integral anode bias and signal decoupling circuits. This device must be operated in clean vacuum with pressures lower than  $1 \times 10^{-6}$  mbar.

Signal processing and spatial position decoding of the four low-level output signals from this sensor is provided by the Quantar Technology 2401 Series Position Analyzer [Qua91b] in combination with the Option EP preamp, data collection, and display systems.

The detector has been placed roughly 1 cm in front of the LEIS as shown in Fig. B.2 on page 121. The potential between detector and source has been varied from at least 100 volts, in order to suppress the 75 eV electrons, up to 400 volts for a better ion detection efficiency.

The LEIS can produce an ion beam far too intense for this type of position sensitive detector. We therefore tested several grids in front of the detector in order to dampen the signal. Unfortunately, these grids had a large influence on the effective beam shape and thus we limited the electron emission current to several nA. Only in chapter 5.4.4 we used an array of three grids in order to show that the beam profile at higher intensities is not influenced by space charging. Therefore we expect the measured beam shapes from this chapter to be typical over the whole intensity range.

### 5.4.1 Static mode beam shape

In the static mode the source inlet valve has been closed and no gas was introduced directly into the ion source. The electron emission current  $i_-$  of the microtip has been varied from 1 nA to 7 nA and the ion energy has been set to 200 eV. This first set of beam profiles has been taken in order to show the influence of rising intensity on the beam shape. All shapes are normalized to the total ion current at 7 nA electron emission in Fig. 5.8 on page 70.

Counts on screen [1/100s]	Fraction of counts	$i_-$ [nA]	Fraction of current	Figure Nr.
122110 ± 349	15.8%	1.0 ± 0.2	14.3%	5.6
222020 ± 471	28.8%	2.0 ± 0.2	28.6%	A.1
334208 ± 578	43.3%	3.0 ± 0.2	42.9%	5.7
441320 ± 664	57.2%	4.0 ± 0.2	57.1%	A.2
545077 ± 738	70.6%	5.0 ± 0.2	71.4%	A.3
661072 ± 813	85.6%	6.0 ± 0.2	85.7%	A.4
772167 ± 879	100.0%	7.0 ± 0.2	100.0%	5.8

**Tab. 5.4:** Characteristics for the measured beam shapes for different electron emission currents  $i_-$  in static mode at  $4.4 \times 10^{-8}$  mbar residual gas pressure. The accumulation time is 100 s and the ion energy is 200 eV.

Tab. 5.4 lists the measured intensities of all 7 acquired profiles and shows how the intensity evolves with the rise of the electron emission current (third column). In the first column the total measured counts during 100 s on the MCP detector are listed, as well as the corresponding Poisson's statistics. The second column lists the fraction of the actual measured intensity relative to the 7 nA electron emission current case (last row). The fourth column gives the corresponding values predicted from the relative fraction of the electron emission current. Some of the beam shapes can be found in appendix A.

It has already been mentioned that the emission current has to be limited to several nA in order to not supersaturate the position sensitive detector. Thus the microtip must be operated very close to the lower limit value of the emission which is quite delicate.

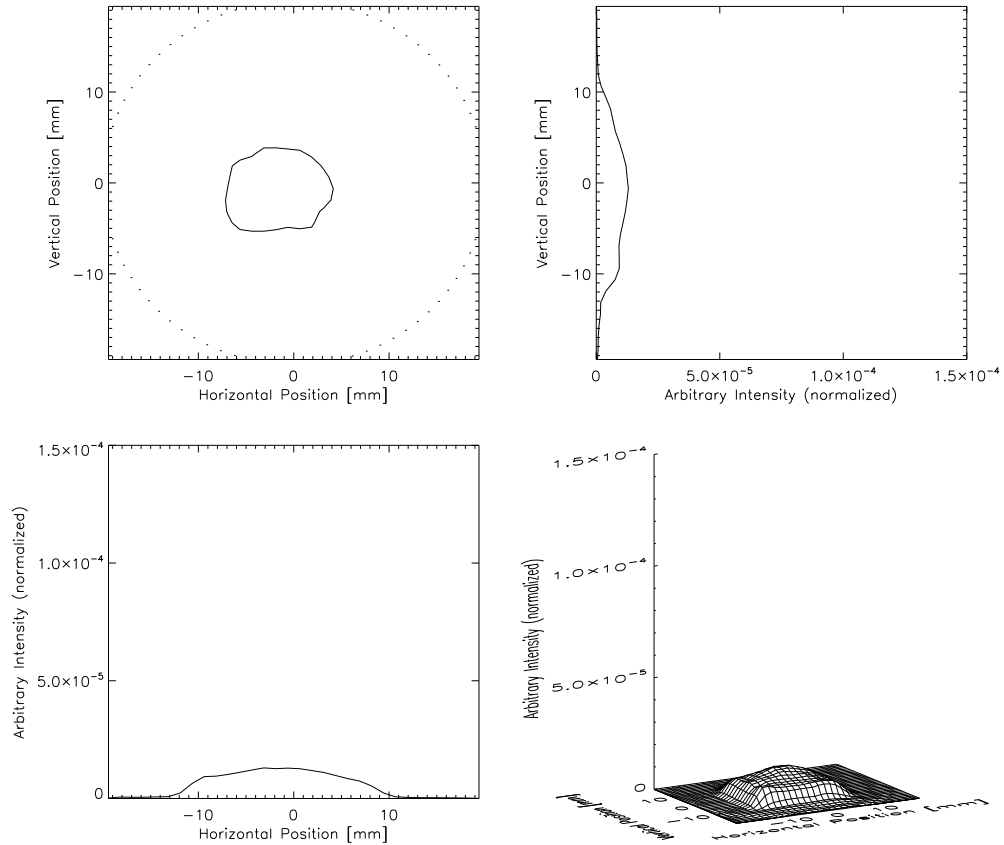


**Fig. 5.6:** Beam shape at 1.0 nA electron emission current  $i_-$  in static mode at  $4.4 \times 10^{-8}$  mbar residual gas pressure. The plots are normalized to the intensity of the beam at 7.0 nA electron emission current in Fig. 5.8 on page 70. Top left the plot shows the  $1 \times 10^{-5}$  contour lines and top right a vertical cut through peak maximum is shown. Bottom left a horizontal cut through the peak maximum can be seen and bottom right the beam intensity is plotted as a 3D-surface.

We do not know how uniform the electrons are emitted close to the emission threshold. It is possible that only some hot-spots are actually generating this emission current. Fortunately, the measured beam shapes do not indicate that this might be a major effect.

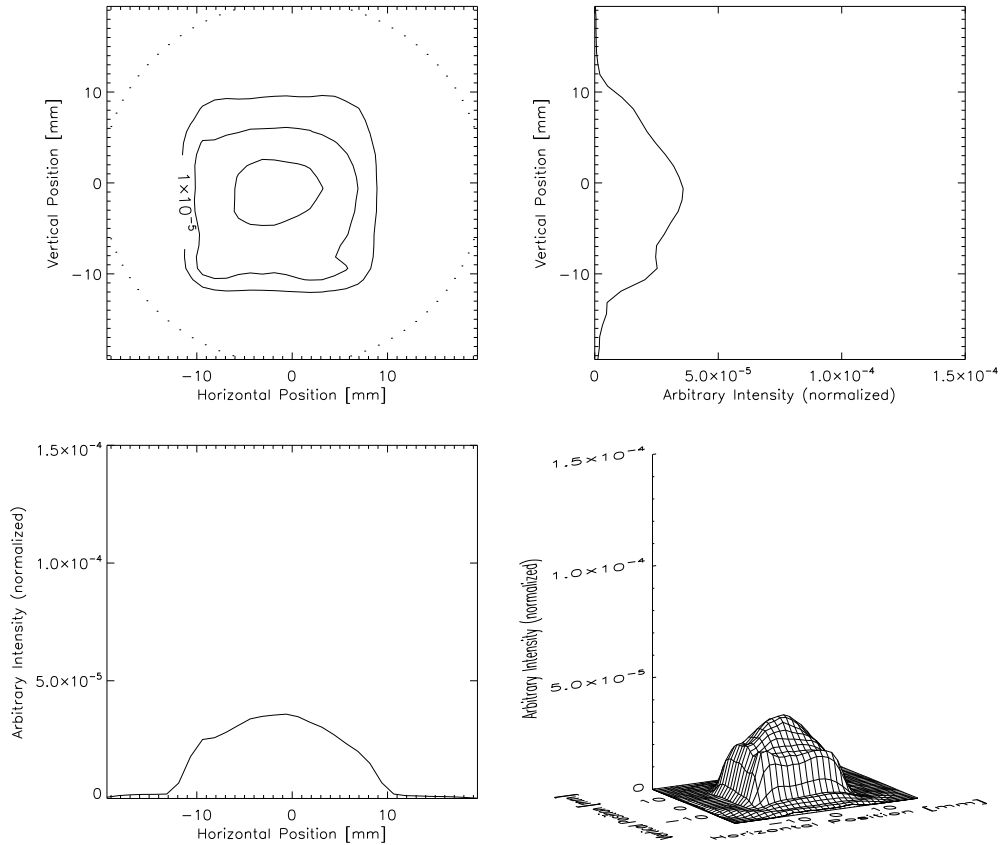


**Fig. 5.7:** Beam shape at 3.0 nA electron emission current  $i_-$  in static mode at  $4.4 \times 10^{-8}$  mbar residual gas pressure. The plots are normalized to the intensity of the beam at 7.0 nA electron emission current in Fig. 5.8 on page 70. Top left the plot shows the  $1 \times 10^{-5}$  contour lines and top right a vertical cut through peak maximum is shown. Bottom left a horizontal cut through the peak maximum can be seen and bottom right the beam intensity is plotted as a 3D-surface.

The measured current varies about  $\pm 0.2$  nA which explains the difference between the fraction of counts and the fraction of electron emission current in Tab. 5.4, especially in case of the 1.0 nA emission.

Generally, the quadratic beam shape at the bottom is caused by the physical

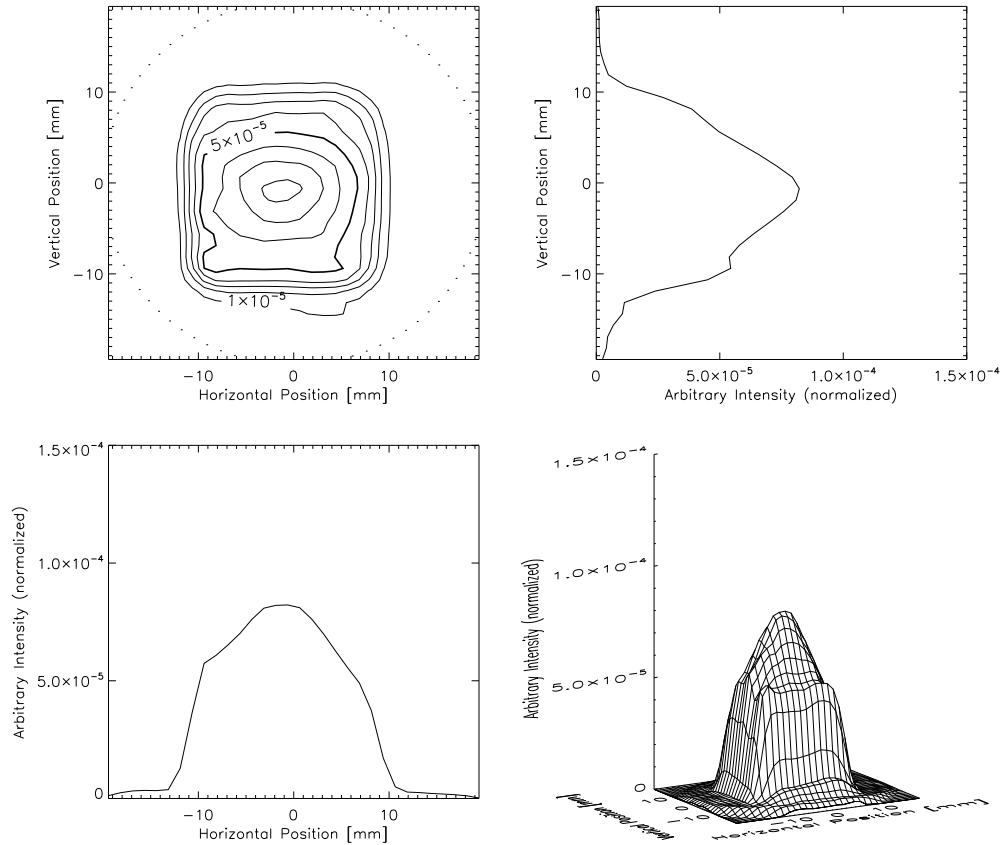


**Fig. 5.8:** Beam shape at 7.0 nA electron emission current  $i_-$  in static mode at  $4.4 \times 10^{-8}$  mbar residual gas pressure. Top left the plot shows the  $1 \times 10^{-5}$  contour lines and top right a vertical cut through peak maximum is shown. Bottom left a horizontal cut through the peak maximum can be seen and bottom right the beam intensity is plotted as a 3D-surface.

dimensions of the cage exit grid ( $21 \text{ mm} \times 21 \text{ mm}$ ; see Fig. 3.1 on page 28). In contrast, the circular top is caused by the fact that the center of the source gets the greatest portion of ions generated anywhere inside the ion source. This effect is even more pronounced in the dynamical mode presented in chapter 5.4.2 on page 71.



Since the LEIS has not a perfectly symmetrical inner setup, this is also reflected in the profile of the beam: the upper side (positive vertical position) faces the microtip side (microtip front; potential typically 0 V) whereas the lower part (negative vertical position) points towards the electron collector (potential typically 50 V, strong repeller for low energy ions). In general, the flank of the electron collector side is a bit steeper. In contrast to this, the left and right side (horizontal position) show no general difference.

#### 5.4.2 Dynamic mode beam shape

When the bypass is closed and the gas is introduced directly into the source, the beam shapes look different. In dynamic mode the pressure inside the source is significantly higher than on the edge of the vacuum chamber where the pressure gauge is mounted. It is only possible to calculate the effective pressure inside the source by the use of the equation in Fig. 5.5 on page 64. The initial flying direction of the introduced neutral atoms (argon) before ionization is not randomly distributed but directional from the glass capillary array towards the source exit.

Counts on Screen [1/100s]	Fraction of counts	$i_-$ [nA]	Fraction of current	Figure Nr.
$261948 \pm 512$	33.7%	$1.0 \pm 0.2$	33.3%	5.9
$532425 \pm 730$	68.5%	$2.0 \pm 0.2$	66.7%	5.10
$777352 \pm 882$	100.0%	$3.0 \pm 0.2$	100.0%	5.11

**Tab. 5.5:** Characteristics for the measured beam shapes for different electron emission currents  $i_-$  in dynamic mode at  $4.4 \times 10^{-8}$  mbar residual gas pressure and  $3.6 \times 10^{-7}$  mbar argon in the source introduced through the glass capillary array. The ion energy is still 200 eV and the accumulation time is 100 s.

Tab. 5.5 gives the applied settings for the three beam shapes acquired in dynamic mode. The individual columns represent the same values as in Tab. 5.4. Due to the higher pressure compared to the static mode measurements it wasn't possible to rise the electron emission current  $i_-$  above 3.0 nA in order to not supersaturate the position sensitive detector.

Figs. 5.9, 5.10, and 5.11 show the acquired beam shapes at  $i_- = 1.0$  nA, 2.0 nA, and 3.0 nA, respectively. The ion energy for all pictures is 200 eV in order to get a sufficient signal on the MCP detector. It has already been mentioned that the profiles look different compared to the static mode. Namely

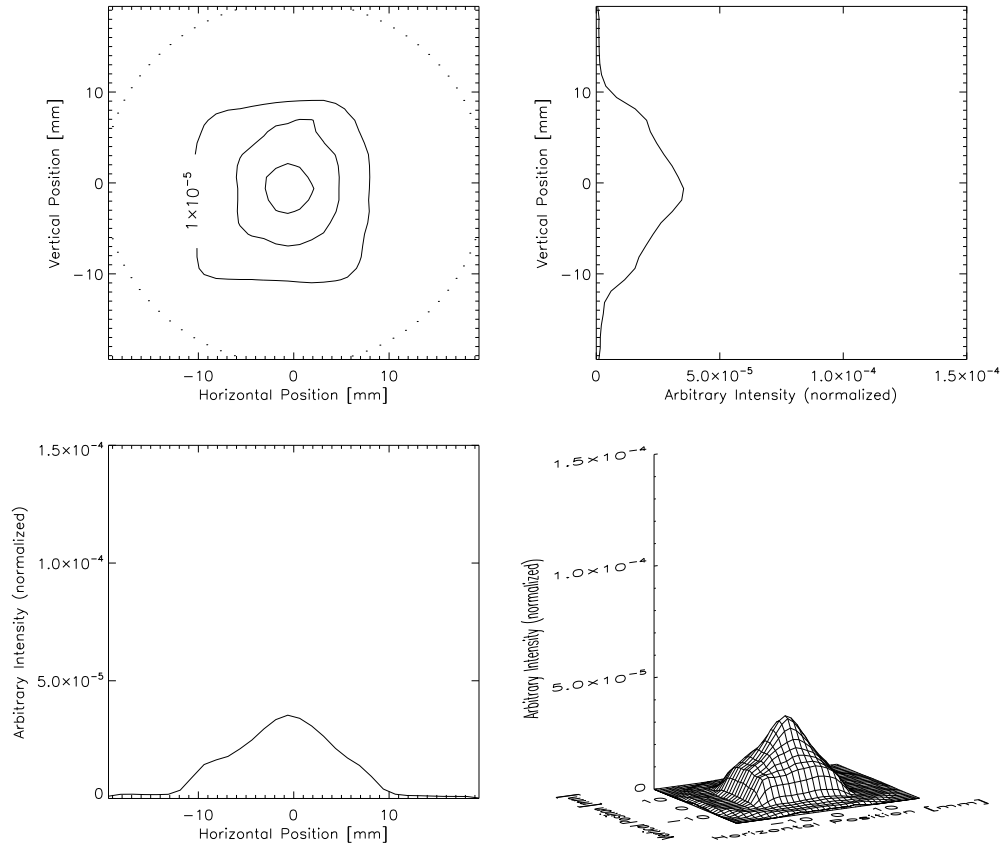


**Fig. 5.9:** Beam shape at 1.0 nA electron emission current  $i_-$  in dynamic mode at  $3.6 \times 10^{-7}$  mbar argon pressure and  $4.4 \times 10^{-8}$  mbar residual gas pressure. The plots are normalized to the intensity of the beam at 3.0 nA electron emission current in Fig. 5.11 on page 74. Top left the plot shows the  $1 \times 10^{-5}$  contour lines and top right a vertical cut through peak maximum is shown. Bottom left a horizontal cut through the peak maximum can be seen and bottom right the beam intensity is plotted as a 3D-surface.

the upper part of the profiles look more spiky than it has been observed during static mode measurements. This can easily be understood when looking at Fig. 3.1 on page 28: Because the gas inlet is mounted in the mid-

dle behind the glass capillary array, the entering gas is concentrated to the center of the source. Especially atoms and molecules, which leave the inlet in parallel to the glass capillary tubes, have a greater chance to pass compared to particles which arrive under a certain angle (see Eq. 4.2 on page 36).

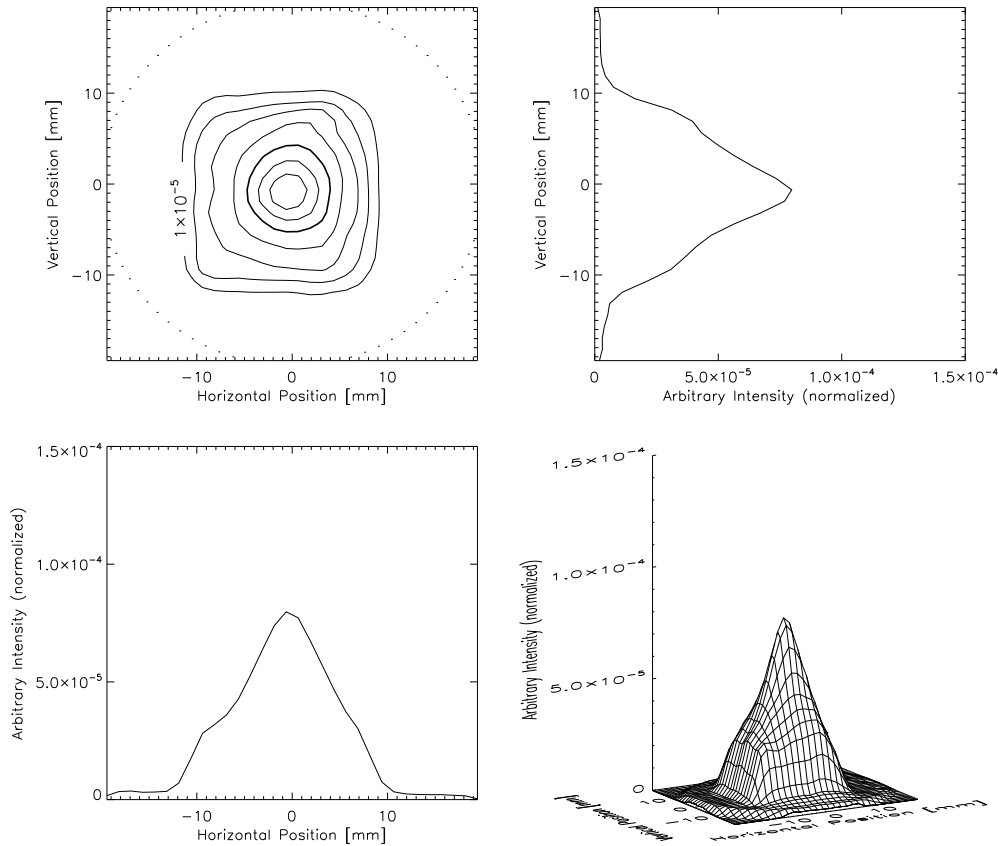


**Fig. 5.10:** Beam shape at 2.0 nA electron emission current  $i_-$  in dynamic mode at  $3.6 \times 10^{-7}$  mbar argon pressure and  $4.4 \times 10^{-8}$  mbar residual gas pressure. The plots are normalized to the intensity of the beam at 3.0 nA electron emission current in Fig. 5.11 on page 74. Top left the plot shows the  $1 \times 10^{-5}$  contour lines and top right a vertical cut through peak maximum is shown. Bottom left a horizontal cut through the peak maximum can be seen and bottom right the beam intensity is plotted as a 3D-surface.

Nevertheless, the lower part of the profiles look very similar to the static mode beam shapes: rectangular with rounded edges and a width of around

23 mm on the bottom which fits nicely to the dimension of the source exit opening (21 mm, see Fig. 3.1 on page 28).

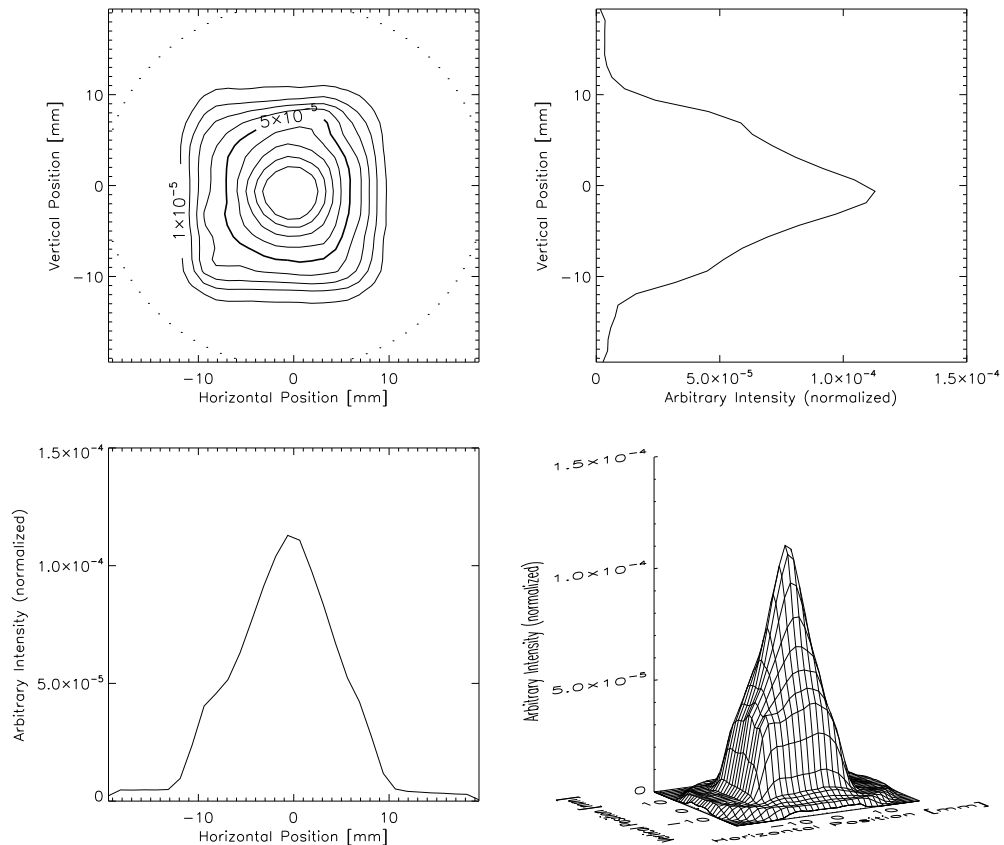


**Fig. 5.11:** Beam shape at 3.0 nA electron emission current  $i_-$  in dynamic mode at  $3.6 \times 10^{-7}$  mbar argon pressure and  $4.4 \times 10^{-8}$  mbar residual gas pressure. Top left the plot shows the  $1 \times 10^{-5}$  contour lines and top right a vertical cut through peak maximum is shown. Bottom left a horizontal cut through the peak maximum can be seen and bottom right the beam intensity is plotted as a 3D-surface.

In order to suppress this concentration of the intensity in the center, an obstacle could be mounted in front of the gas inlet preventing the direct path to the capillary plate. Such a setup would cause a lower transmission

---

probability due to a higher mixing of the gas flow directions behind the glass capillary plate, but could be compensated by a higher pressure.

Generally, the beam profile in dynamic mode is an interaction between a static component originating from the residual pressure and a dynamic component with a concentration to the beam center.

### 5.4.3 Beam dispersion

Due to the effectiveness of the detector and the electron energy of 75 eV the detector potential should be at least 100 V below the source exit potential. But when the LEIS is used together with the ROSINA instruments DFMS and RTOF, this potential will be significantly lower, probably a few volts. For this purpose it is very important to know the beam shape at such low potentials too. This information has been obtained by an extrapolation of the measured beam profiles at 100 eV, 200 eV, 300 eV, and 400 eV ion energy. All profiles were taken at a residual gas pressure of  $4.4 \times 10^{-8}$  mbar and normalized to the total counts on the screen (see Tab. 5.6). The accumulation time is 100 s each. The electron emission current  $i_-$  was adjusted to obtain similar intensities on the detector.

Counts on Screen [1/100 s]	Ion Energy [eV]	$i_-$ [nA]	Figure Nr.
$837591 \pm 915$	100	$31.2 \pm 0.2$	5.12
$831891 \pm 912$	200	$7.3 \pm 0.2$	5.13
$816979 \pm 904$	300	$4.4 \pm 0.2$	5.14
$803464 \pm 896$	400	$3.0 \pm 0.2$	5.15

**Tab. 5.6:** Characteristics for the measured beam shapes for different ion energies respectively different potentials between ion source and detector in static mode at  $4.4 \times 10^{-8}$  mbar residual gas pressure. The electron emission current  $i_-$  was adjusted to obtain similar intensities on the detector (see first column).

In Fig. 5.12 the ion energy of 100 eV is much too low for a good detection efficiency on the MCP. Thus the signal-to-noise ratio is quite high. Moreover, an enhancement at the lower left edge of the profile in the first plot of Fig. 5.12 is visible which seems to be a detector problem. When the detector is unable in pinpointing a particle then the position is automatically set to the edge of the shape.

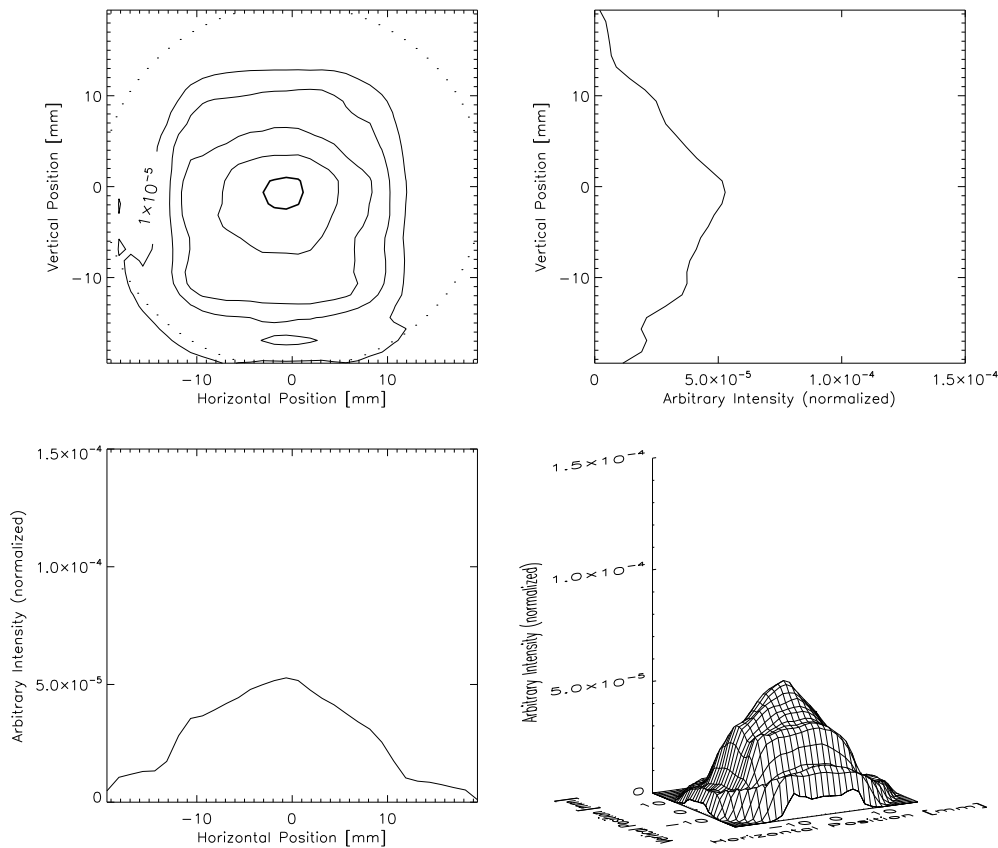


**Fig. 5.12:** Beam shape at 100 eV ion energy in static mode at  $4.4 \times 10^{-8}$  mbar residual gas pressure, normalized to the total signal. Top left the plot shows the  $1 \times 10^{-5}$  contour lines and top right a vertical cut through peak maximum is shown. Bottom left a horizontal cut through the peak maximum can be seen and bottom right the beam intensity is plotted as a 3D-surface.

Figs. 5.13, 5.14, and 5.15 show the same profiles at 200 eV, 300 eV, and 400 eV ion beam energy. The ion energy is still very low for the MCP even though the edge effects disappear.

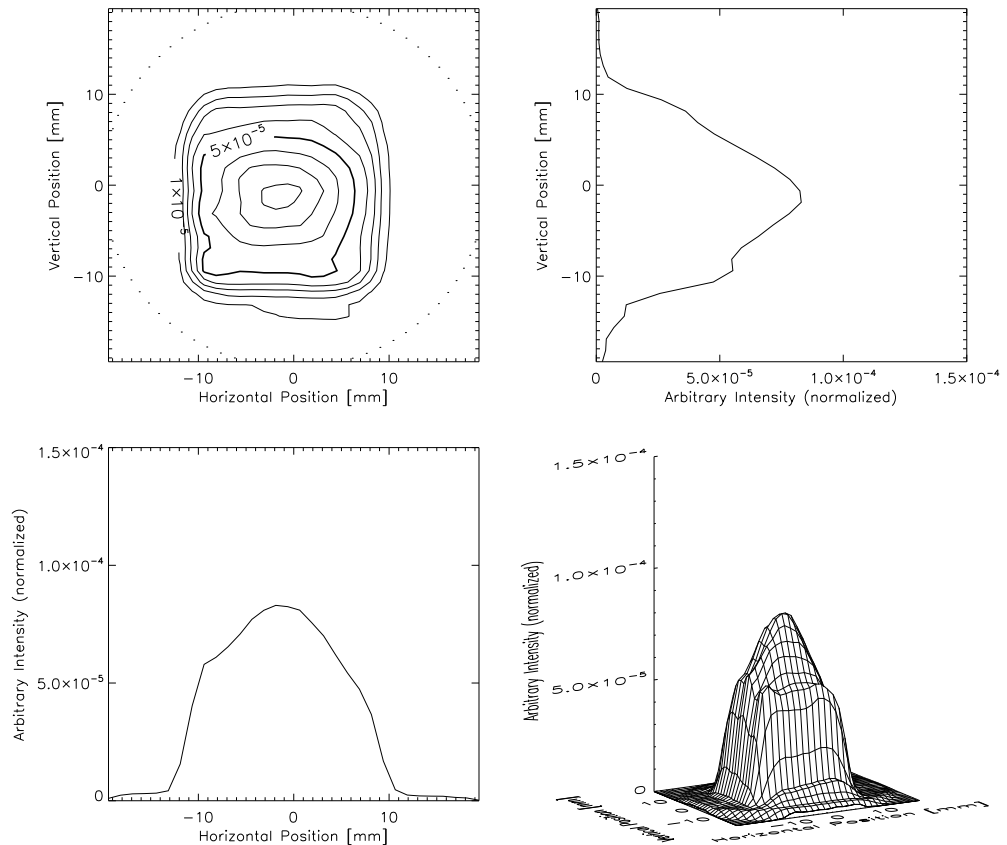


**Fig. 5.13:** Beam shape at 200 eV ion energy in static mode at  $4.4 \times 10^{-8}$  mbar residual gas pressure, normalized to the total signal. Top left the plot shows the  $1 \times 10^{-5}$  contour lines and top right a vertical cut through peak maximum is shown. Bottom left a horizontal cut through the peak maximum can be seen and bottom right the beam intensity is plotted as a 3D-surface.



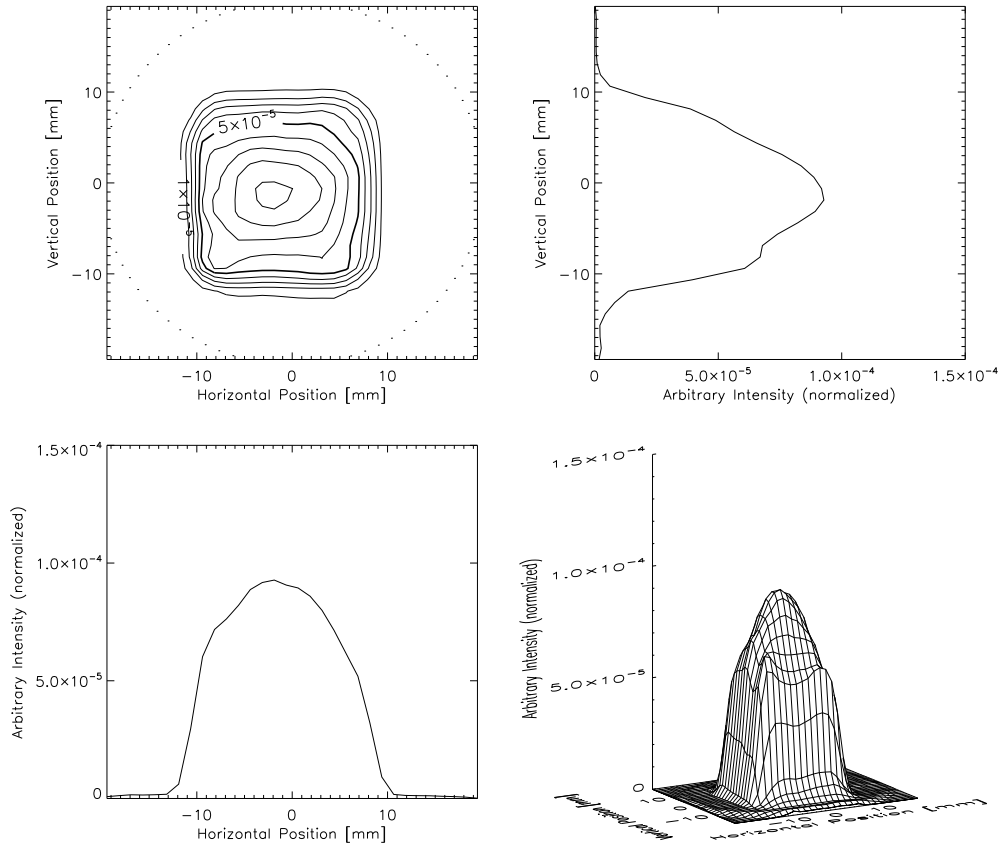


**Fig. 5.14:** Beam shape at 300 eV ion energy in static mode at  $4.4 \times 10^{-8}$  mbar residual gas pressure, normalized to the total signal. Top left the plot shows the  $1 \times 10^{-5}$  contour lines and top right a vertical cut through peak maximum is shown. Bottom left a horizontal cut through the peak maximum can be seen and bottom right the beam intensity is plotted as a 3D-surface.

The measured half widths at 50% peak height can be seen in Tab. 5.7. The  $\infty$ -entry corresponds to the minimal HWHM<sup>1</sup> obtained through the exponential fit in Fig. 5.16. This peak width would be measured at an infinite acceleration potential.

<sup>1</sup>Half Width at Half Maximum

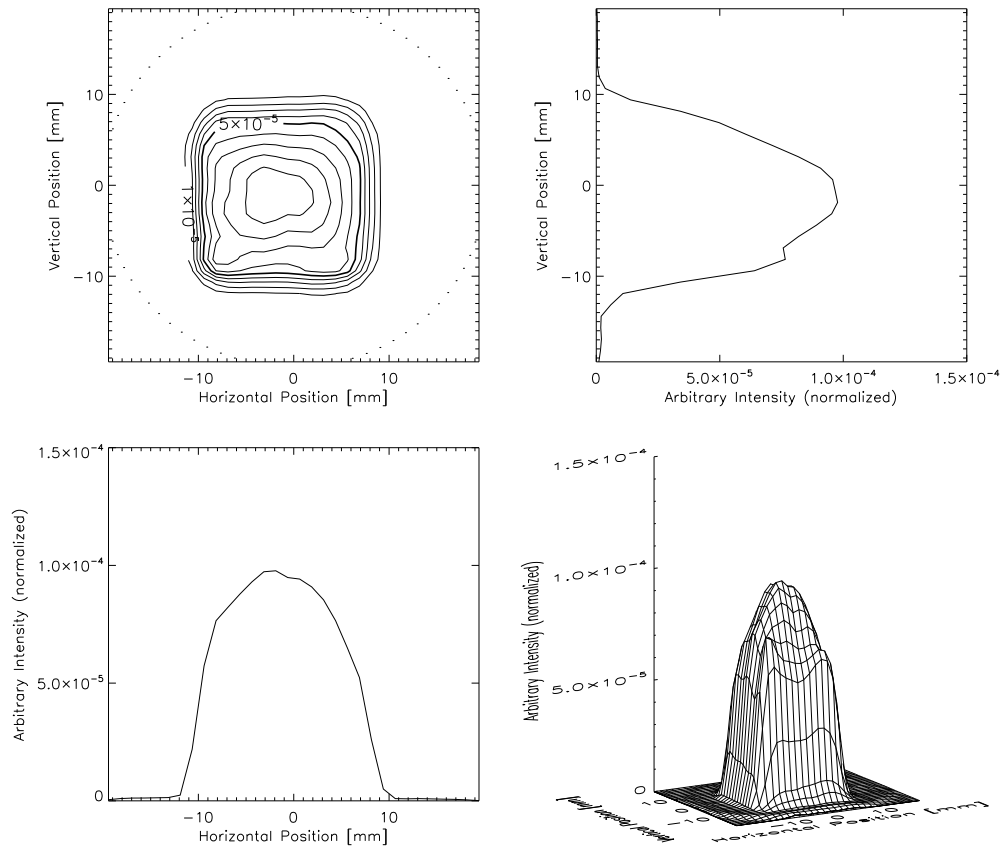


**Fig. 5.15:** Beam shape at 400 eV ion energy in static mode at  $4.4 \times 10^{-8}$  mbar residual gas pressure, normalized to the total signal. Top left the plot shows the  $1 \times 10^{-5}$  contour lines and top right a vertical cut through peak maximum is shown. Bottom left a horizontal cut through the peak maximum can be seen and bottom right the beam intensity is plotted as a 3D-surface.

On the other hand, the beam width for the 0 V potential has been gained through extrapolation of the measured results with the exponential fit in Eq. 5.3:

$$HWHM(U_{\text{ion}}) = 8.304 \text{ mm} + 6.379 \text{ mm} \cdot e^{-9.581 \times 10^{-3} \text{ eV}^{-1} \cdot U_{\text{ion}}} . \quad (5.3)$$

Thus, extrapolated with the exponential fit in Eq. 5.3, the HWHM for a  $\sim 0$  V ion beam is approximately 14.7 mm.

Acceleration potential [V]	HWHM [mm]
0	<b>14.68</b>
100	10.75 $\pm$ 0.19
200	9.25 $\pm$ 0.19
300	8.65 $\pm$ 0.19
400	8.45 $\pm$ 0.19
$\infty$	<b>8.30</b>

**Tab. 5.7:** Peak widths at 50% height. Calculated values are bold, measured values in normal font.

Tab. 5.7 can also be used to calculate the angle of beam spread for the 50% peak level when the ions are not further accelerated (0 V acceleration potential). The initial HWHM of 8.3 mm is somewhat smaller than half the cage exit grid aperture (10.5 mm; see Fig. 3.1 on page 28). After 10 mm the HWHM rises up to 14.7 mm (bold in Tab. 5.7). Therefore when the ions are not further accelerated/decelerated after leaving the source, the whole beam spread angle is equal to 65°.

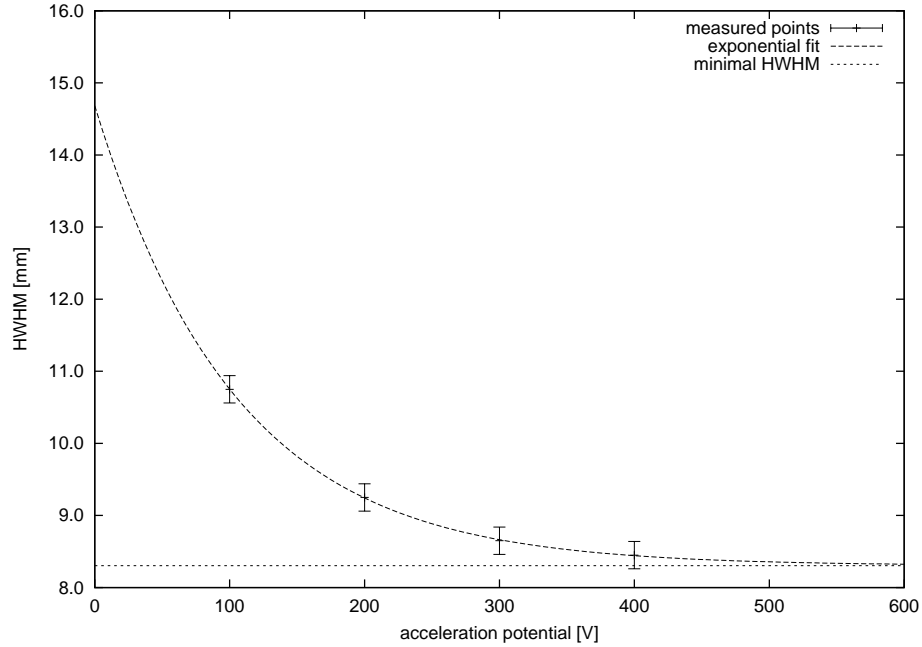


**Fig. 5.16:** Measured peak widths HWHM and exponential fit (see Eq. 5.3 and Tab. 5.7).

Furthermore, we've not only looked at the width at the 50% peak height but also at the variances of the peak widths in general and how they depend on the ion acceleration potential. In Fig. 5.12 on page 77 the noise is quite high. Therefore we compared the measured beam shapes mainly above the 30% level which should not be affected too much by the noise. We observed two major effects during the increase of the ion energy: in between 30% and 70% of its height, the peak gets narrower, and above 70%, the shape gets wider. In superposition of both effects the higher ion acceleration potential leads to a more rectangular peak shape which fits perfect to the SIMION simulations done in chapter 6 beginning on page 95.

## 5.4.4 Space charge effects

After the calculations in chapter 4.2.2 on page 45 we do not expect any major space charge effects in the ion beam.

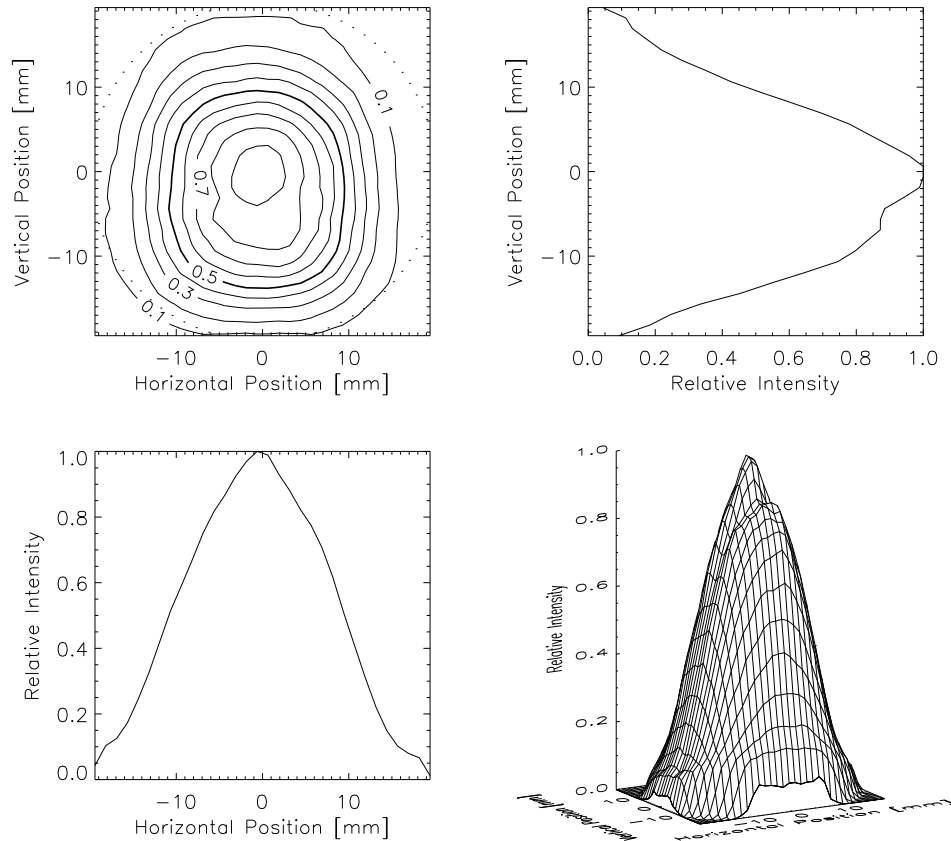


**Fig. 5.17:** Beam shape at  $8.6 \mu\text{A}$  electron emission in static mode at  $7.5 \times 10^{-9}$  mbar residual pressure ( $\approx 11$  pA ion current before intensity reduction grids). Normalized to peak height. Top left the plot shows the 0.1 contour lines and top right a vertical cut through peak maximum is shown. Bottom left a horizontal cut through the peak maximum can be seen and bottom right the beam intensity is plotted as a 3D-surface.

Nevertheless, three grids each of 10% transmission have been mounted in front of the position sensitive detector in order to allow much higher inten-

sities. Even though these grids significantly influence the beam shape, it is possible to compare the profiles of two 200 V ion beams in Figs. 5.17 and 5.18 at different intensities.

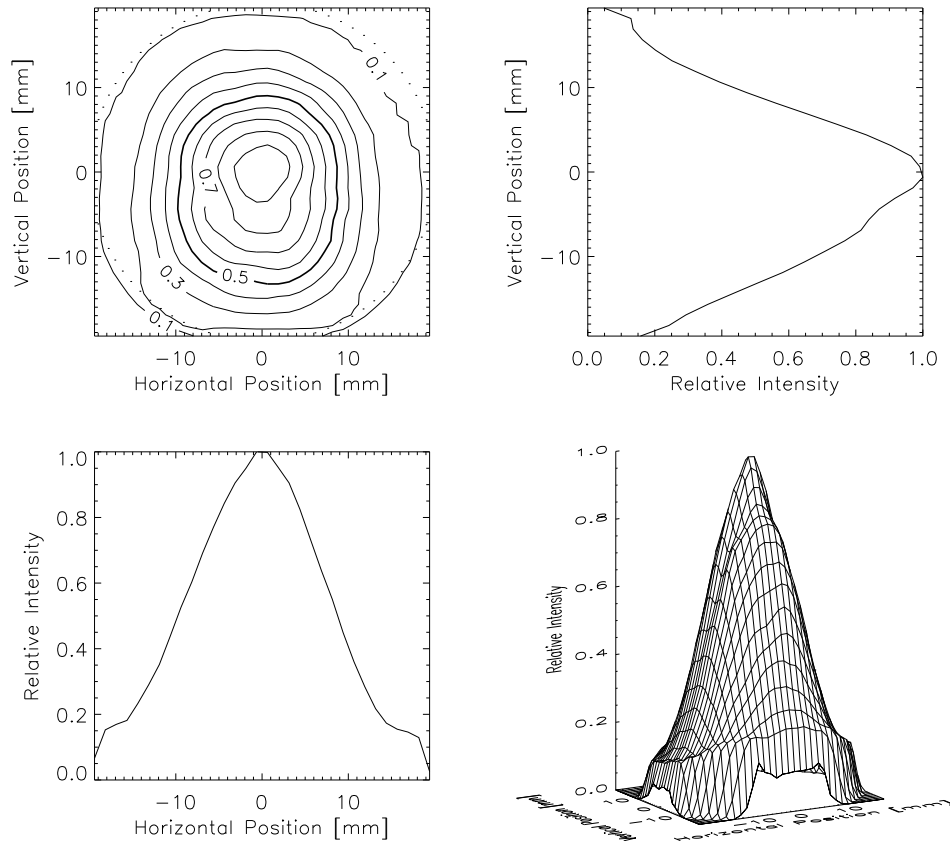


**Fig. 5.18:** Beam shape at  $8.6 \mu\text{A}$  electron emission in static mode at  $7.5 \times 10^{-9}$  mbar residual pressure and  $7.7 \times 10^{-7}$  mbar argon pressure ( $\approx 33$  pA ion current before intensity reduction grids). Normalized to peak height. Top left the plot shows the 0.1 contour lines and top right a vertical cut through peak maximum is shown. Bottom left a horizontal cut through the peak maximum can be seen and bottom right the beam intensity is plotted as a 3D-surface.

Both peaks are quite sharp. On the contrary, space charge effects would rather cause broad peaks. Furthermore, also the difference of a factor of 3 in intensity between Fig. 5.17 and Fig. 5.18 can not be seen in the shape of the beam.

### 5.5 *Energy distribution*

The energy distribution in forward direction has been measured with a retarding potential analyzer. Equal to the sensitivity (see chapter 5.3) and the beam shape measurements (see chapter 5.4), we had to take into account that not only ions with very low energy leave the source, but also electrons ( $\sim 2.2\%$  of all emitted electrons; see Tab. 5.3 on page 58) at much higher potential (75 V) and much higher intensities ( $\times 10^4$ ). In order to get rid of these electrons, an additional electron suppressor grid was mounted as shown in Fig. B.1 on page 120. The grid voltage has to be significantly above the electron energy and thus we used at least  $-100$  V. So after leaving the source, the positively charged ions were accelerated towards the electron suppressor grid whereas the electrons in the same area were repelled backwards. After the electron suppressor grid there is only the pure ion beam left which is then decelerated and its current measured on the collector anode (see setup in Fig. B.1 on page 120).

In Fig. 5.19 the measured ion current is plotted against the potential difference between the source (cage) exit and the collector anode. The absolute value of this difference is equal to the ion energy in forward direction if we assume the vast majority of the ions being only single charged (94.4% at 75 eV electron impact energy; see [SRL<sup>+</sup>95]). The measurements have been fitted with a sigmoid curve (see Eq. 5.5 on page 91).

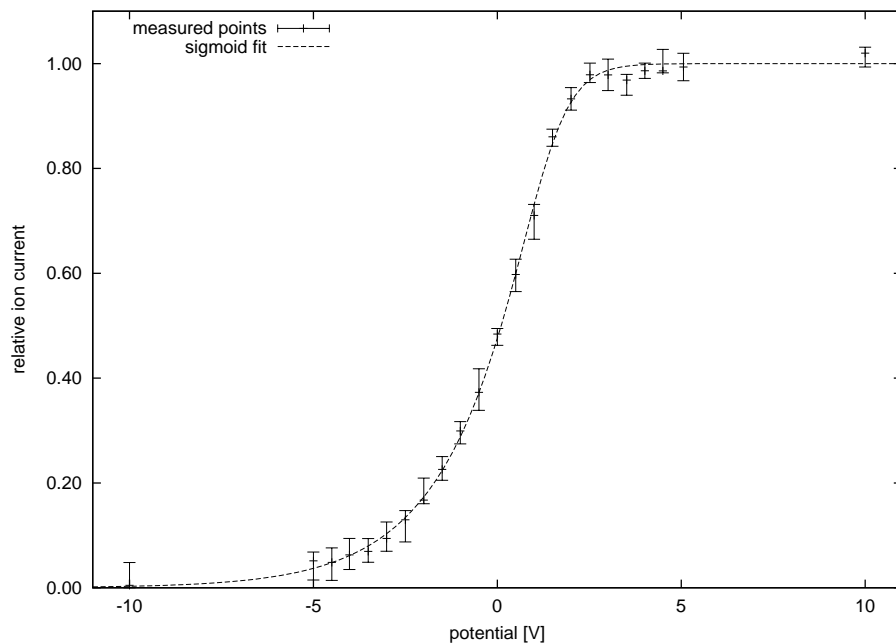


**Fig. 5.19:** Relative ion current against the retarding potential. Measurements in the static mode are fitted with a sigmoid curve. The electron suppressor grid potential is set to -100 V.

Fig. 5.20 shows the ion current distribution obtained from the changes in the relative ion current divided by the difference in potential. More precise is the direct derivation of the sigmoid curve.

A negative potential means positive ion energy since the ions have to overcome the applied potential in order to be detected. Nevertheless, in Fig. 5.20 we can see that there is also an ion beam at positive potential (negative ion energy!) which makes no sense at all. The crux to solve this problem lays



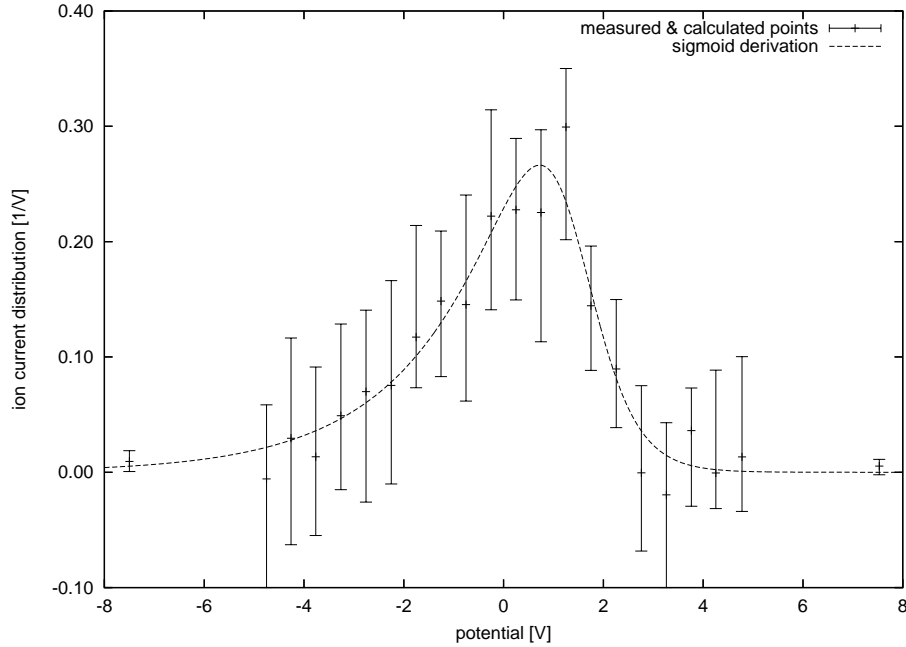


**Fig. 5.20:** Ion current distribution in static mode calculated from the measurement (see Fig. 5.19) and obtained through derivation of the sigmoid. The area beneath the curve is normalized to 1 and the electron suppressor grid potential is  $-100$  V.

in the cage exit grid. The conducting partially transparent grid separates two uniform static fields of different strengths: field free inside the source  $E_{\text{inside}} = 0$  V/cm and  $E_{\text{outside}} = -100$  V/cm due to the required electron suppressor. This leads to an altered potential distribution in the holes of the mesh [GYW73], causing the effective average potential of the mesh to become different from the potential applied to the mesh itself [RBBW98]. In other words, the electron suppressor grid pulls out extra ions because the source exit grid does not perfectly shield the inner source from the outside field. The effect, which is proportional to the difference in field strength, is in the order of 2 V for an electron suppressor grid voltage of  $-100$  V.

So we changed the potential of the electron suppressor grid from  $-100$  V to  $-200$  V and extrapolated to  $0$  V suppressor potential, which can be seen for the static mode in Fig. 5.21 and for the dynamic mode in Fig. 5.22. Even though we did not get rid of the effect, the results, represented by the solid lines in both figures look much better.

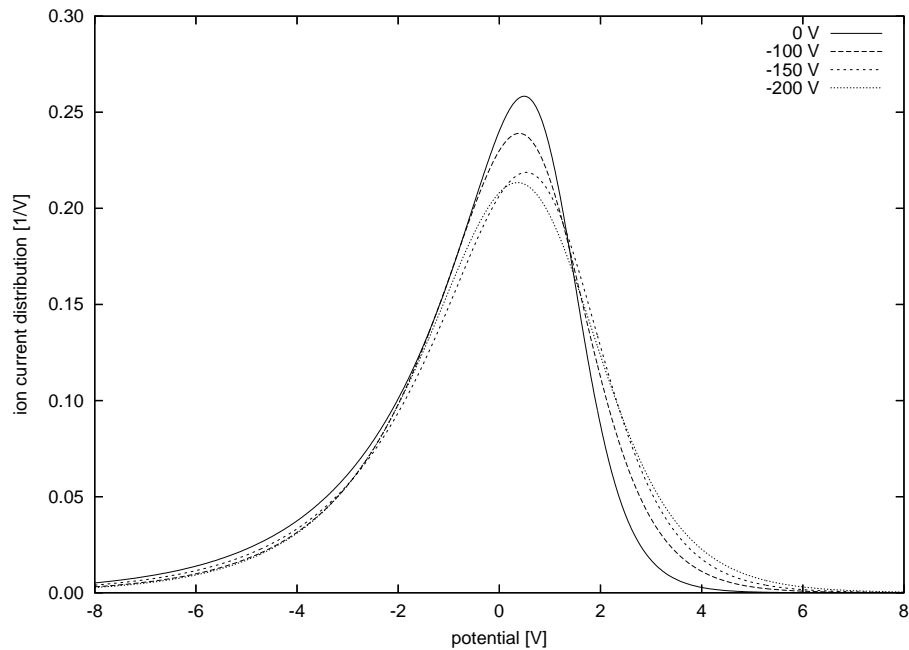


**Fig. 5.21:** Ion current distributions at different electron suppressor grid potentials in the static mode. Curves for  $-100$  V,  $-150$  V, and  $-200$  V are measured whereas the curve for  $0$  V has been extrapolated. All areas beneath the curves are normalized to 1.

The difference caused by the electron suppressor grid potentials seems to be more prominent in the dynamic mode. At least for the high voltage, e.g.  $-200$  V, the curve is quite different to its equivalent in the static mode.

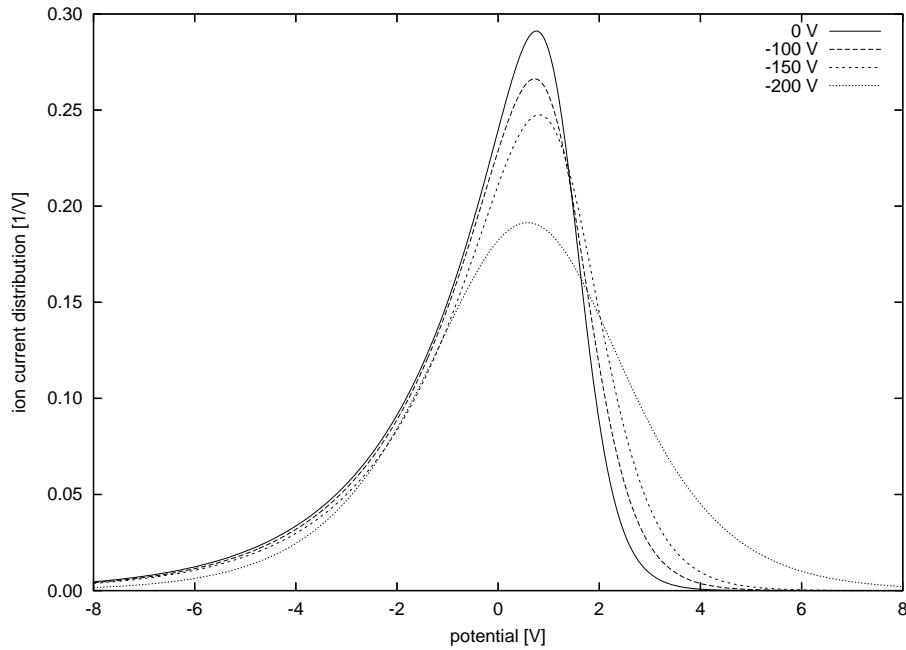


**Fig. 5.22:** Ion current distributions at different electron suppressor grid potentials in the dynamic mode. Curves for  $-100$  V,  $-150$  V, and  $-200$  V are measured whereas the curve for  $0$  V has been extrapolated. All areas beneath the curves are normalized to 1.

In both modes the energy distribution is slightly shifted to the higher potentials respectively the maximum of the ion current distribution is slightly above the  $0$  V potential ( $\sim 0.5$  V). This could be caused by noise in the electronics or a small offset in the voltage power supply.

Fig. 5.23 presents both final results for static and dynamic mode. The ion current distribution for the dynamic mode is slightly narrower and steeper compared to the static mode curve. This is coherent with the fact that the dynamic mode contains mainly gas that passed through the glass capillary array. Since this part of the gas moves only in forward direction, the energy distribution gets narrower.

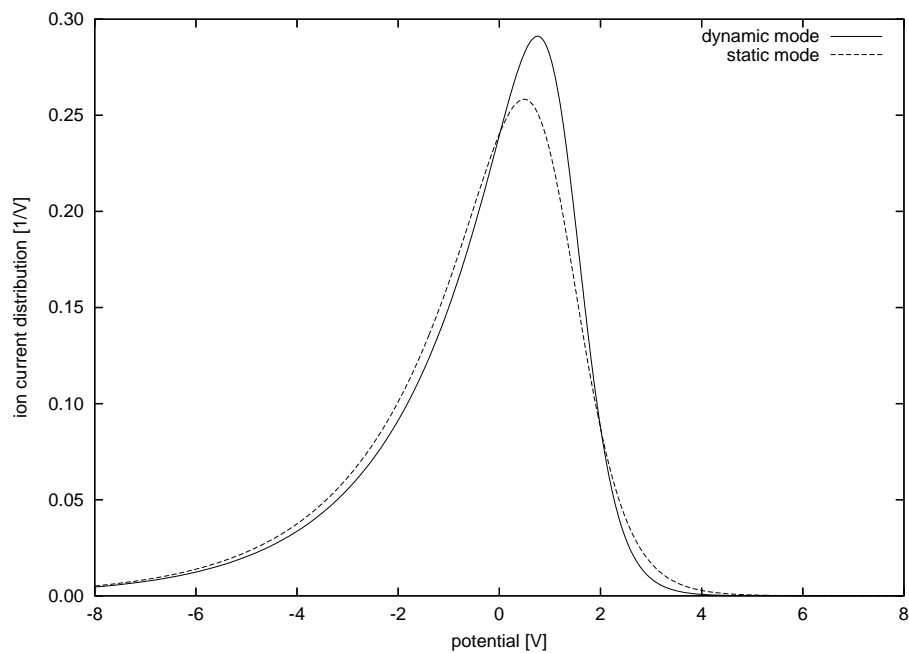


**Fig. 5.23:** Comparison between energy distributions in static and dynamic mode. The integrals of both curves are normalized to 1.

But there is always residual gas in the source independent of the used mode. This residual part is estimated to behave like static mode gas, where the particle's flying direction is distributed randomly. The dynamic mode is thus the sum of a specific mixture of gas introduced into the source moving in forward direction and residual gas that behaves like in static mode.

In both modes around 90% of all ions have kinetic energies in forward direction below 3.5 eV. Since the LEIS can be floated up to several volts, one can cut off all ions with energies below the applied potential. This makes it possible to limit, at the cost of intensity, e.g. 90% of the ions to energies

below 1 eV. On the other hand, it is possible, also by floating of the whole source, to further accelerating the ions. This generates an ion beam with an narrow energy bandwidth at the applied potential e.g.  $E_{\text{kin, forward}} = 400$  eV and  $\Delta E_{\text{kin, forward}} = 3.4$  eV.

Both curves in Fig. 5.23 can be described by the following equation:

$$f(p) = \frac{a \cdot c \cdot e^{-\frac{p-p_0}{b}}}{b \cdot \left(1 + e^{-\frac{p-p_0}{b}}\right)^{c+1}}, \quad (5.4)$$

where  $p$  is the applied retarding potential,  $a$ ,  $b$ ,  $c$ , and  $p_0$  are fitted parameters, listed in Tab. 5.8.

Parameter	Static mode	Dynamic mode	Note
$a$	1.00	1.00	scaling parameter
$b$	0.54 V	0.40 V	exponential parameter
$c$	0.27	0.20	exponential parameter
$p_0$	1.2 V	1.4 V	potential offset parameter

**Tab. 5.8:** Fitted parameters for the obtained retarding potential distribution.

The relative fraction of ions reaching the collector anode at potential  $p_{\text{max}}$  can be calculated with the integral of Eq. 5.5 and Tab. 5.8:

$$F(p \leq p_{\text{max}}) = \int_{-\infty}^{p_{\text{max}}} \frac{a \cdot c \cdot e^{-\frac{p-p_0}{b}}}{b \cdot \left(1 + e^{-\frac{p-p_0}{b}}\right)^{c+1}} dp = \frac{a}{\left(1 + e^{-\frac{p_{\text{max}}-p_0}{b}}\right)^c}. \quad (5.5)$$

For example  $F(p_{\text{max}}) = 0.1$  for  $p_{\text{max}} = -3.41$  V in static mode means that only 10% of the ions have energies above 3.41 eV in forward direction (under the assumption they are all single charged).

### 5.6 ROSINA RTOF ion measurements setup

For the first ion measurements of ROSINA RTOF, the LEIS has been mounted in the CASYMS vacuum chamber at the University of Bern. The setup can be found in Figs. B.5 and B.6 on page 124 and following.

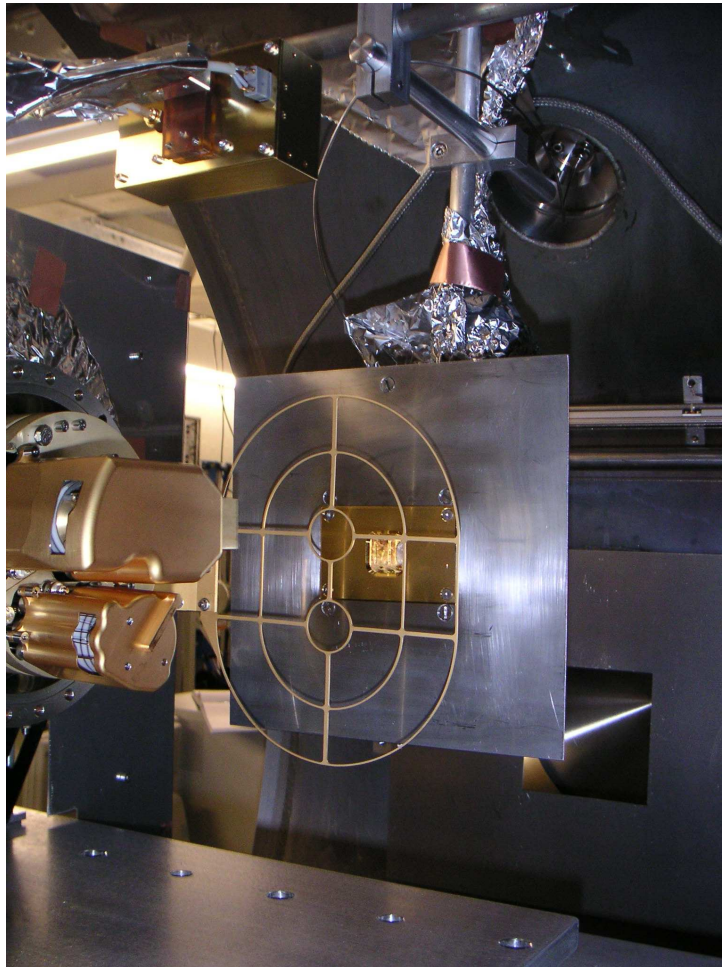


**Fig. 5.24:** ROSINA RTOF mounted in the CASYMS chamber on a moveable table. The Low Energy Ion Source is attached in front and the Faraday cup above the two sources and the ion attraction grid, respectively.

The LEIS has been mounted on three fully adjustable arms (see chapter 3.1) which allows all demanded relative positions pertaining to the RTOF sources and the attraction grid. RTOF is mounted on a moveable table and can be

---

tilted  $\pm 10^\circ$  around two axis and be moved in vertical direction, even during measurements. Therefore when moving the table vertically, an additional Faraday Cup (see Fig. B.3 on page 122) can be placed in front of the LEIS. The aperture of this Faraday cup is equal to the RTOF orthogonal source entrance for cross calibration. The circuit diagram of the Faraday cup power supply can be found in Fig. B.9 on page 128.

The nominal mounting position in Fig. 5.24 of the LEIS is typically in front of the RTOF orthogonal source in a distance of at least 5 cm to the RTOF attraction grid (about two times the structure dimensions of the attraction grid of  $\sim 2.5$  cm to minimize lens effects). All cables and non conducting surfaces close the the ion flight path need to be at least covered with aluminium foil.





## 6. ION SOURCE SIMULATION WITH SIMION

The Low Energy Ion Source has been simulated with SIMION 3D Version 7.0 from Idaho National Engineering and Environmental Laboratory. The source geometry has been exported from CatiaV5 CAD via stl (stereolithography) files. A program called "SL Toolkit" has been used to convert and import the whole array into SIMION.

SIMION [Dah00] makes use of potential arrays that define the geometry and potentials of electrodes and magnetic poles. The potentials of points outside electrodes and poles are determined by solving the Laplace equation by finite difference methods:

$$\Delta V = 0 \quad . \quad (6.1)$$

The Laplace equation constrains all electrostatic and static magnetic potential fields to conform to a zero charge volume density assumption. The equation assumes that there are no space charge effects.

The Laplace equation really defines the electrostatic or static magnetic potential of any point in space in terms of the potentials of surrounding points. For example, in a 2-dimensional electrostatic field represented by a very fine mesh of points the Laplace equation is satisfied (to a good approximation) when the electrostatic potential of any point is estimated as the average of its four nearest neighbor points:

$$V = \frac{V_1 + V_2 + V_3 + V_4}{4} \quad .$$

Ions and electrons can be flown within the simulated volume and their trajectories change according to the fields of the potential array instances they fly through.

SIMION utilizes potential arrays to define electrostatic and magnetic fields. Potential arrays are dimensioned by the number of so-called voxels in each dimension (x, y, and z). In order to save calculation time or to gain more

precision, two types of symmetries are allowed in SIMION: Planar (2D and 3D arrays) and cylindrical (2D array only). The maximum number of voxels is limited to 50'000'000, however, by mirroring the source, it was possible to increase the resolution of the potential array by a factor of  $\sqrt[3]{2}$ . Even though the microtip holder and the microtip itself are not perfectly symmetrical regarding to the cutting plane, the influence on the ions is expected to be negligible since the ionization zone is separated by two grids from these two elements. On the other hand, the energy of the electrons is way to high to be influenced by this slight asymmetry. The attained voxel dimension for the LEIS is thus 0.2 mm and therefore its volume 0.008 mm<sup>3</sup>. The grids of the source have been replaced in SIMION with ideal grids (uniform potential without any grid effects close to the wires) since the dimensions of the real grids are noticeable smaller than a single voxel dimension (wire thickness 0.035 mm).

Electrode	Potential [V]
Microtip holder	0
Microtip front	0
Microtip back	-75
Microtip grid	10
Ionization box	0
Ionization box exit	0
Electron collector grid	10
Electron collector	50
Cage exit	0
ext. Ion collector	0, -100, -200, -300, and -400

**Tab. 6.1:** Used potentials for the electrodes in SIMION.

Fig. 6.1 shows a slice of the source in SIMION. On the left side, in direction of the ions, a collector electrode with an additional grid (grids are represented by surfaces with a thickness of one voxel) have been implemented. The distance of this collector to the cage of the source is typically 1 cm and therefore the same as it was during the measurements with the position sensitive MCP detector in chapter 5.4. This setup allows to compare simulated beam shapes to the actual measured ones.

Furthermore, the potentials were set to the typical values listed in Tab. 6.1

(see also Tab. 3.2 on page 33). The microtip front voltage has been set to 0 volts which is the case for maximum electron emission ( $U_{\text{microtip back}} - U_{\text{microtip front}} = -75 \text{ V}$ ).

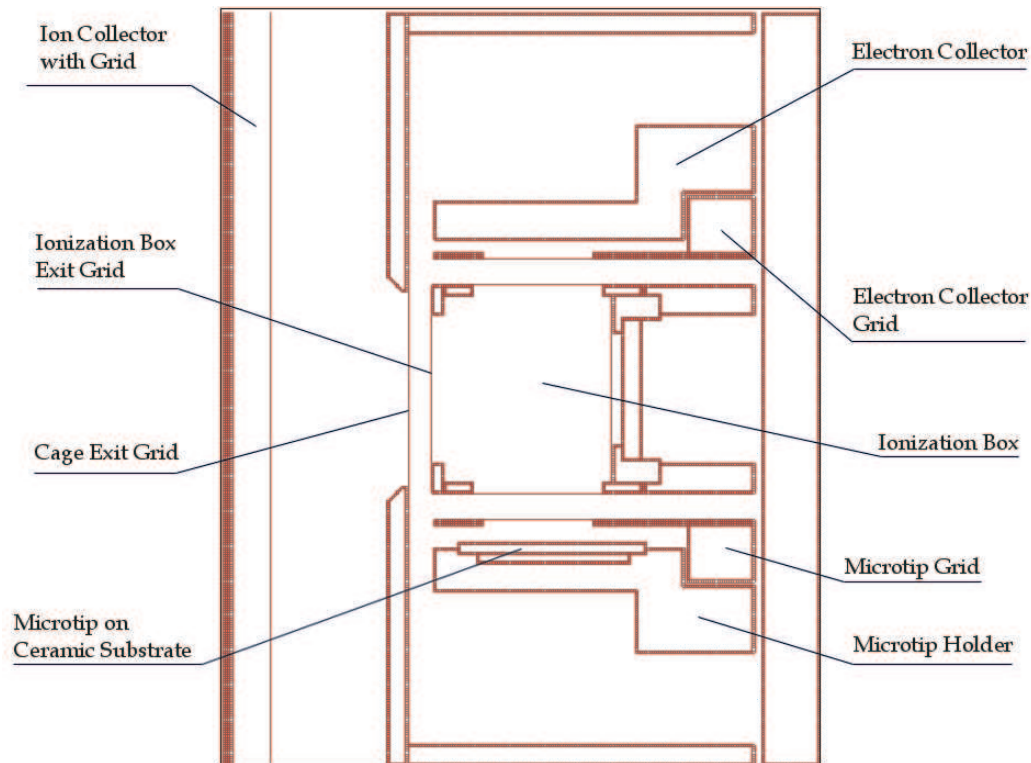


**Fig. 6.1:** Cut through the Low Energy Ion Source potential array (see also Fig. 3.1 on page 28). On the lower part the microtip can be seen as well as the electron collector on the upper side. The electron flight direction is therefore upwards and ions move from the right to the left in this picture. The large electrode with grid on the left edge is the ion collector.

Fig. 6.2 shows typical electron trajectories inside the source. Most electrons hit the electron collector anode or at least other electrodes within the source. It was not possible to reproduce the  $\sim 2\%$  of electrons which leave the source as measured in Tab. 5.3 on page 58 without significantly increasing the  $30^\circ$  opening angle of the microtip emission [PB94]. Effects that can't be simulated by SIMION, like bouncing of electrons on surfaces, are probably responsible for this electron current.

Fig. 6.3 shows the setup in the potential energy view. Positive charged ions

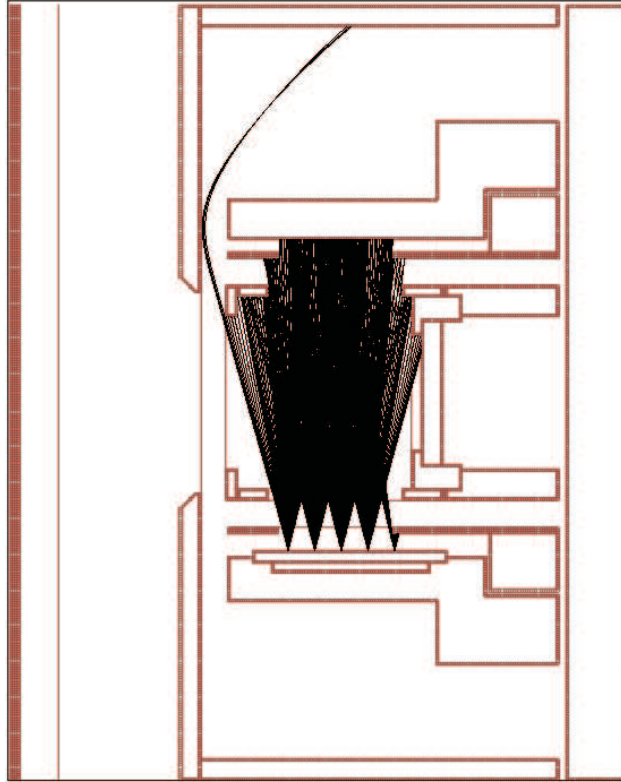


**Fig. 6.2:** Cut through the Low Energy Ion Source potential array including trajectories of electrons emitted by the microtip in a 30 degrees angle (see [PB94]).

tend to fly downwards in order to minimize their potential energy. Ions that leave the source are then in this case accelerated towards the lowest part which is the collector electrode with a grid at  $-100$  V. On the contrary the large elevation belongs to the electron collector, which is at 50 volts, the two smaller rises belong to the two grids at 10 volts each. Both grids work as repeller for the ions which move perpendicular to the main direction. One can see that the whole ion flight path inside the source is quite homogeneous on equal potential i.e. ground potential. The real grids are not as ideal as in the simulation, but nevertheless the true potentials are expected to look quite similar.

The dimensions of some parts of the microtip are much smaller than the

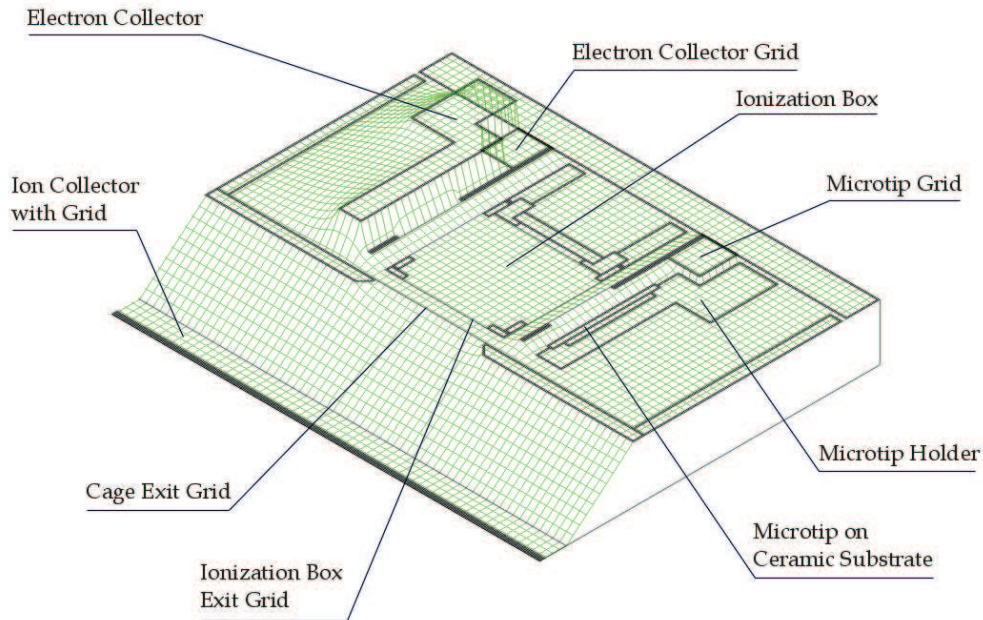


**Fig. 6.3:** Potential energy view of the potential array. The setup is given in Tab. 6.1. The highest part is the electron collector electrode at 50 V and the lowest part is the external ion collector (with grid) at  $-100$  V. Also the microtip grid and the electron collector grid at 10 volts can be seen. All other parts are on ground potential.

resolution of the simulation. The whole front side of the microtip in the simulation is set to 0 volts which is actually not the case for the real microtip because e.g. half of the bonding wires are on the microtip back potential ( $-75$  volts) and not shielded. Anyway the influence on the ions is very marginal due to the two grids separating the ions from the microtip and the bonding wires.

Unfortunately but not surprisingly we were not able to reproduce the actual measured energy distribution with this simulation. The ions more or less kept their initial thermal energy. The true energy distribution, measured in chapter 5.5, is also influenced by noise of the used power supplies and various other effects which cannot be simulated with SIMION. Therefore we used the energy distribution measured with the retarding potential analyzer as initial

energy of the ions in the simulation.

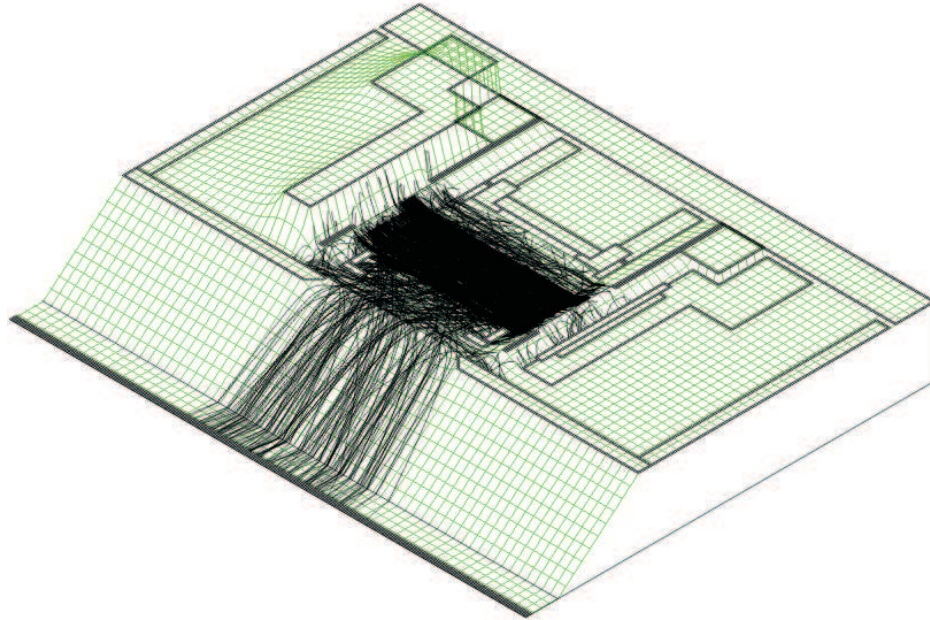


**Fig. 6.4:** Potential Energy view of the potential array including calculated ion trajectories. The ions are generated homogeneously (in position and with forward direction) in the ionization zone which is typical for the static mode, where no additional gas is introduced through the glass capillary array.

Fig. 6.4 shows the potential energy view together with calculated ion trajectories. A set of 500'000 ions (SIMION maximum) has been used in order to get the best statistics as possible. All ions are generated on random positions and with forward directions within the ionization zone, which is typical for the static mode (no gas is introduced through the glass capillary array). The ion energy was given according to the measured static mode energy distribution showed in chapter 5.5 on page 85 and following.

Additionally to the acquired beam shapes with the position sensitive MCP detector, it was also possible to simulate the case where the collector was just on 0 volts. In this setup the ion energy is typically below 4 volts (see Fig 5.21 on page 88) and the efficiency of the MCP detector gets very small, even below the detector noise.

Once the ions left the source they are recorded when passing the collector

---

grid. The following pictures show the simulated beam shapes at the position of the collector grid at different potentials, namely  $U_{\text{Collector Grid}} = 0 \text{ V}$ ,  $-100 \text{ V}$ ,  $-200 \text{ V}$ ,  $-300 \text{ V}$ , and  $-400 \text{ V}$ .

Fig. 6.5 shows the simulated beam shape without further ion acceleration towards the collector grid. The ion energy distribution stays more or less at the initial energy obtained from chapter 5.5 on page 85 and following. As already mentioned, it is not possible to use a MCP detector for ions at these low energies, thus there exists no experimental dataset for this beam shape. Nevertheless, the width at half maximum fits very nicely to the value extrapolated from the measurements in chapter 5.4.3 (see Fig. 6.10 on page 107). The simulated beam shape at 100 eV ion energy in Fig. 6.6 not only looks different to the 0 eV case but also to its measured counterpart in Fig. 5.12 on page 77. The peak is quite narrow and the top is flat. Since the initial energy of the ions is less than 10% of the forward acceleration potential, the lateral expansion is quite suppressed. Furthermore no additional peak broadening caused by collisions with grids, noise in the detector signal cables, etc. affects the simulated beam shapes.

Compared to SIMION, the MCP has detection problems for ions at  $\sim 100 \text{ eV}$  energy (low detection efficiency), noise in the electronics, and also some negative effects when the beam hits the surface on the edge of the detector. Due to all these effects it is difficult to compare simulated and measured peak shapes at such low ion energies.

Figs. 6.6, 6.7, 6.8, and 6.9 are very similar. The largest change can only be observed in beam width. This is due to the fact that the initial ion energy is always the same, but the forward potential changes from 100 V up to 400 V.

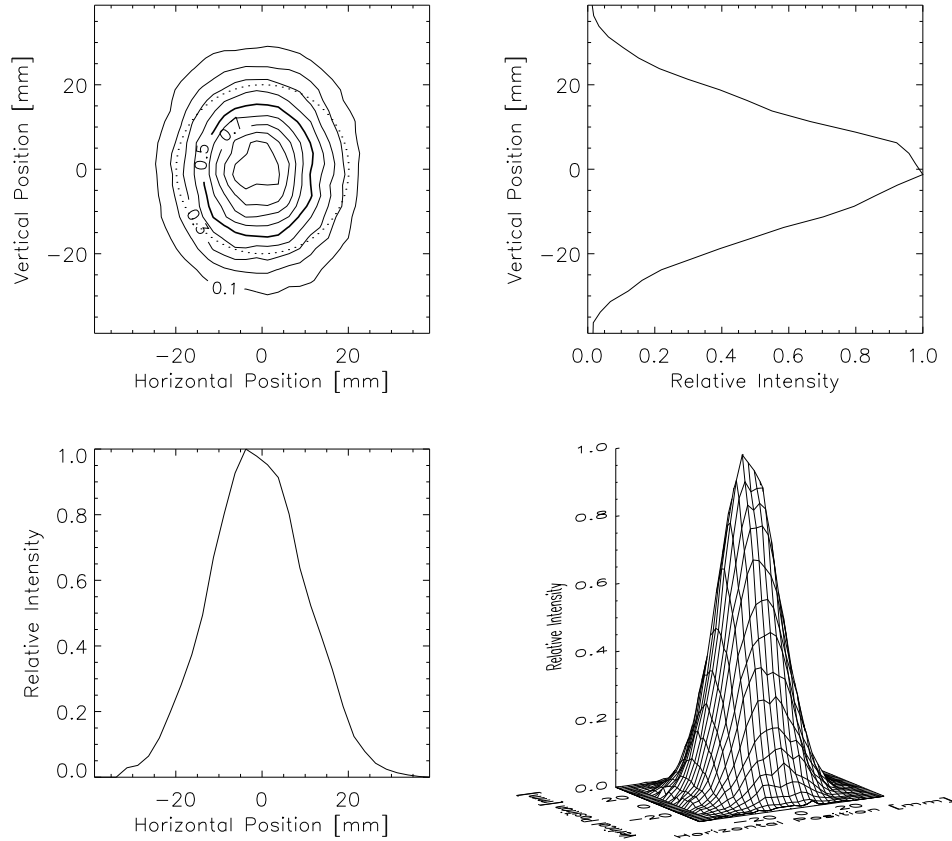


**Fig. 6.5:** Beam shape at 0 V acceleration potential ( $U_{\text{Collector Grid}} = 0$  V,  $U_{\text{Cage}} = 0$  V) normalized to its height. Top left the plot shows the 0.1 contour lines and top right a vertical cut through peak maximum is shown. Bottom left a horizontal cut through the peak maximum can be seen and bottom right the beam intensity is plotted as a 3D-surface. Note that the 8 cm vertical and horizontal ranges are both twice the standard 4 cm from the other figures. For comparison, the dotted circle with a 2 cm radius in the first plot shows the active area of the MCP detector used during the measurements in chapter 5.4.



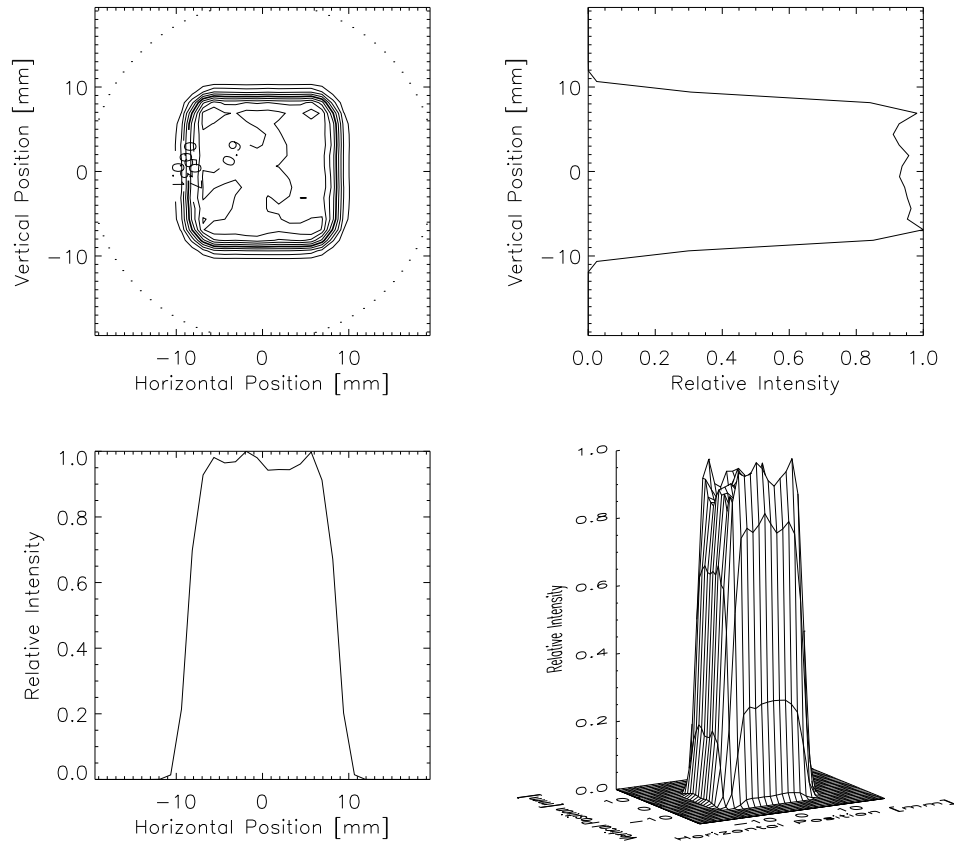


**Fig. 6.6:** Beam shape at 100 V acceleration potential ( $U_{\text{Collector Grid}} = -100$  V,  $U_{\text{Cage}} = 0$  V) normalized to its height. Top left the plot shows the 0.1 contour lines and top right a vertical cut through peak maximum is shown. Bottom left a horizontal cut through the peak maximum can be seen and bottom right the beam intensity is plotted as a 3D-surface. For comparison, the dotted circle with a 2 cm radius in the first plot shows the active area of the MCP detector used during the measurements in chapter 5.4.

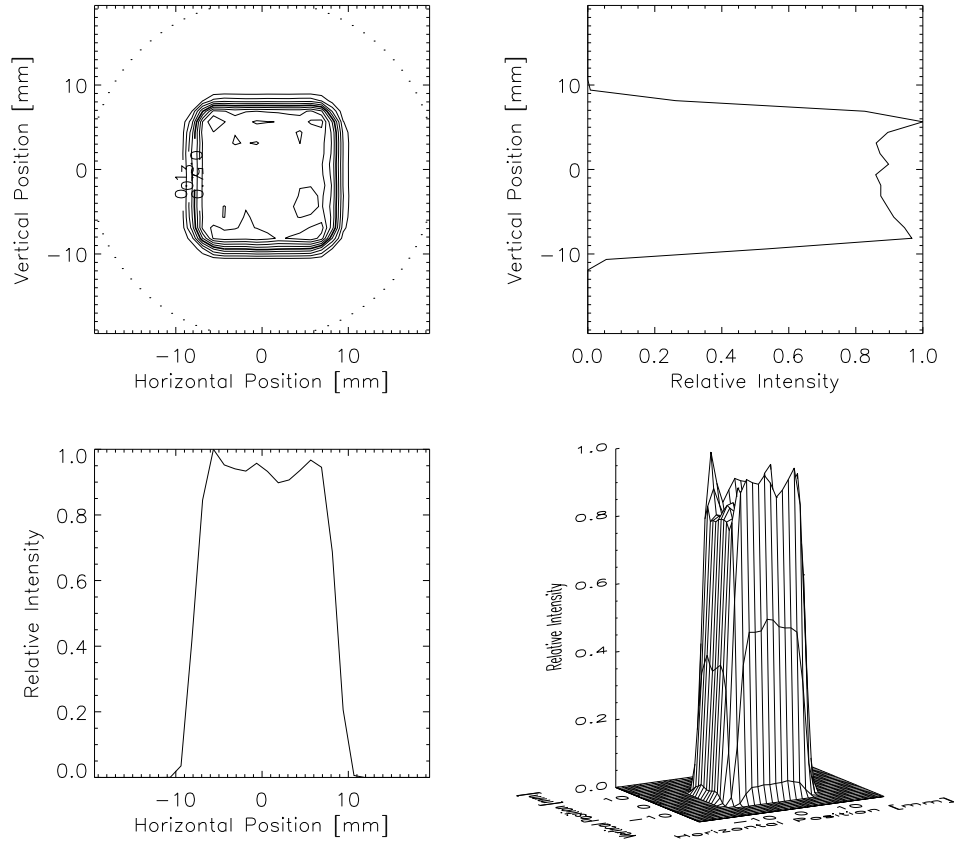


**Fig. 6.7:** Beam shape at 200 V acceleration potential ( $U_{\text{Collector Grid}} = -200$  V,  $U_{\text{Cage}} = 0$  V) normalized to its height. Top left the plot shows the 0.1 contour lines and top right a vertical cut through peak maximum is shown. Bottom left a horizontal cut through the peak maximum can be seen and bottom right the beam intensity is plotted as a 3D-surface. For comparison, the dotted circle with a 2 cm radius in the first plot shows the active area of the MCP detector used during the measurements in chapter 5.4.

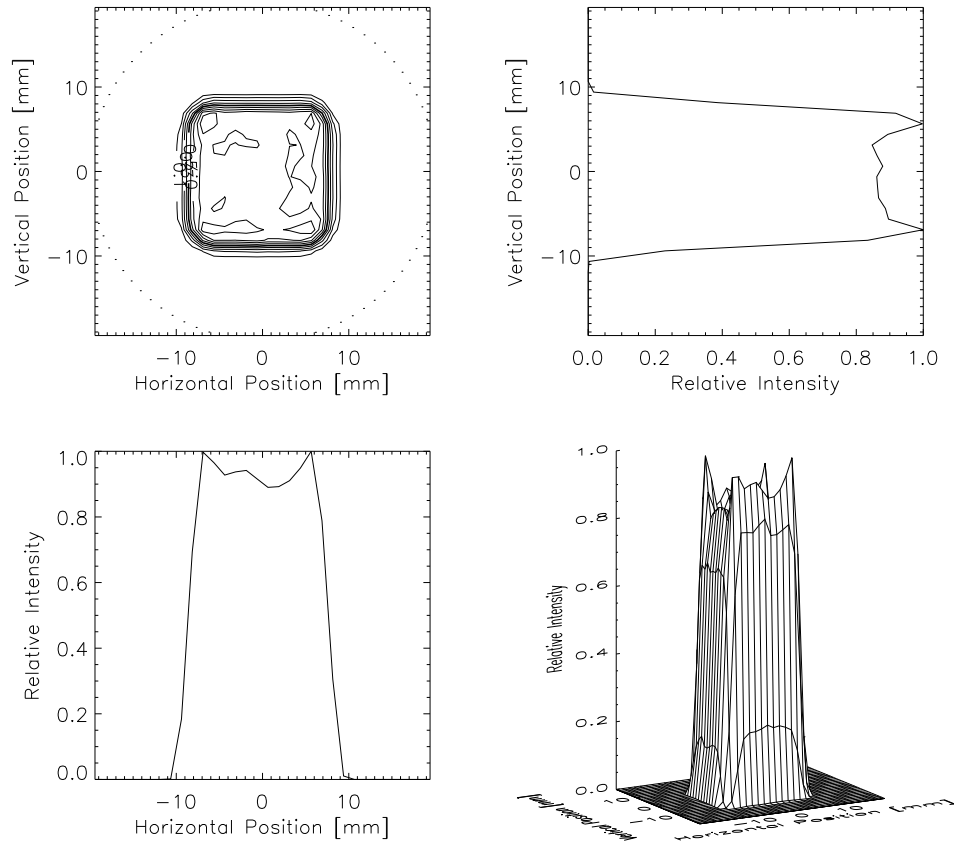


**Fig. 6.8:** Beam shape at 300 V acceleration potential ( $U_{\text{Collector Grid}} = -300$  V,  $U_{\text{Cage}} = 0$  V) normalized to its height. Top left the plot shows the 0.1 contour lines and top right a vertical cut through peak maximum is shown. Bottom left a horizontal cut through the peak maximum can be seen and bottom right the beam intensity is plotted as a 3D-surface. For comparison, the dotted circle with a 2 cm radius in the first plot shows the active area of the MCP detector used during the measurements in chapter 5.4.

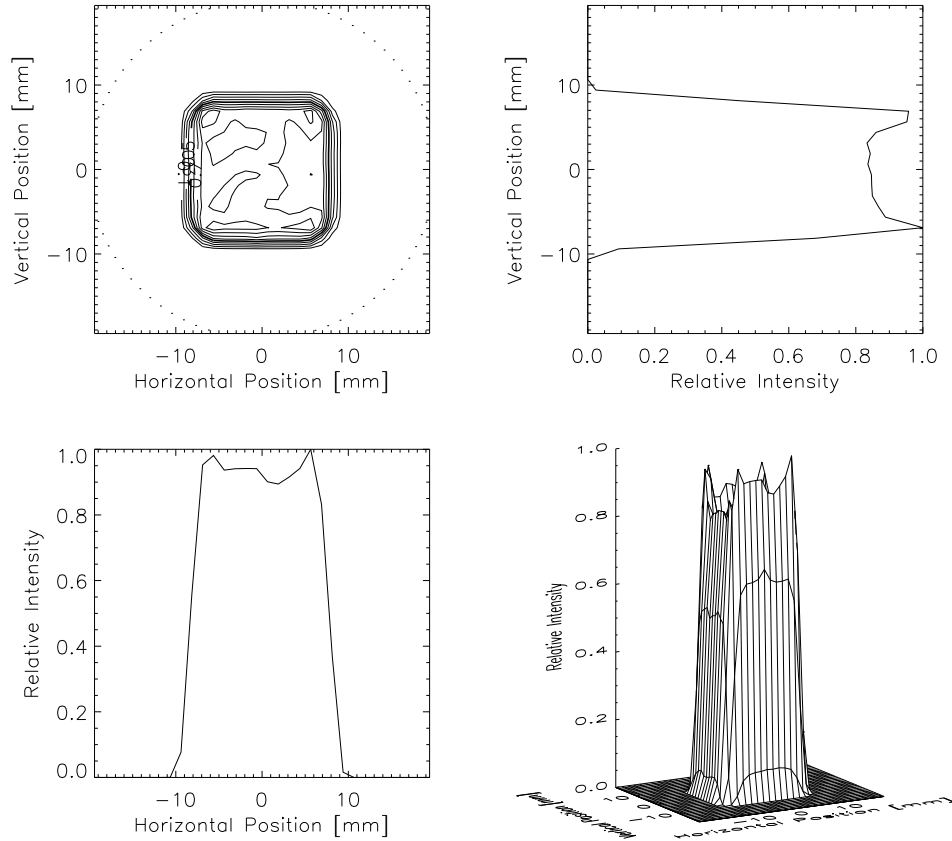


**Fig. 6.9:** Beam shape at 400 V acceleration potential ( $U_{\text{Collector Grid}} = -400$  V,  $U_{\text{Cage}} = 0$  V) normalized to its height. Top left the plot shows the 0.1 contour lines and top right a vertical cut through peak maximum is shown. Bottom left a horizontal cut through the peak maximum can be seen and bottom right the beam intensity is plotted as a 3D-surface. For comparison, the dotted circle with a 2 cm radius in the first plot shows the active area of the MCP detector used during the measurements in chapter 5.4.

In Fig. 6.10 the beam widths at half maximum of Figs. 6.5 to 6.9 are added to Fig. 5.16 on page 82. The minimum peak width is nearly the same for measurements and simulation ( $\approx 8.3$  mm). Also, the simulation of the 0 V acceleration potential seems to fit quite well the extrapolated value for the beam width from the measurements ( $\approx 14.5$  mm). But especially for the 100 V potential case, the differences are quite large and the relative error can reach up to 50%. This can be explained with the already mentioned detecting problems of MCPs at these low ion energies. This effect gets smaller as the ion energy increases, and the simulated peak shape fits better to the actually measured one. The same effect can also be observed in the measurements: the peak gets more closer to a rectangular beam profile the higher the ion energy is. In the simulation this effect is already dominant at 100 V, in the MCP detector measurements several hundreds of volts are required (see Figs. 5.12 to 5.15 on page 77 and following).

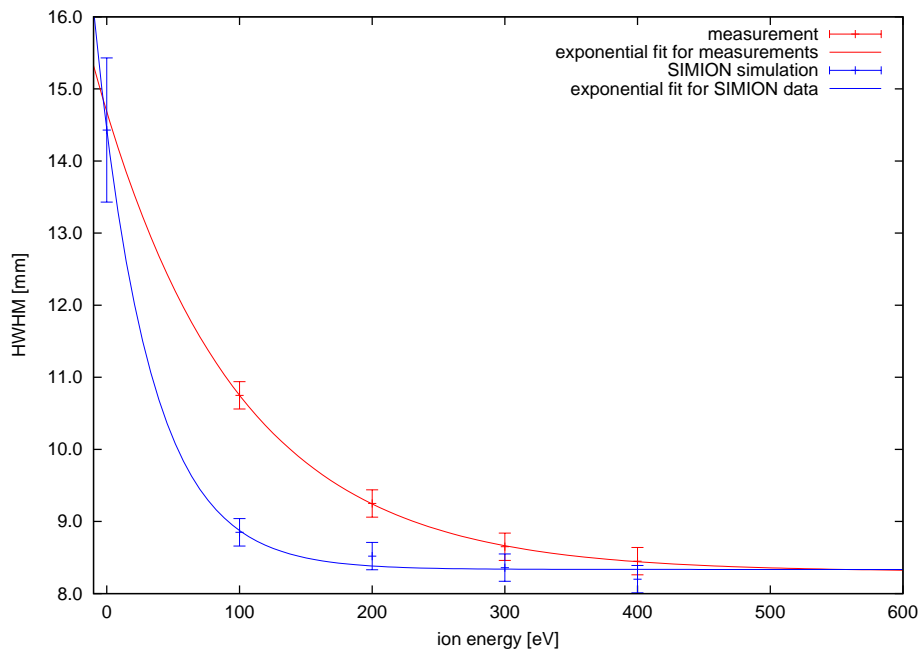


**Fig. 6.10:** Measured peak widths HWHM and exponential fits for both, measured (upper red curve) and simulated (blue) beam shapes (see also Fig. 5.16 on page 82).

SIMION gives some interesting insights in the LEIS, despite the fact that it

was not possible to reproduce results like the energy distribution. Unknown factors like collisions with walls and grids, surface impurities, and electrical noise of the used power supplies are not negligible and cannot easily be simulated.

## 7. CONCLUSIONS & OUTLOOK

The Low Energy Ion Source has been successfully built and tested. The obtained data during the characterization of the source show good performance.

- The microtip has been conditioned and successfully operated over a period of 1.5 years (see chapter 5.1).
- The gas inlet system has been successfully tested in the dynamic (gas introduction directly into the source) and the static mode (gas introduced through the bypass).
- The sensitivity in both modes, dynamic and static, has been determined (see chapter 5.3).
- The beam shapes of both modes are well known for different intensities. Besides, also the angle of the beam spread for an ion beam which was not further accelerated has been obtained and is typically  $65^\circ$  (see chapter 5.4).
- The energy of the ions, generated by the source, and their energy distribution has been measured and is typically in the order of a few eV. It is possible to further accelerate or decelerate the ions by floating the whole source (see chapter 5.5).

Based on the results of the presented work, future activities have to proceed parallel in two directions. In the near future it will be necessary to perform the ion mode calibrations with both ROSINA mass spectrometers RTOF and DFMS. For this purpose, also a DFMS test setup needs to be developed: one for the wide FOV and one for the narrow FOV ion source entrances.

Concerning the Low Energy Ion Source itself a few changes can be proposed:

- The microtip performance is below average in terms of emission current (see chapter 5.1.2). An exchange with another tip can be considered in the long run. It is also possible to implement another type of electron emitting surface without changing the whole setup. On the contrary, with some major changes in the source layout, a second microtip perpendicular to the first one would also help to further increase the emission current. However, for both ROSINA mass spectrometers, the obtainable ion current should be high enough for the ion calibration.
- For a slightly more homogeneous beam shape in dynamic mode, an obstacle could be introduced in front of the gas inlet behind the capillary plate (see chapter 5.4.2).
- To automatize the source, the new electronics package is designed to be controllable by a computer. Therefore some efforts are needed for software development i.e. LABVIEW. A regulated gas inlet would allow for an even higher degree of automatization.

Last but not least the Low Energy Ion Source can also be used in other experimental setups whenever an ion beam of a well known (low-) energy is needed.



## APPENDIX



## A. PICTURES

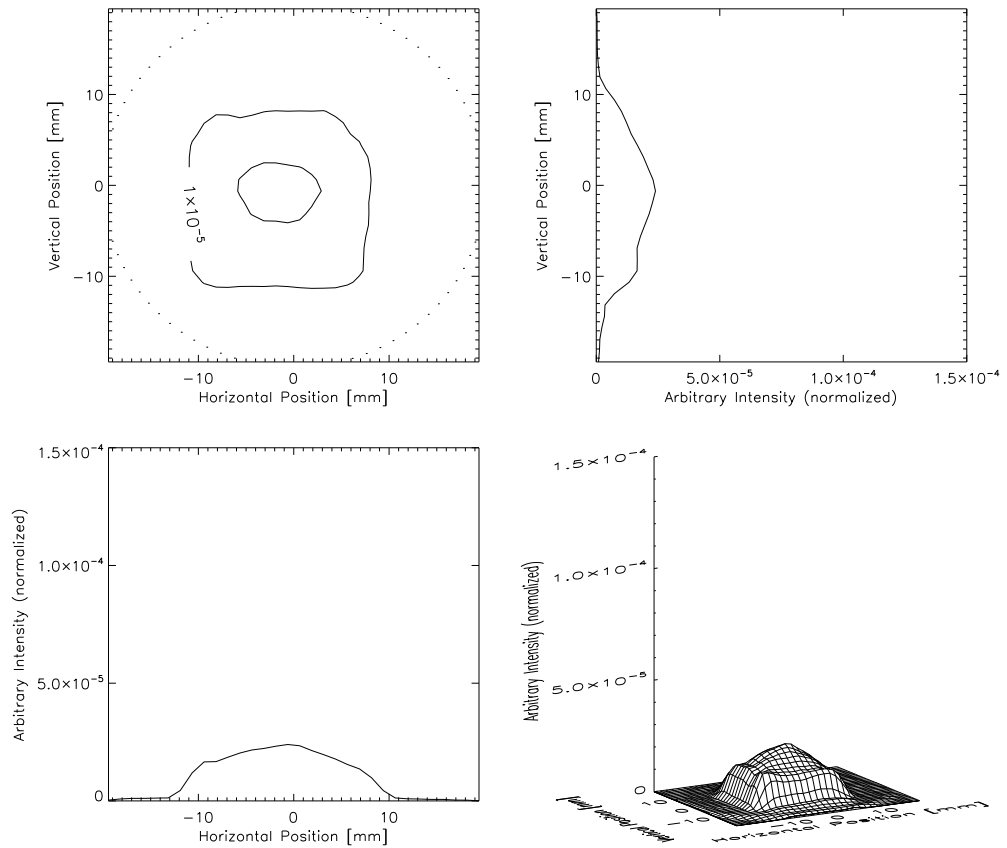


**Fig. A.1:** Beam shape at 2.0 nA electron emission current  $i_-$  in static mode at  $4.4 \times 10^{-8}$  mbar residual gas pressure. The plots are normalized to the intensity of the beam at 7.0 nA electron emission current in Fig. 5.8 on page 70. Top left the plot shows the  $1 \times 10^{-5}$  contour lines and top right a vertical cut through peak maximum is shown. Bottom left a horizontal cut through the peak maximum can be seen and bottom right the beam intensity is plotted as a 3D-surface.

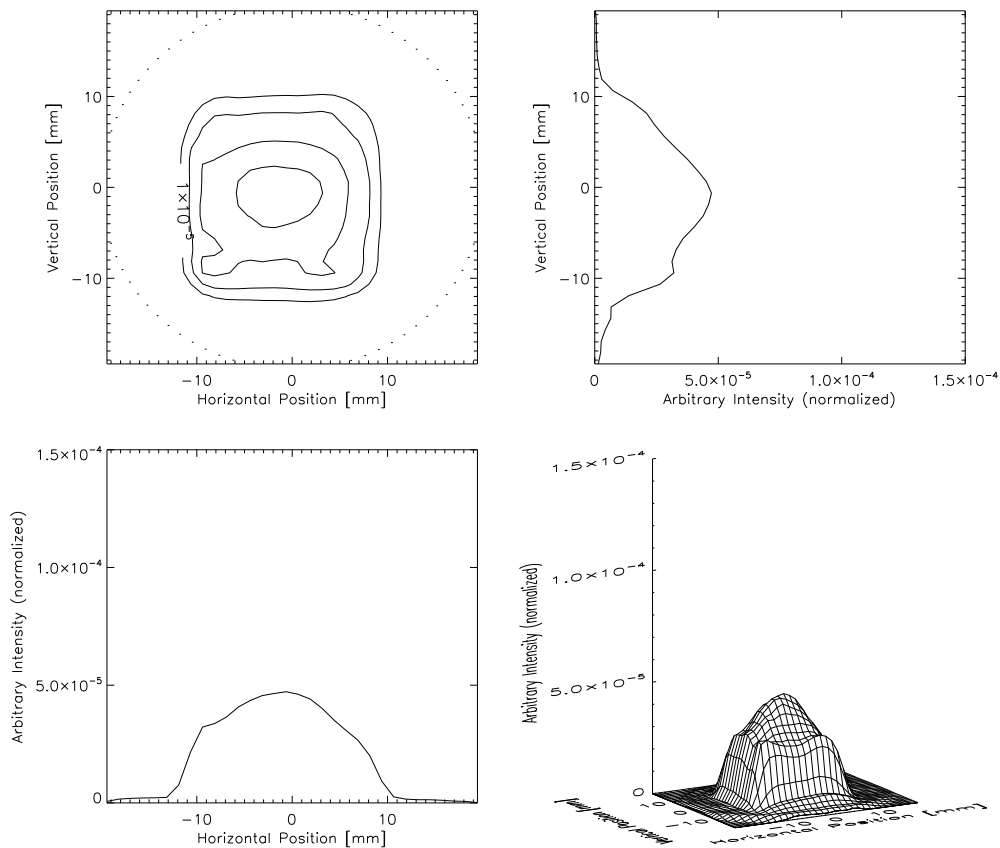


**Fig. A.2:** Beam shape at 4.0 nA electron emission current  $i_-$  in static mode at  $4.4 \times 10^{-8}$  mbar residual gas pressure. The plots are normalized to the intensity of the beam at 7.0 nA electron emission current in Fig. 5.8 on page 70. Top left the plot shows the  $1 \times 10^{-5}$  contour lines and top right a vertical cut through peak maximum is shown. Bottom left a horizontal cut through the peak maximum can be seen and bottom right the beam intensity is plotted as a 3D-surface.

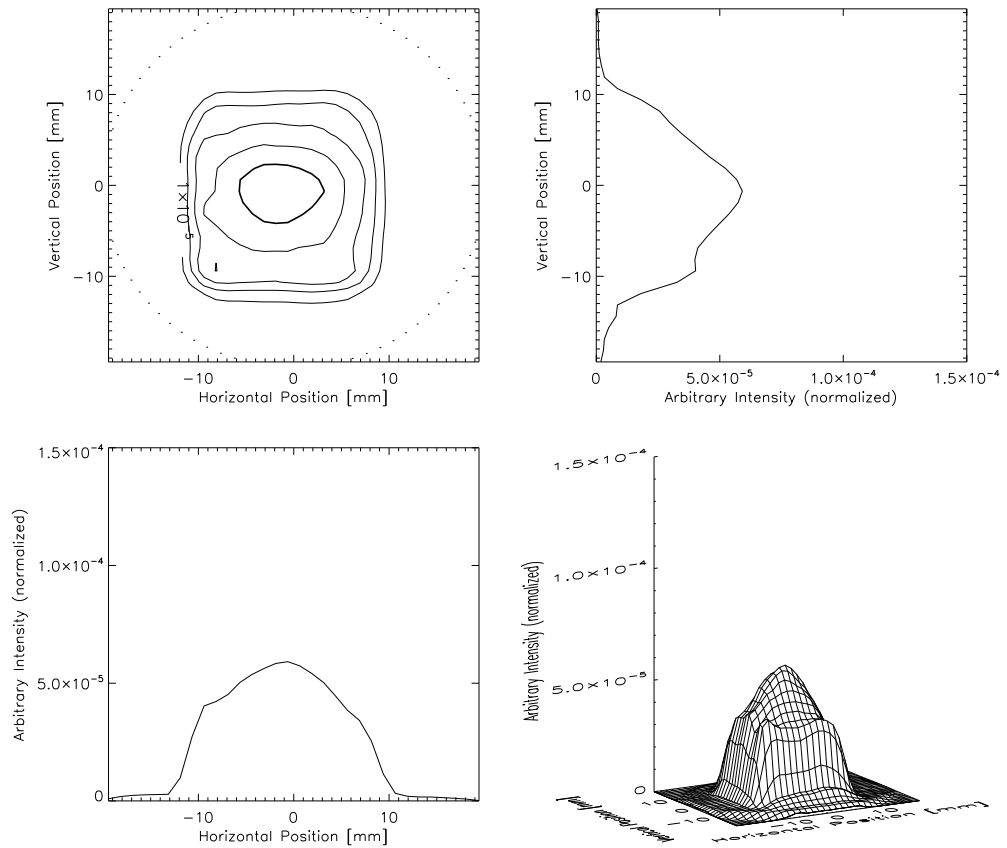


**Fig. A.3:** Beam shape at 5.0 nA electron emission current  $i_-$  in static mode at  $4.4 \times 10^{-8}$  mbar residual gas pressure. The plots are normalized to the intensity of the beam at 7.0 nA electron emission current in Fig. 5.8 on page 70. Top left the plot shows the  $1 \times 10^{-5}$  contour lines and top right a vertical cut through peak maximum is shown. Bottom left a horizontal cut through the peak maximum can be seen and bottom right the beam intensity is plotted as a 3D-surface.

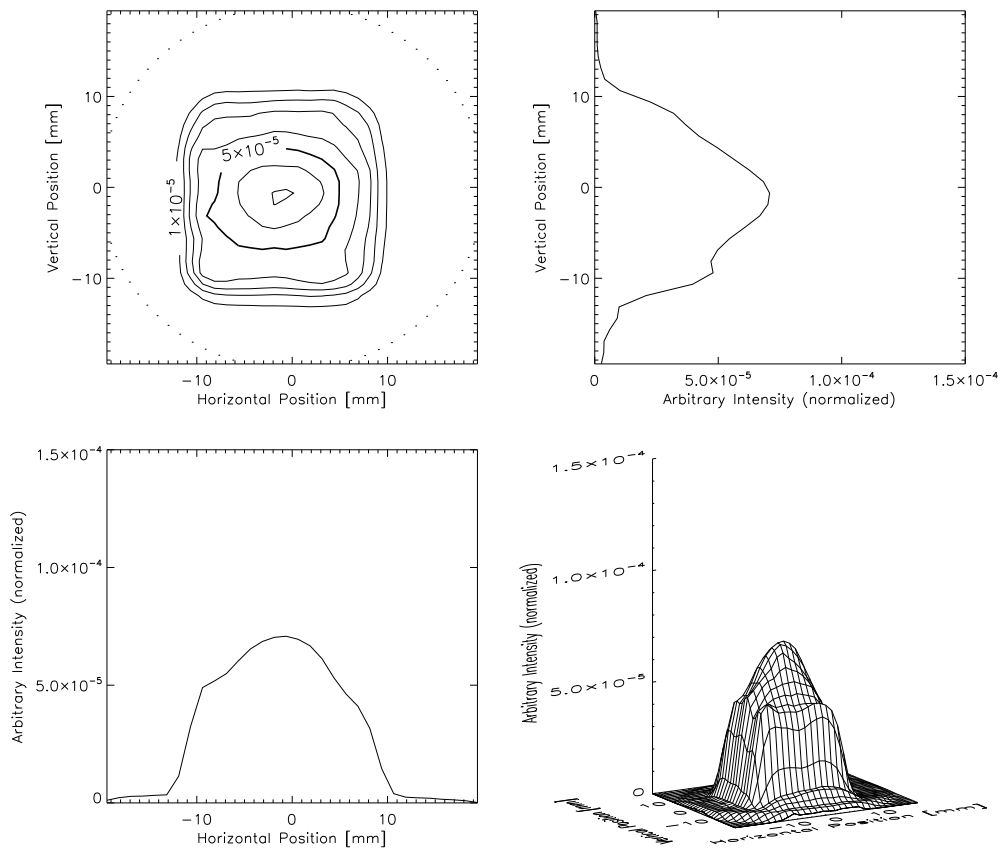


**Fig. A.4:** Beam shape at 6.0 nA electron emission current  $i_-$  in static mode at  $4.4 \times 10^{-8}$  mbar residual gas pressure. The plots are normalized to the intensity of the beam at 7.0 nA electron emission current in Fig. 5.8 on page 70. Top left the plot shows the  $1 \times 10^{-5}$  contour lines and top right a vertical cut through peak maximum is shown. Bottom left a horizontal cut through the peak maximum can be seen and bottom right the beam intensity is plotted as a 3D-surface.





B. DRAWINGS AND SCHEMATICS

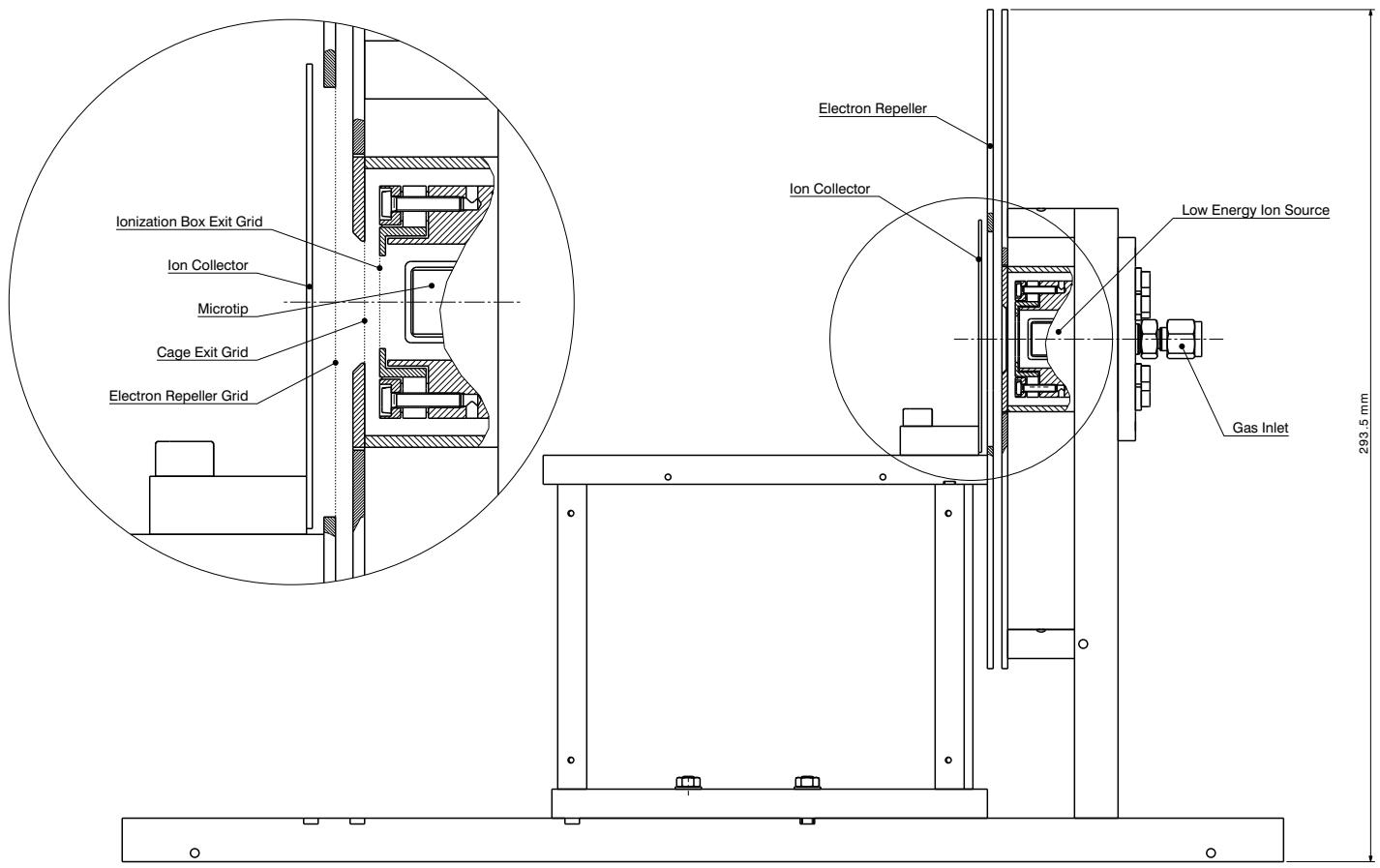
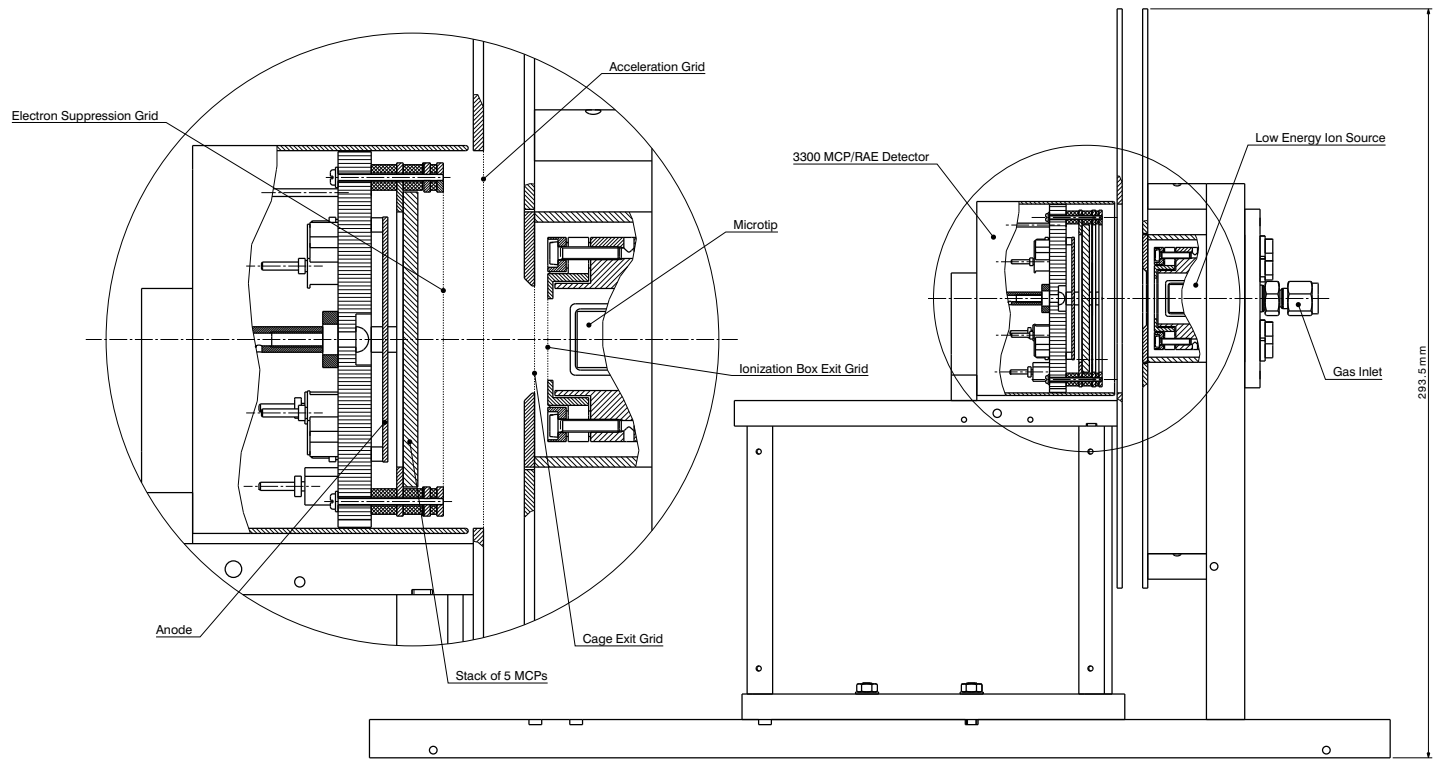
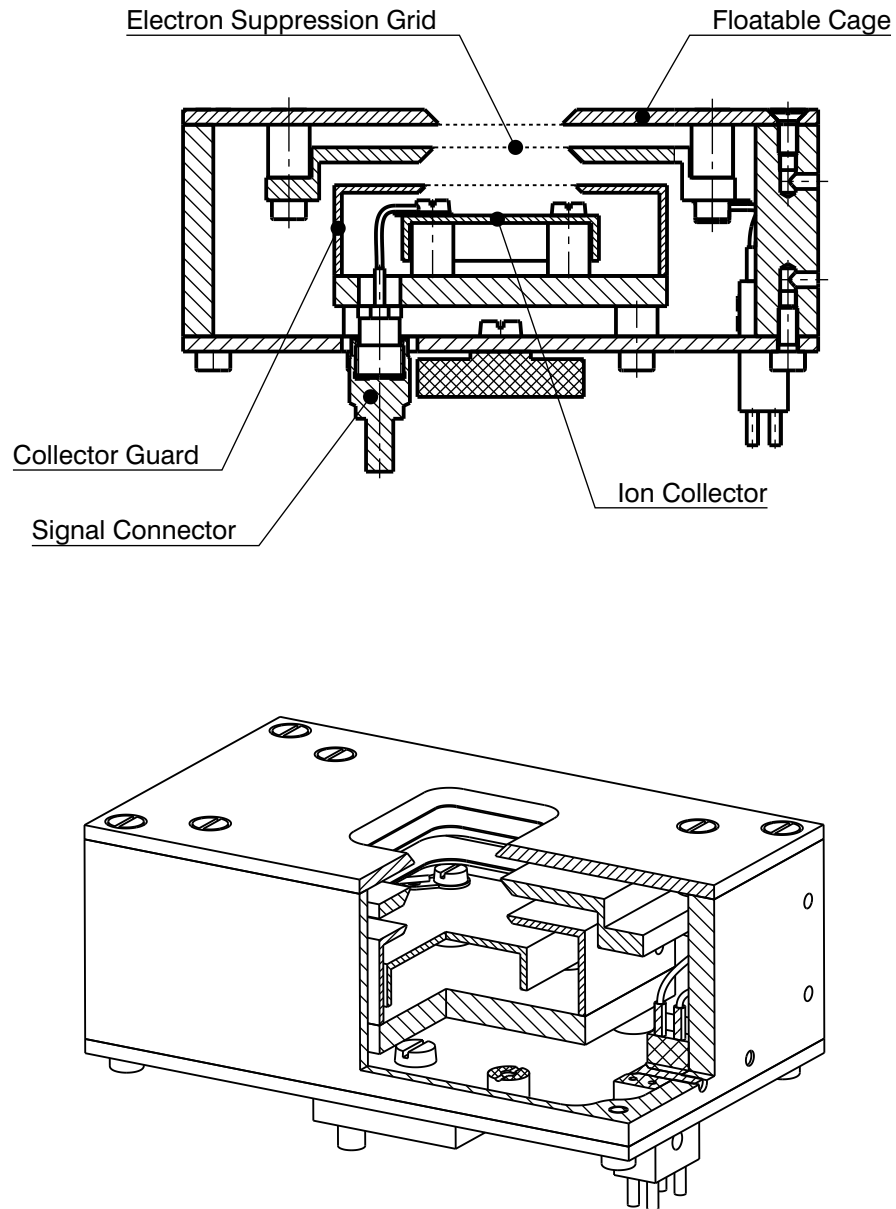


Fig. B.1: Current measurement setup.



**Fig. B.2:** Beam shape measurement setup.



**Fig. B.3:** The top figure shows a cut through the Faraday cup and the bottom figure the isometric view.

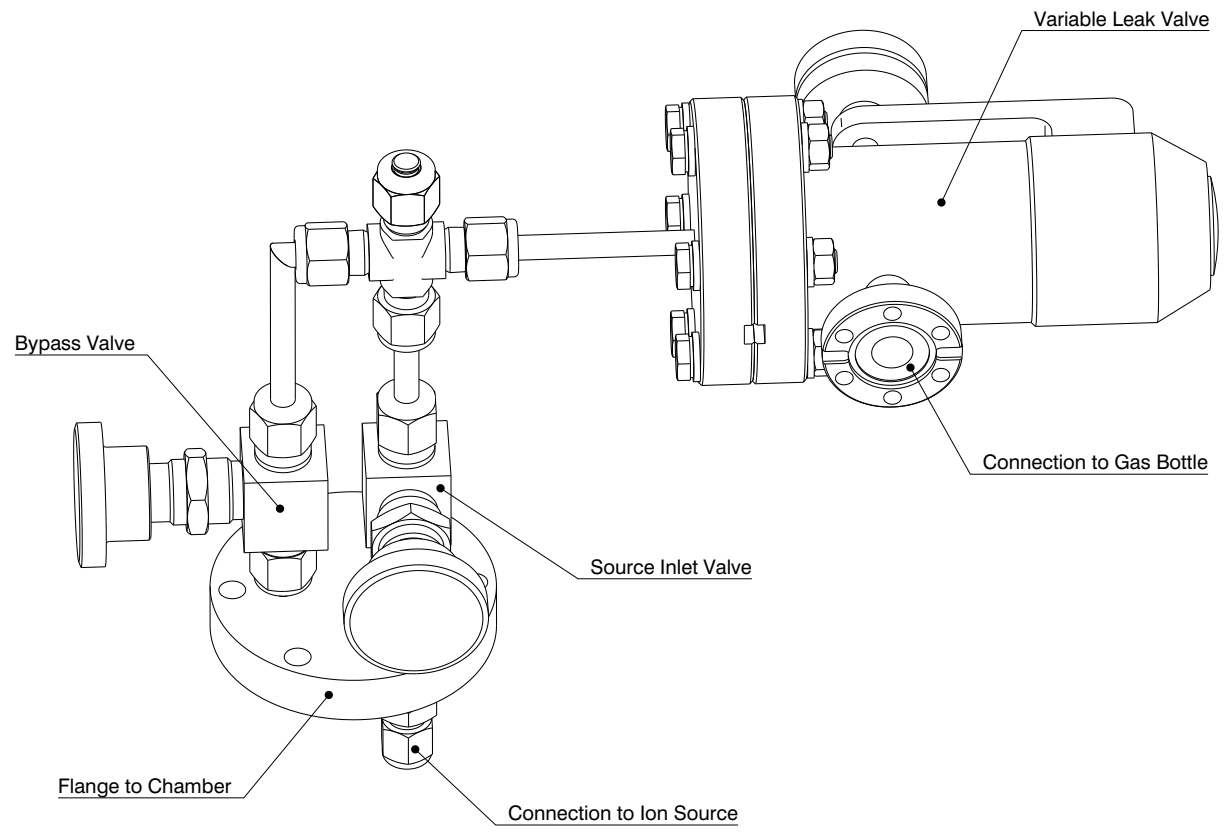


**Fig. B.4:** Gas inlet flange with variable leak valve.

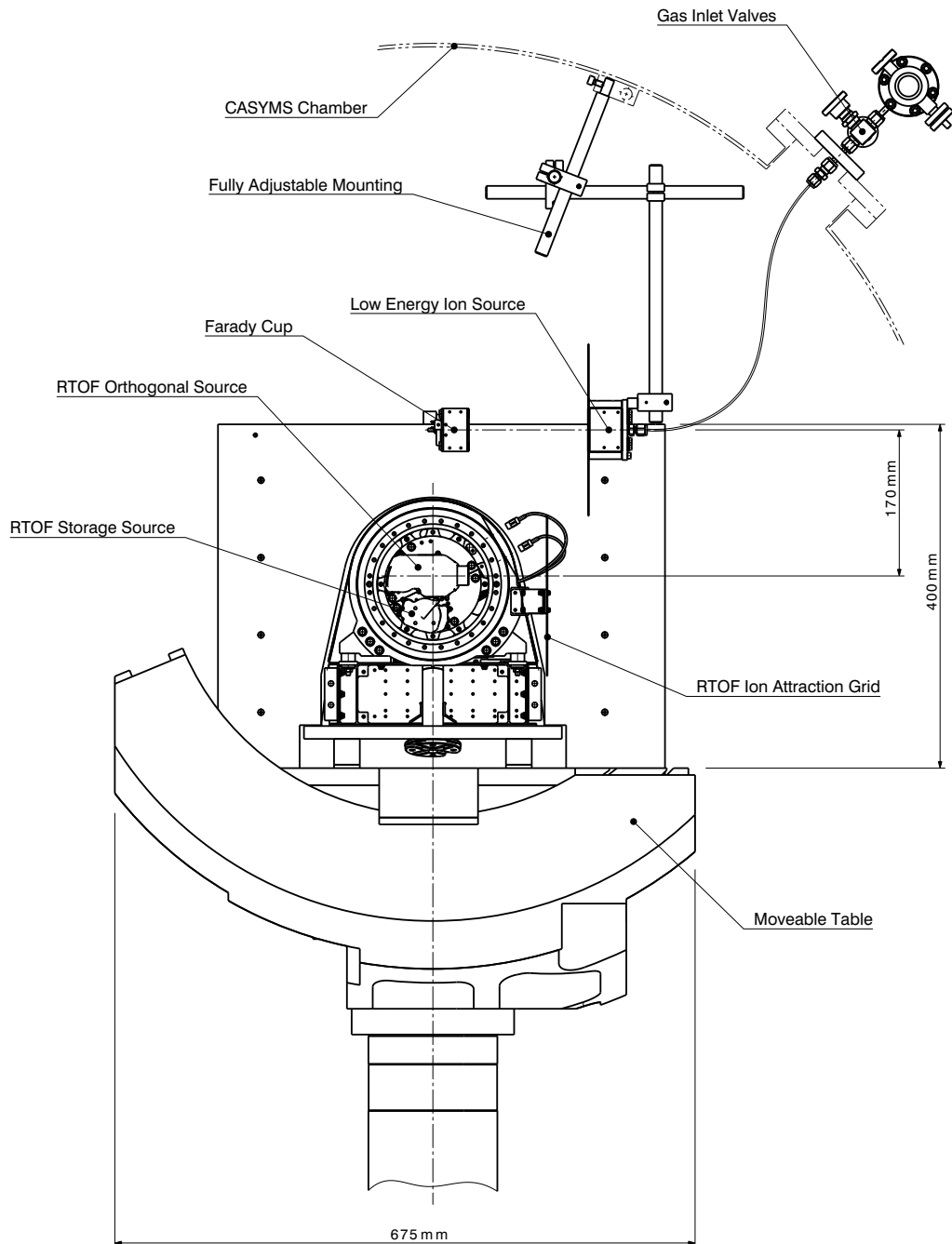


**Fig. B.5:** Front view of the Low Energy Ion Source (LEIS) mounted together with RTOF and the Faraday cup in the CASYMS chamber. The table can be moved so that either RTOF or the Faraday cup is in front of the LEIS.

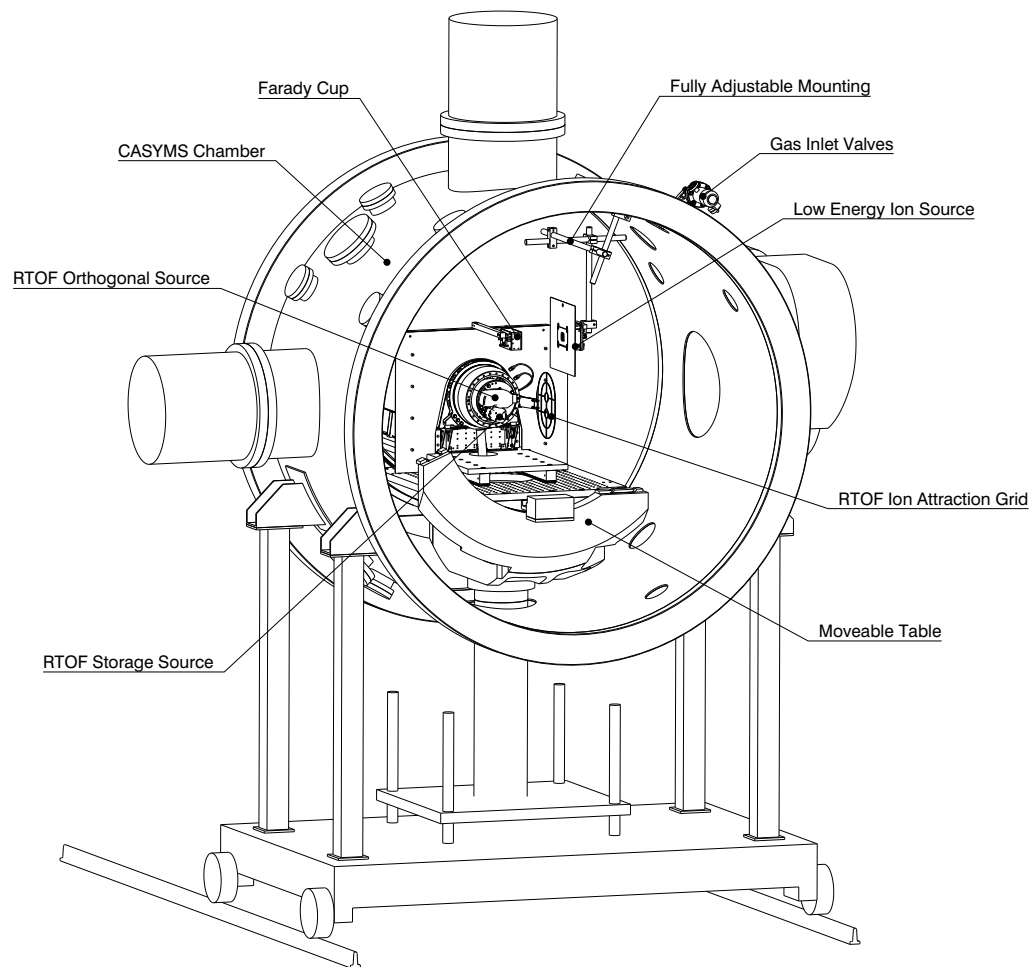


**Fig. B.6:** Isometric view of the Low Energy Ion Source mounted together with RTOF and the Faraday cup in the CASYMS chamber.

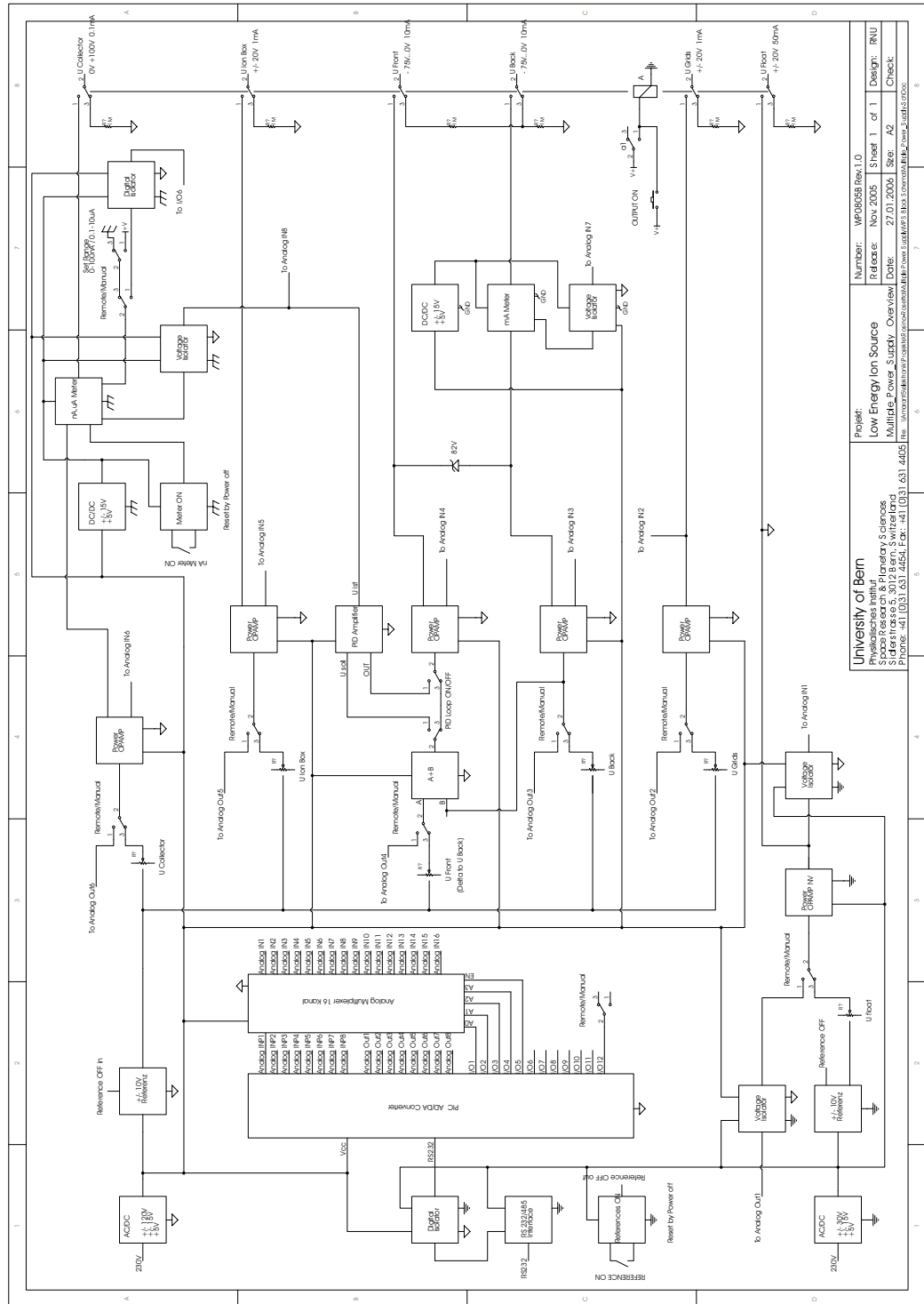
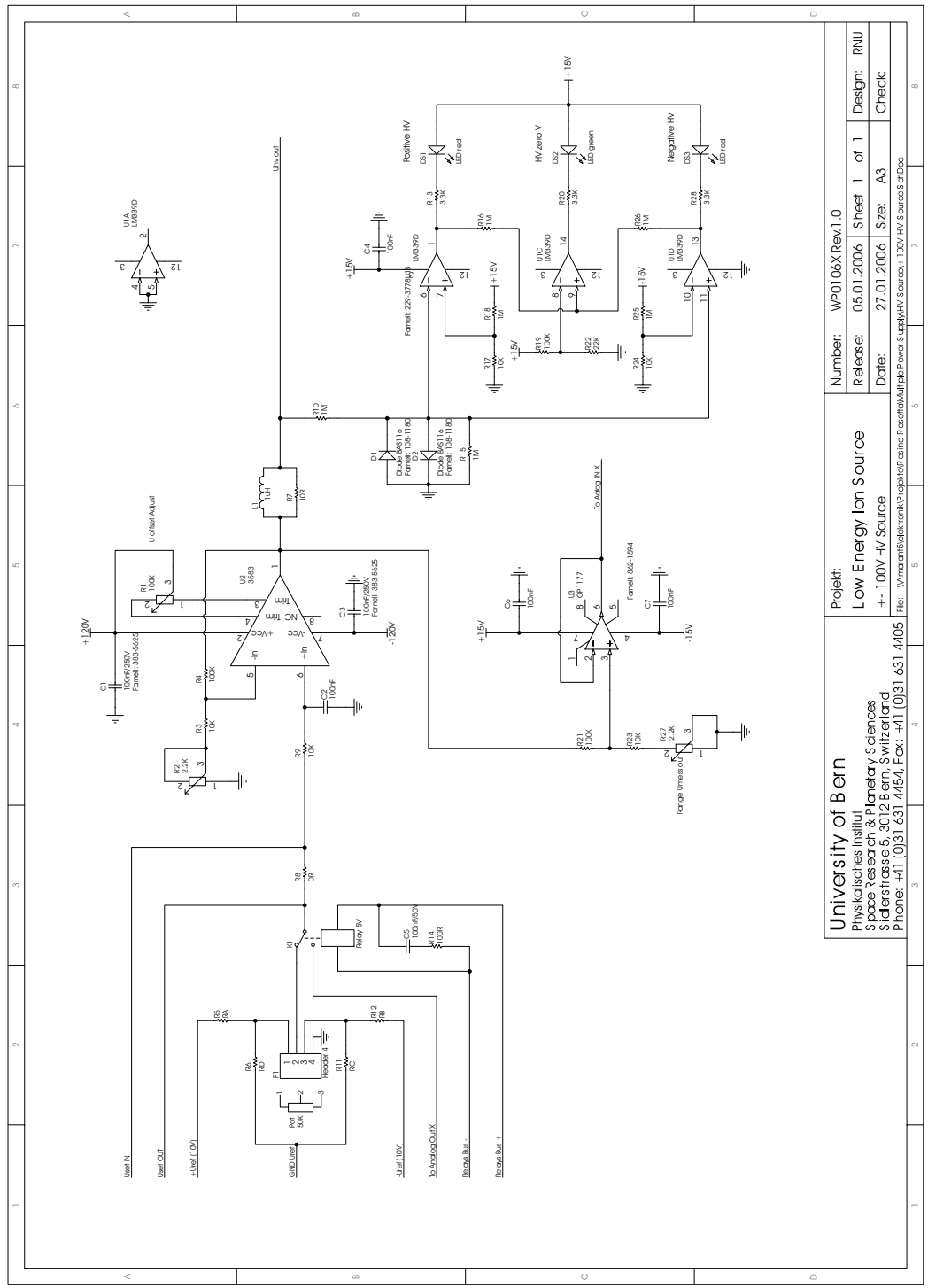


Fig. B.7: Low Energy Ion Source power supply circuit diagram. The power OPAMP modules scheme can be seen in Fig. B.8.





Project:	WP0106X Rev.1.0
Number:	05.01.2006
Release:	Sheet 1 of 1
Design:	RNU
Date:	27.01.2006
Size:	A3
Check:	
File: W:\mranon\5\Elektronik\IP_geraet\geraet\OPAMP\Multiplex Power S. ucp\HV_V_Sources\+-100V_HV_Sources.schDoc	

University of Bern  
 Physikalisches Institut  
 Space Research & Planetary Sciences  
 Sidlerstrasse 5, 3012 Bern, Switzerland  
 Phone: +41 (0)31 631 4454; Fax: +41 (0)31 631 4405

Fig. B.8: Circuit diagram of the power OPAMP modules.

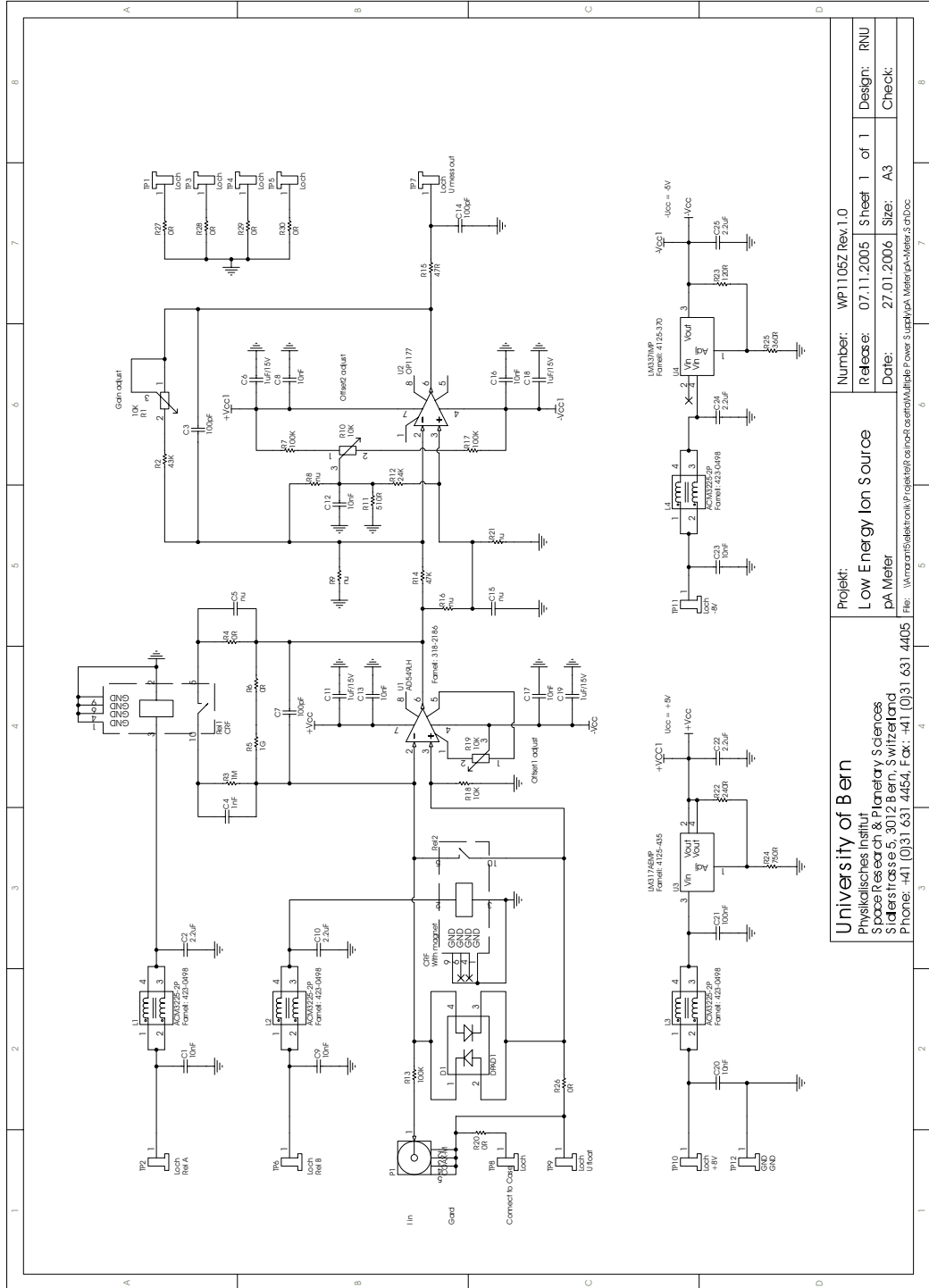


Fig. B.9: Faraday cup pA meter circuit diagram.

## BIBLIOGRAPHY

- [AJB<sup>+</sup>04] K. Altwegg, A. Jäckel, H. Balsiger, E. Arijs, J. J. Berthelier, S. Fuselier, F. Gliem, T. Gombosi, A. Korth, and H. Rème. Rosina's Scientific Perspective at Comet Churyumov-Gerasimenko. In *ASSL Vol. 311: The New Rosetta Targets. Observations, Simulations and Instrument Performances*, pages 257–+, October 2004.
- [BAB<sup>+</sup>86] H. Balsiger, K. Altwegg, F. Bühler, J. Geiss, A. G. Ghielmetti, B. E. Goldstein, R. Goldstein, W. T. Huntress, W.-H. Ip, A. J. Lazarus, A. Meier, M. Neugebauer, U. Rettenmund, H. Rosenbauer, R. Schwenn, R. D. Sharp, E. G. Shelly, E. Ungstrup, and D. T. Young. Ion composition and dynamics at comet Halley. *Nature*, 321:330–334, May 1986.
- [BAB<sup>+</sup>06] H. Balsiger, K. Altwegg, P. Bochsler, P. Eberhardt, J. Fischer, S. Graf, A. Jäckel, E. Kopp, U. Langer, M. Mildner, J. Müller, T. Riesen, M. Rubin, S. Scherer, P. Wurz, S. Wüthrich, E. Arijs, S. Delanoye, J. De Keyser, E. Neefs, D. Nevejans, H. Rème, C. Aoustin, C. Mazelle, J. L. Médale, J. A. Sauvaud, J. J. Berthelier, J. L. Bertaux, L. Duvet, J. M. Illiano, S. A. Fuselier, A. G. Ghielmetti, T. Magoncelli, E. G. Shelley, A. Korth, K. Heerlein, H. Lauche, S. Livi, A. Loose, U. Mall, B. Wilken, F. Gliem, B. Fiethe, T. I. Gombosi, B. Block, G. R. Carignan, L. A. Fisk, J. H. Waite, D. T. Young, and H. Wollnik. Rosetta Orbiter Spectrometer for Ion and Neutral Analysis ROSINA. *Space Science Reviews*, 2006. in press.

- 
- [BM06] T. Bagdonat and U. Motschmann. Plasma boundaries and ion dynamics at comet Churyumov-Gerasimenko. *Annales Geophysicae*, 2006. in press.
- [BMGK04] T. Bagdonat, U. Motschmann, K.-H. Glassmeier, and E. Kührt. Plasma environment of comet Churyumov-Gerasimenko 3D hybrid code simulations. In *The New Rosetta Targets*, pages 153 – 166. Kluwer, 2004.
- [BR04] J.-J. Berthelier and J.-F. Roussel. A study of the electrical charging of the Rosetta orbiter: 2. Experimental tests in a laboratory plasma. *Journal of Geophysical Research (Space Physics)*, 109:1105–+, January 2004.
- [Con98] C. Constancias. *Emission d'électrons par effet de champ à partir de micropointes pour écrans plats : simulations, caractérisations et confrontations expérimentales*. PhD thesis, Laboratoire LETI CEA, January 1998.
- [CTT75] P. M. Chung, L. Talbot, and K. J. Touryan. *Electric Probes in Stationary and Flowing Plasmas: Theory and Application*. Springer Verlag, 1975.
- [Dah00] D. A. Dahl. *SIMION 3D, Version 7.0, User's Manual*. Idaho National Engineering and Environmental Laboratory, P.O. Box 1625, Idaho Falls, February 2000.
- [DL66] S. Dushman and J. M. Lafferty. *Scientific Foundations of Vacuum Technique*. John Wiley & Sons, Inc., New York, London, Sydney, second edition, October 1966.
- [dL05] I. de Pater and J. J. Lissauer. *Planetary Sciences*. Cambridge University Press, 2005.
- [FN28] R. H. Fowler and L. Nordheim. Electron emission in intense electric fields. *Proceedings of the Royal Society of London. Series A, Containing Papers of a Mathematical and Physical Character*, 119(781):pp. 173–181, May 1928.

- [GYW73] P. D. Goldan, J. Yadlowski, and E. C. Whipple. Errors in Ion and Electron Temperature Measurements Due to Grid Plane Potential Nonuniformities in Retarding Potential Analyzers. *Journal of Geophysical Research*, 78(16):pp. 2907–2916, June 1973.
- [Ip87] W.-H. Ip. Cometary Plasma Tails and the Coma Source Region. In *Magnetotail Physics*, pages 367 – 382. The Johns Hopkins University Press, 1987.
- [Joc90] K. Jockers. Ion Dynamics in the Coma of Comets Giacobini-Zinner and Halley. In *Asteroids, Comets, Meteors III*, pages 353–+, 1990.
- [LAB<sup>+</sup>] U. Langer, K. Altwegg, H. Balsiger, J. J. Berthelier, B. Block, P. Eberhardt, B. Fiethe, J. Fischer, S. A. Fuselier, T. Gombosi, S. Graf, J. M. Illiano, E. Kopp, T. Magoncelli, A. Korth, E. Neefs, D. Nevejans, and M. Rubin. The Double Focusing Mass Spectrometer ROSINA-DFMS on-board the Comet Rendezvous Mission Rosetta. preprint submitted to Elsevier Science.
- [Mey66] R. Meyer. Procédés de Fabrication de Micropointes Métalliques. *Le vide*, 282:pp. 478–484, January 1966.
- [MKS97] U. Motschmann, H. Kafemann, and M. Scholer. Nongyrotropy in magnetoplasmas: Simulation of wave excitation and phase-space diffusion. *Annales Geophysicae*, 15:603–613, 1997.
- [Oat57] C.W. Oatley. The flow of gas through composite systems at very low pressures. *British Journal of Applied Physics*, 8:pp. 15–18, January 1957.
- [PB94] C. Py and R. Baptist. Stability of the emission of a microtip. *Journal of Vacuum Science & Technology*, 12:pp. 685–688, March 1994.
- [Ped95] A. Pedersen. Solar wind and magnetosphere plasma diagnostics by spacecraft electrostatic potential measurements. *Annales Geophysicae*, 13:118–129, February 1995.

- 
- [Qua91a] Quantar Technology, 3004 Mission Street, Santa Cruz, CA 95060. *3300 Series Open-Face MCP/RAE Sensors Installation and Maintenance Manual*, August 1991.
- [Qua91b] Quantar Technology, 3004 Mission Street, Santa Cruz, CA 95060. *3300/2400 Series System Installation and Operation Manual*, November 1991.
- [RB04] J.-F. Roussel and J.-J. Berthelier. A study of the electrical charging of the Rosetta orbiter: 1. Numerical model. *Journal of Geophysical Research (Space Physics)*, 109:1104–+, January 2004.
- [RBBW98] F. H. Read, N. J. Bowring, P. D. Bullivant, and R. R. A. Ward. Penetration of electrostatic fields and potentials through meshes, grids, or gauzes. *Review of Scientific Instruments*, 69(5):pp. 2000–2006, May 1998.
- [Roh01] U. Rohner. Messung der Gasdynamik bei Kometen, 2001. Master thesis.
- [SRL<sup>+</sup>95] H. C. Straub, P. Renault, B. G. Lindsay, K. A. Smith, and R. F. Stebbings. Absolute partial and total cross sections for electron-impact ionization of argon from threshold to 1000 eV. *Phys. Rev. A*, 52:1115–1124, August 1995.
- [WB73] R. G. Wilson and G. R. Brewer. *Ion Beams*. John Wiley & Sons, Inc., New York, London, Sydney, Toronto, first edition, January 1973.

## ACKNOWLEDGEMENT

I thank my advisor, Prof. Dr. Kathrin Altwegg, for giving me the unique opportunity to write my PhD thesis on the ROSINA instrument. I appreciated in particular the fruitful discussions we've had in the course of this work. My special thanks go to Prof. Dr. Tamas Gombosi from the University of Michigan for refereeing this work.

The extensive hardware production for this work required the assistance of many individuals from the engineering department, the mechanical workshop, as well as the electronics workshop:

- Josef Fischer and Martin Sigrist for sharing their profound knowledge with me as well as their continuous support.
- Daniele Piazza, Martin Rieder, and Beat Zahnd from the engineering office for their support.
- Jürg Jost, Jakob Stettler, and Roland Nussbaum for supporting me with electronics during the whole work.
- Harry Mischler, Sascha Häusler, and the whole mechanics workshop for their help.

I am furthermore indebted to:

- Dr. Annette Jäckel for the close collaboration concerning the first RTOF ion measurements.
- Sandra Wüthrich for her help with the SIMION ion source simulations and reading through my thesis.

- Prof. Dr. Peter Wurz for supporting me with his knowledge.
- Adrian Etter for operating the CASYMS calibration facility.
- Reto Karrer for his assistance with IDL.
- Dr. Stephan Graf, Andre Galli, and Timm Riesen for reading through my thesis.
- Katja Ammon, Dr. Tobias Badertscher, and Dr. Frédéric Buclin from my office for the cooperative atmosphere.

I owe thanks to all of the people in the department of physics for their assistance in technical and administrative concerns. The favorable work environment made my work a real pleasure.

Finally, I also like to thank my family for their long-standing and continuous support and last but not least our wag-a-lot Golden Retriever Gino.

This work was founded by the Swiss National Science Foundation, the Prodex Program of the European Space Agency, and the Kanton Bern.



## CURRICULUM VITAE

### Personal Data

Name Rubin  
First names Martin  
Date of birth July 8, 1977  
Address Kapellenstrasse 1,  
3700 Spiez, Switzerland

### Education

1984 - 1988 Primary school Hofachern in Spiez  
1988 - 1993 Secondary school Längenstein in Spiez  
1993 - 1997 Gymnasium in Interlaken  
1997 Matura at Gymnasium Interlaken,  
Type C (natural sciences)

### Academic record

1997 - 2002 Studies at the University of Bern in physics,  
mathematics, and astronomy  
1999 - 2001 Master's thesis in physics at the Physikalisches Institut,  
University of Bern, Division of Space Research  
and Planetary Sciences,  
entitled "Development of an optimization strategy  
for ROSINA DFMS",  
Supervisors: Prof. Dr. Kathrin Altwegg and Prof. Dr. Hans Balsiger  
2002 - 2006 PhD thesis in physics at the Physikalisches Institut,  
University of Bern, Division of Space Research  
and Planetary Sciences, entitled  
"Development of a Low Energy Ion Source  
for ROSINA Ion Mode Calibration"  
Supervisor: Prof. Dr. Kathrin Altwegg

**Professional Training**

1999 - 2006 Teaching assistant of physics laboratory class and exercises for students of physics and other branches